2013

Engineered Soil with Thermally Controlled Wettability

Yi Dong
Lehigh University

ENGINEERED SOIL WITH THERMALLY CONTROLLED WETTABILITY

by

Yi Dong

A Dissertation

Presented to the Graduate and Research Committee

of Lehigh University

in Candidacy for the Degree of

Doctor of Philosophy

in

Civil Engineering

Lehigh University

May, 2013

Yi Dong

ENGINEERED SOIL WITH THERMALLY CONTROLLED WETTABILITY

Approved and recommended for acceptance as a dissertation in partial fulfillment of the requirements for the degree of Doctor of Philosophy

_____

Defense Date

_____

Dr. Sibel Pamukcu
(Dissertation Advisor)

_____

Approved Date

Committee Members:

_____

Dr. Muhannad Suleiman
(Committee Chair)

_____

Dr. Arup SenGupta

_____

Dr. Gregory Ferguson

_____

Dr. Mesut Pervizpour

ACKNOWLEDGEMENT

I would like to first thank to my advisor Dr. Sibel Pamukcu for her guidance, support, and generosity. It was a great fortune to meet her and to work with her making my Ph.D. experience at Lehigh University.

I would like to express my appreciation to my committee members for their insightful and invaluable comments and suggestions: Dr. Arup SenGupta, Dr. Gregory Ferguson, Dr. Mesut Pervizpour, and Dr. Muhannad Suleiman. Special thanks go to Dr. Taesup Yun for drafting this research and formulating the plan.

I also want to thank my parent for always believing I could accomplish anything, and their unconditional love and continuous support for me.

I would like to thank all past and current members in our geotechnical group at Lehigh for their assistance, encouragement, and discussion: Ehsan Ghazanfari, Hai Lin, Lusu Ni, Suguang Xiao.

I wish to acknowledge the Lehigh University and National Science Foundation for providing the funding for this research.

TABLE OF CONTENTS

LIST OF FIGURES

LIST OF TABLES

ABSTRACT

Engineered soils are geo-materials with designed mechanical, physical, and chemical properties to address practical problems in geotechnical and geo-environmental applications. This research focused on the development of an innovative “smart soil”, and centered the fundamental understanding of capillary effects, mechanical properties, and conduction behaviors of this new material with the emphasis on reversible surface wettability.

Surface-initiated atom-transfer radical polymerization (ATRP) technique was explored to synthesize engineered soils coated with a thermally sensitive polymer. Several surface characterizations were used to verify the surface modifications. Particle-level observations revealed the influences of the particle-fluid interactions and pore space liquid distribution on particle connectivity and propagation-path establishment in porous media with different wettability. A numerical simulation was conducted to analyze the capillary pressure and capillary forces applied at particle contact with various volumes of liquid bridge. Complementary shear-wave-velocity tests captured the “cementing” effect induced by capillarity at low degrees of saturation of water for hydrophilic soils. Finally, thermal and electrical properties of engineered soils with different wettabilities were analyzed experimentally at varying degrees of saturation to gain an enhanced understanding of effects of particle-water interaction on thermal and electrical conduction

behaviors. Hydraulic transport responses under three conditions were studied to examine the influences of surface properties on flow performances – dry soil water infiltration, saturated flow, air imbibition and gravity drainage.

CHAPTER 1

INTRODUCTION

1.1 BACKGROUND

Soil functionality

One of the key issues for geo-engineers has been to improve soil properties to mitigate indiscriminate geo-hazards and to broaden their functionality as engineering materials. The common approaches include physical modifications of soil minerals, chemical treatments of soil solids and pore fluids, introduction of anomalous materials, and mixing of different granular materials to achieve desired functionalities. For instance, the mixture of geo-materials with different stiffness help reduce the settlement of foundations (Zornberg et al., 2004). Mixing granular materials of different thermal properties, such as silica sands and tire rubber particles, induce thermo-elastic damping within the mixture that can be exploited for vibration mitigation in the subsurface (Pamukcu and Akbulut, 2006). The colloidal particles and fine-grained clay minerals introduced into the pore space tend to mitigate the liquefaction potential of coarse grained deposits (Gallagher and Lin, 2005; Gratchev et al., 2007). "Intelligent" fluids responsive to magnetic excitation (e.g. magneto-rheological fluid) stiffen the soil for temporary solidification (Hryciw and Susila, 2005). The emerging interest in bio-geo engineering explores the feasibility of ground improvement using bio-mineralization and bio-gas

generation (Rebata-Landa, 2007). Yet, these approaches still render permanent and stationary modification of soil properties, which cannot be reversed in most cases, namely non-switchable and irreversible. In a dynamic environment where environmental conditions change, it is desirable to adjust the behavior of the engineered facility to adapt to the changes. Hence, extending the limited functionality of natural soils is an important advancement in geo-engineering targets.

Functionalized Surfaces

Advances in material science and surface chemistry permit modifications of surfaces by controlling chemical composition and conformational structure of a surface coating. For instance, surface modification with organosilanes, polymers and carbon nanotubes dramatically increases surface hydrophobicity (Dorrer and Rühe, 2008; Li et al., 2008; Rodriguez and Newaz, 1988; Rodriguez et al., 1997; Sanders et al., 2003). Particles and membranes coated with functional polymers and organosilanes can be used for separating immiscible fluids, removing oil from the surface, and sieving hazardous compounds (Bryant et al., 2003; Callewaert et al., 2005; Wang et al., 2008). However, these approaches are still limited by non-switchable properties. Although electro-wetting imposes quasi-tunable wettability on the surface, it requires additional electric energy or a secondary non-polar liquid to be completely reversible (Heikenfeld and Dhindsa, 2008). Hence, most approaches are limited by irreversible functionality where the achieved property cannot be reversed or "switched off" at demand in a dynamic environment.

Switchable and fully reversible surface wettability of host material can be achieved by grafting stimuli-responsive polymers, also referred to as "smart polymers". In this case the polymer type determines the desired functionality of the surface that

respond to a specific trigger, which can be applied externally (e.g., temperature) or occurring naturally (e.g., pH). For example, various external stimuli can trigger the reversible wettability of a functionalized surface, including temperature (Sun et al., 2004b; Wu et al., 2008; Zhang et al., 2007), pH (Kaeselev et al., 2001), ultraviolet light (Abbott et al., 1999; Ichimura et al., 2000; Rosario et al., 2004), solvent (Minko et al., 2003; Motornov et al., 2003), and electric potential (Lahann et al., 2003a; Lahann et al., 2003b). In these cases, the reactive polymers change their conformations or structures that change the attractive or repulsive interactions with the surrounding fluids and organic materials under different types of stimuli.

Synthesis and performance of stimuli-responsive "smart" polymers has been studied in a wide range of applications, including liquid chromatography (Ayano et al., 2006), controlled drug release (Zhang, 2007), adhesion and release of cultured cell from a substrate (Ista et al., 1999), and membrane filters to control fluid flow (Fu et al., 2007; Iwata et al., 1991), but never on a natural, geological material, such as silica sand.

1.2 MOTIVATION AND IMPORTANCE

The interest in engineered soil with switchable surface wettability controlled by temperature reflects geotechnical and geo-environmental concerns of subsurface processes.

Natural-hazard-induced water repellency: Increased water-repellency caused by wildfires that frequently take place on the West Coast brings indiscriminate vulnerability in geo-environment. Heating stimulates the volatilization and melting of

organic components and the subsequent condensation and redistribution onto mineral grains (DeBano et al., 1998; Franco et al., 2000). The reduced infiltration and evaporation of water impose considerable risk of hillside runoff, surface erosion, and unexpected overflow (Burch et al., 1989; Doerr et al., 2006; Scott, 2000). The altered surface wettability entails complexity in hydrologic systems.

Subsurface contamination: More than 60 % of large oil spill cases (>10k gallons) in the United States are related to storage tanks, regulated facilities of oil driiling, processing, and transmission facilities such as pipelines and vessels (Etkin, 2005a; Yoshioka and Vitale, 2005). More than 50 % of inland spill cases come from fixed facilities and pipelines (Stalcup et al., 2005). The U.S. EPA also estimates that more than 1 million releases of oil take place at underground and above-ground storage tanks to date, primarily caused by pipeline failures (Tafuri et al., 2005). These problems innately cause concern about contamination in geo-environments. The average cleanup cost was $73,000/ton in the United States in 1997 and it has been increasing for last three decades worldwide (Etkin, 2005b; Etkin, 2005c). Even small amounts of released oil results in severe contamination of groundwater, and jeopardizes the geo-environment and human life. Oil spills into the environment require prompt attention and post-cleanup operations to minimize contaminant migration. Chemical methods using dispersants, sorbents or solidifiers as a secondary cleanup may still introduce toxic materials into the environment. Bio-remediation can degrade residual hydrocarbons after the initial cleanup, but it may require long durations for acceptable results to emerge with concerns of nutrients and oxygen supplies during the process (after Exxon Valdez 1989; (Bragg et al., 1994)). Soil washing and incineration are not viable methods for deep subsurface

contamination. Thermal treatment is only effective for volatile components of oil (Catalan et al., 2004), and sediment removal is recommended for heavy contamination cases, though it has been shown unsuccessful in long-term case studies (Vandermeulen et al., 2005). Major challenges lie with current technical capabilities to mitigate spilled oils and oily wastes in subsurface.

Fluid separation: The efficient separation of immiscible fluids and production of oil maximizes energy recovery because water occupies large quantity of the waste streams (Anonymous, 1991; Khan and Islam, 2006). Hydrophilic or oleophilic surface of granular beds and membrane filters selectively remove fluids from permeating immiscible fluids after the first treatments using mechanically driven hydro-cyclone, gravity separation and flotation in down-hole (Delaine, 1985; Khan and Islam, 2006; Kong and Li, 1999; Rushton et al., 2000; Sokolovic et al., 2007).

Bioremediation and contaminant flow: Pathogens are major sources of groundwater contamination and waterborne diseases (Abbaszadegan et al., 2003). The appropriate control of transport and fate of pathogenic microorganism can mitigate subsurface contamination and enhance the efficiency of bioremediation processes. Bacterial transport through a porous network and bacterial adherence to the soil particle surfaces are governed not only by the microorganism attributes (cell size, surface macromolecules, hydrophobicity, and surface charge density of the membrane), but also the properties of the surfaces of granular materials (Baygents et al., 1998; Gargiulo et al., 2007; Ginn et al., 2002; Rosenberg et al., 1983). In particular, the degree of hydrophobicity and inter-molecular force of the soil particle surfaces determines the preferential adhesion and detachment of bacteria (Jacobs et al., 2007; Torkzaban et al.,

2006). A switchable or reversible surface wettability function of sand could provide additional control over engineered facilities for bioremediation processes.

The examples described above highlight that the surface wettability dominates the fate and transport of fluids and organic substances in soils. Moreover, the inherent wettability of natural soils can complicate remediation technologies and engineering control of fluid migration through them. A functionalized "smart soil" which possesses switchable and fully reversible surface wettability triggered by external stimuli could be deployed readily as an integral part of most civil infrastructures for environmental mitigation and fluid-separation purposes, as well as other functions such as electrical and thermal insulation on demand.

The work presented in this dissertation explores this new development. Silica sand was treated with a smart polymer using a state-of-the-art coating technique. The thermally sensitive polymer is hydrophilic at ambient temperature, but turns distinctly hydrophobic when the temperature rises above a threshold value. The main purpose for the functionalized sand was to integrate it with engineered facilities and civil infrastructure to accomplish or assist:

i) mitigation of subsurface contamination (i.e., detection, filtration, separation, retardation, or selective flow),

ii) separation of immiscible fluids (i.e., oil and water). As an example of subsurface application, the functionalized sand packs around buried gas/oil pipelines might be switched to a hydrophobic state by thermal stimulation to retard gas/oil leakage when and where encountered.

1.3 SCOPE AND ORGANIZATION

The goal of this research was to investigate the multi-scale behaviors of an engineered "smart soil" whose wettability is switchable and fully reversible, triggered by changes in temperature. In this process, innovative engineering implications relevant to the surface wettability were discovered and demonstrated. The thermal stimuli-responsive sand manufactured and tested in this research is predicted to serve as a prototype for other smart soils that can be manufactured for a desired functionality by choosing a specific stimuli-responsive polymer. The stimuli can range from UV or solvent exposure, to pH and ionic strength of the surrounding environments. A mixture of such engineered soils may possess broad functionality to be triggered either by externally applied stimuli or target natural occurrences.

Table 1.1 The scope of tasks and level of studies in this manuscript.

Mineral Surface *molecular-scale (nm)*	*Porous Network* *2D micro-scale (μm-mm)*	*Bulk Soil* *3D macro-scale (>mm)*
Task 1	**Task 2**	**Task 3**
1.1 Synthesis of Functionalized Soil : physical adsorption and chemical bonding 1.2 Surface Characterization : SEM, AFM, FT-IR, XPS	2.1 Interfacial Interaction : optical inspection 2.2 Characterization of Surface Wettability : contact angle, water penetration	3.1 Macro-Scale Behavior : physical characterization, conduction (hydraulic, thermal and electrical) behaviors

This research explored the behavior of interfacial interactions between the functionalized soil and the participating fluid at particle level using complementary experimental study and analytical techniques. The specific goals of the work included:

i) synthesis of thermo-responsive polymer grafted soils,

ii) surface characterizations,

iii) optical observation of particle-fluid interaction and fluid distribution, and

iv) characterization of selected bulk physical properties.

The scope of the work and the level of the particular tasks are summarized in Table 1.1.

Chapter 2 describes polymer-coating techniques, and explores efficient polymerization methods to graft functional polymers on the particle surface. Characterizations of the modified surface were conducted to verify the polymer synthesis and particle coating.

Chapter 3 reports the contact angles and water affinity for water penetration, as well as examines the particle-water interaction and pore-fluid distribution on particle surfaces with different wettability during wetting and drying circles.

Chapter 4 documents the fundamental study of the capillary effect in unsaturated particulate materials both at the particle and macro level. Numerical modeling complements the experimental study.

Chapter 5 centers on the conduction behavior including hydraulic, electrical, and thermal transfer in functionalized sands in their hydrophilic and hydrophobic states.

Chapter 6 summarizes general key conclusions and offers recommendations for future studies.

CHAPTER 2

SYNTHESIS OF FUNCTIONALIZED SOIL AND SURFACE CHARACTERIZATIONS

2.1 INTRODUCTION

Temperature-Sensitive Polymer

Through a preliminary literature review to seek a polymer that is adaptable to endow soils with a switchable wettability, we concluded that the thermo-responsive poly(*n*-isopropylacrylamide), or poly-NIPAAm or PNIPAAm, is the most appropriate material. It has been widely used in membrane separations (Guilherme et al., 2003; Liang et al., 1999; Okamura et al., 2005), drug delivery systems (Hsiue et al., 2002; Zhang et al., 2004), chromatography (Ayano et al., 2006), enzyme and cell immobilization (Okamura et al., 2005), and molecular valves (Peng and Cheng, 1998).

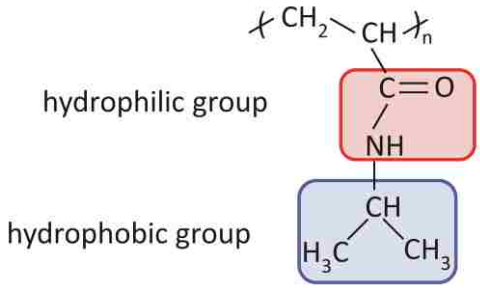

Figure 2.1 Molecular structure of PNIPAAm: -(CO)-NH- group (hydrophilic) and -CH(CH_3)$_2$ group (hydrophobic).

Figure 2.1 depicts the molecular structure of PNIPAAm. The repeating unit (monomer) of the polymer chains has one hydrophilic group and one hydrophobic group. PNIPAAm has a lower critical solution temperature (LCST) of ~32 °C, which is highly approachable in the subsurface environment. Below the LCST, this polymer forms swollen coils due to strong hydrogen bonds between the amide (-CONH-) group of PNIPAAm and water molecules, and shows hydrophilic behavior. On the other hand, the polymer chain becomes insoluble and collapses above the LCST and exposes the isopropyl ($-CH(CH_3)_2$) group to produce a hydrophobic state. Figure 2.2 (left) shows the

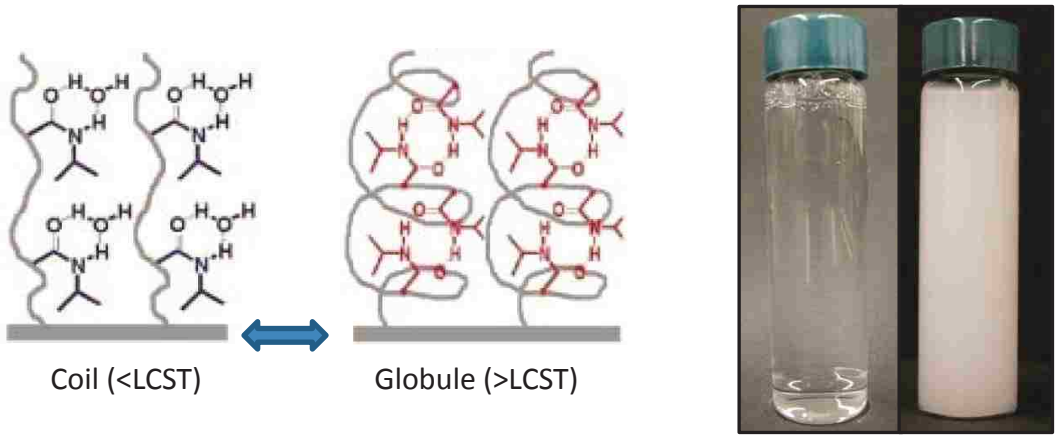

Figure 2.2 Diagram of reversible formation of intramolecular hydrogen bonding between C=O and N-H groups in PNIPAAm chains (left), which is considered to be the molecular mechanism of the thermally responsive wettability of a PNIPAAm thin film (Sun et al., 2004b). Photos of poly-NIPAAm solution of water (right): transparent in room temperature, and milky white when heated.

schematic change of conformation of the PNIPAAm film on a flat surface. The sharp phase transition provides switchable hydrophilic and hydrophobic properties to the grafted substrate. Note that this structural change only occurs when the polymer meets water as the temperature change, therefore the hydrophilic-hydrophobic switch only happens when the polymer coating is in (against) water. In other words, if no water presents, the surface coating does not change its molecular conformation, and then surface wettability, when temperature across the LCST. The photos in Figure 2.2 (right) capture the phase switch of the poly-NIPAAm solution of water when temperature across the LSCT. When the solution is in room temperature, it is transparent, colorless liquid, while the temperature increases above 32 °C, it quickly turns into milky white colloid fluid.

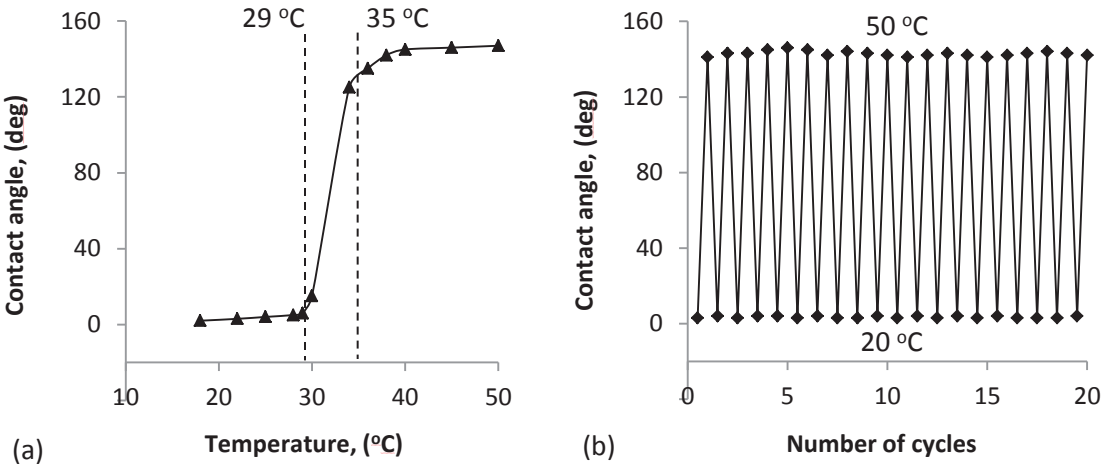

Figure 2.3 Re-plot of wettability of a PNIPAAm-modified surface (Sun et al., 2004b). (a) Temperature dependences of water contact angles for PNIPAAm coating on the a rough-enhanced silicon substrate. (b) Water contact angles at two different temperatures for a PNIPAAm-modified rough substrate.

Figure 2.3 shows the surface wettability responses to the temperature change. Left plot indicates the surface wettability had an abrupt change if the temperature across the LCST. When temperature increased from ~30 °C to ~35 °C, the contact angle increased almost instantly from near 0° to 120°. The cyclic heating-cooling test (right) justified the durability of this thermal sensitivity of surface wettabilities. After 20 cycles of temperature repeat between 20 °C and 50 °C, the hydrophilicity at 20 °C and hydrophobicity at 50 °C were very stable and not deteriorated.

2.2 REVIEW OF POLYMER-COATING TECHNIQUES

There are mainly two strategies for addition of polymer coatings, distinguished by the interaction between the polymer film and the substrate surface. In one of these, physisorption, the polymer layer is only held by physical forces (e.g. van der Waals force) between the polymer molecules and the substrate. In the other method, chemisorption, the polymer layer is chemically connected to the substrate surface by covalent bonds.

2.2.1 Physisorption

During the process of the physical adsorption of polymer coatings onto a substrate, the surface is treated with a solution of the polymer, and the polymer molecules are deposited as the solvent evaporates. There are several well-established methods of physisorption in practice including paint-coating, spray-coating, spin-coating, dip-coating, and doctor-blading (Advincula et al., 2004). The method is somewhat empirical yet simple, similar to the lacquer or enamels painted on the surface of an object for water-

proofing. The disadvantage of the process is that the polymer coating is often not firmly attached onto the substrate surface. The interfacial forces are weak and vulnerable to adverse environments, thus subject to deterioration by (Advincula et al., 2004):

- Desorption and displacement. Contaminants, strong solvents or competing adsorbates in the environment can interact and dissolve or displace the coating;
- Dewetting. If the interfacial free energy of the substrate and the substrate-liquid interface are low relative to that of the coating material, the coating liquid may not spread on the substrate;
- Delamination. If the films are in the glassy state and subjected to wide temperature swings, or if the coating swells while the substrate does not, strong mechanical stresses can develop at the interface and cause the entire film to peel off, leading to large-scale adhesive failure.

2.2.2 Chemisorption

Covalently grafted chains on surface, attached either by the "grafting to" or "grafting from" techniques can overcome the shortcomings of physisorption (Advincula et al., 2004; Dai, 2004).

In the "grafting to" method, preformed polymer chains containing a suitable end-functionalized group are allowed to react with a surface to obtain a "brush" structure. Although the brush layer exhibits thermal and solvolytic stability, it inherently possesses a low grafting density and film thickness on the surface. This is due to the inability of large polymer chains to diffuse to the reactive surface sites that are sterically hindered by surrounding bonded chains (Advincula et al., 2004).

In order to circumvent these disadvantages, a "grafting from" technique is utilized in which the polymer brush layer is generated *in situ* from a suitable surface-immobilized initiator. Due to the small molecular size of the immobilized initiators, which are predominantly formed using a coupling agent containing the desired initiating functionality, high grafting densities are easily obtained. Since the brush length is directly proportional to polymer-chain molecular weight, control over the polymerization would lead to a uniform brush thickness.

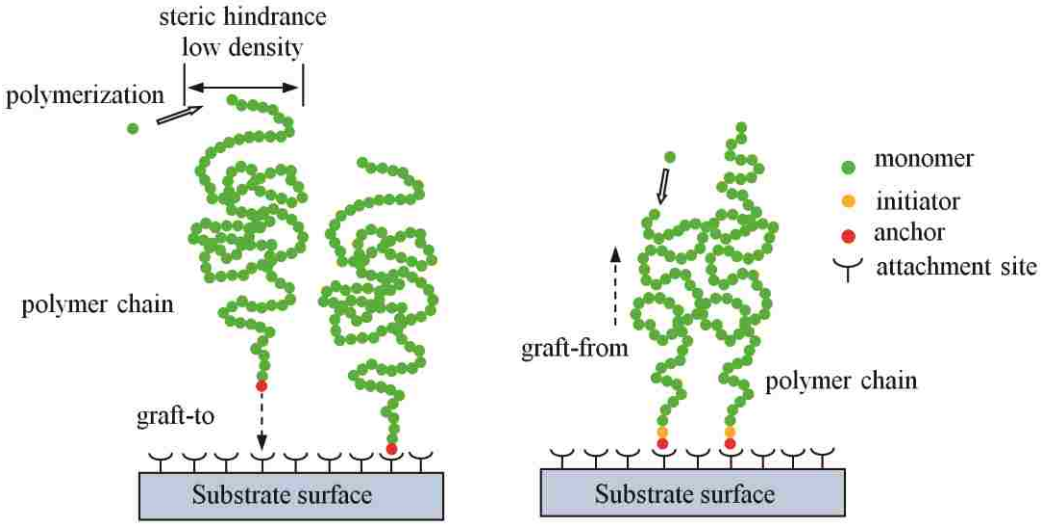

(a) Graft-to coating method (b) Graft-from coating method

Figure 2.4 Schematic illustration of comparison of two types of polymer coating approaches (Advincula et al., 2004): (a) the anchor sites are deposited on the surface while the polymerization was performed separately, and then the synthesized polymers were attached to the anchor sites. (b) The anchor site and initiator are attached on the surface first, then polymerization is triggered by initiator and addition of monomers one-by-one.

Figure 2.4 demonstrates the processes and distinguishes these two types of coating techniques. It shows the "graft-to" method in Figure 2.4-a, where polymers are formed before grafting onto the substrate, and "grafting-from" method in Figure 2.4-b, where the coating process is accomplished by initiating the polymerization from attachment sites.

The "grafting-from", namely surface initiated polymerization, which produces high density, homogeneous, and strong bonding coating film, was adopted in this study to synthesize thermally-sensitive polymer coatings on sand particles.

2.3 SURFACE-INITIATED ATOM-TRANSFER RADICAL POLYMERIZATION

The covalent attachment of ultrathin films of polymers to a solid substrate is often desirable to modify the properties of the surface. Either generated from surface or produced in solution, atom-transfer radical polymerization (ATRP) is one of the most effective and widely used methods of controlled radical polymerization (CRP) or living polymerization (Matyjaszewski, 2012b). It forms carbon-carbon bonds with the intervention of a transition metal catalyst. As the name implies, the atom radical is the key role in the process for uniform polymer chain growth. ATRP provides a simple yet effective route to many well-defined (co)polymers with predetermined molecular weight, narrow molecular-weight distribution (low polydispersity, usually the polydispersity index $PDI = M_w/M_n < 1.1$), high degree of chain-end functionality, and highly controlled molecular architecture in terms of chain topology and composition (Matyjaszewski, 2012a).

The basic principal is shown schematically in Figure 2.5. In ATRP, the equilibrium between propagating radicals ($P_n^{\bullet}$) and dormant alkyl halides species (P_n-X), activated by the transition metal complexes (Mt^m/L in a lower oxidation state m, Mt represents the transition metal species and L is a ligand), with the rate of constant activation k_{act}, is the mechanism of the reaction. The dominant species periodically react with the transition metal complexes to form growing radicals and deactivators (X-Mt^{m+1}/L, in a higher oxidation state with halide ligands) (Matyjaszewski, 2012a).

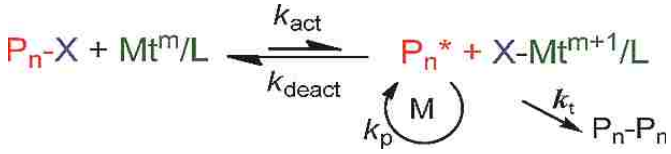

Figure 2.5 ATRP reaction mechanism involving radical-propagation equilibrium (Matyjaszewski, 2012a).

The general procedures of forming a thin film of polymer onto a solid silica surface can be differentiated into four steps (Braun et al., 2004; Dai, 2004; Jordan et al., 2006):

- surface cleaning and hydroxylation,
- amino-ended silanization,
- initiator anchoring,
- and growth of polymer chains, as shown in the following Figure 2.6.

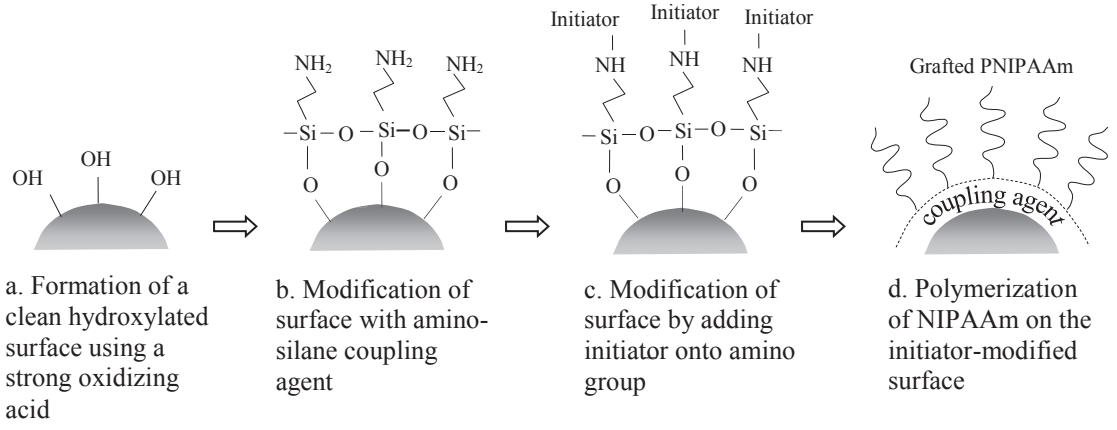

Figure 2.6 Schematic procedures to graft NIPAAm polymers on the silica sand using the surface-initiated atom transfer radical polymerization (SI-ATRP).

2.3.1 Surface cleaning and hydroxylation

A clean surface is important and necessary for the later treatments in surface-initiated-ATRP. The purpose of surface cleaning is to make a fresh SiO_2 surface by removing all impurities residing on it for the functional groups to stably attach. Both physical and chemical treatments can be found for successful surface cleaning.

Chemical cleaning involves strongly reactive solutions. This step combines hydroxylation since the use of a strong-acid oxidizer can at the same time be adding -OH groups on the inorganic surface, which makes the surface hydrophilic. Generally, piranha solution, H_2SO_4 (98 %) and H_2O_2 (30 %) (3:1 v/v), is used to remove most organic contaminants from the surfaces. (Allen et al., 2005; Aswal et al., 2006; Chen et al., 2006; Howarter and Youngblood, 2006; Wang and Vaughn, 2008; Xiu et al., 2006). An alternative cleaning solution is the basic piranha solution: a 3:1 mixture by volume of

ammonium hydroxide (NH_4OH) with hydrogen peroxide (H_2O_2). This solution needs to be heated to 60 °C to be effective (Arya et al., 2007; Aswal et al., 2006). If a pure silicon wafer is cleaned by piranha solution, the surface will be covered by an ultrathin layer of silicon dioxide (SiO_2) with a thickness of ~2 nm, which can be detected by ellipsometry (Allen et al., 2005; Aswal et al., 2006).

Two physical cleaning methods are available as well. One is utilizing sonication in an organic solvent such as chloroform, toluene or acetone, or a strong acid solution (HCl); and the other is using ultraviolet radiation of the surface in presence of oxygen (Aswal et al., 2006; Howarter and Youngblood, 2006; Xiu et al., 2006).

2.3.2 Deposition of amino-terminated silane coupling agents

Silanization of solid surfaces is widely used in surface modification to prepare substrate coated by a uniform functionality coating (Allen et al., 2005; Heiney et al., 2000; Howarter and Youngblood, 2007; Wang and Vaughn, 2008). The conformation of siloxane layer on the silica surface is shown in Figure 2.6-b. The covalently attached siloxanes provide a platform for further chemical reactions through an amine, halogen, or other functionalities at the end of the silane. Some important applications of aminosilane-modified surfaces are: (1) liquid-phase and affinity chromatography, (2) promotion of adhesion between polymers and ceramic or glass surfaces, (3) and production of immobilized artificial membranes or bio-molecules.

The (3-aminopropyl) trimethoxysilane (APTMS) and (3-aminopropyl) triethoxysilane (APTES) are the two most commonly used amino-silanes to form films for further deposition of polymers, due to the stability of Si-O bond, even at high

temperature, formed with the bond energy of 452 kJ/mol by APTMS and SiO_2 (Liu and Zhang, 2005). The molecular structures of these two silanes are shown in Figure 2.7. The

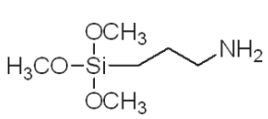

(a) APTMS

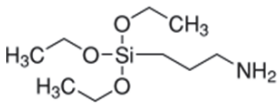

(b) APTES

Figure 2.7 Molecular structures of APTMS and APTES.

CH_3O- (MeO-) or C_2H_5O- (EtO-) groups react with surface hydroxyls on the native SiO_2 layer to form siloxane linkages, and active amino (-NH_2) groups are exposed and available as an anchor for further deposition of initiator.

The two main methods of this treatment are deposition from solution and vapor annealing. The former can be operated by an organic-phase solution or an aqueous solution of amino-silanes, and for annealing treatment, a concentrated (pure) vapor-phase or dilute vapor-phase can be used (Wang and Vaughn, 2008).

Howarter and Youngblood (Howarter and Youngblood, 2006; Howarter and Youngblood, 2007) ran a series of tests to evaluate the effects of different silane concentrations, varied reaction temperatures and durations to the final formed films. After surface cleaning and hydroxylating processes, the substrate slides were put into several previously prepared APTES-toluene solutions (1 %, 10 %, or 33 %), then held at temperature of 25 °C or 75 °C, lasting for 1, 24, 72 hours respectively.

Heiney and co-workers (Heiney et al., 2000) pointed out that the structure of an APTES film is complex in that there are many possible conformations and orientations of the molecule, and the surface coverage and structure depend sensitively on experimental

factors such as the reaction time, temperature, choice of solvent, water content of the solvent, and silane concentration. They adopted a different method to prepare the aminosilane SAM, where after the surface cleaning, the formation of aminosilane films included an adsorption process and an annealing treatment, in which the APTES layer was washed twice with methanol and baked at 120 °C for 4min. At this step, the molecules in the first layer undergo a conformational change, which is a flip from the amino bonding to a surface hydroxyl to one with the silanol end, forming a stable oxygen-bridged surface bond.

2.3.3 Synthesis of polymer brushes

After silanization, the surface becomes active to accept initiators for triggering the polymerization. In this research, bromoisobutyryl bromide (BiB) was used as the initiator. Figure 2.8 shows the structure of the BiB. In initiator immobilization, BiB was covalently attached to the surface-bound siloxane. The alkyl bromide in BiB is the key element to incite the reaction, under favored environmental conditions, to grasp the free monomers from solution and grow the polymer chain from the substrates. The schematic illustration of the processes is depicted in Figure 2.6-c, d.

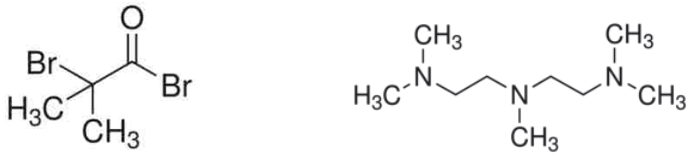

(b) PMDETA (a) BiB

Figure 2.8 Molecular structures of bromoisobutyryl bromide (BiB), and pentamethyl diethylene triamine (PMDETA).

Copper-based atom-transfer radical polymerization, which allows controlled polymerization of styrenes, acrylates, methacrylates, acrylamides, and acrylonitrile appears to be the most studied method (Huang et al., 2004). The CuCl/Me_6TREN (Me_6TREN = tris[2-(dimethylamino)-ethyl]amine) and CuBr/PMDETA (PMDETA = pentamethyl diethylene triamine) are the main catalyst and ligand complex used to control the polymer chain growth, conversion rate, and target molecular weight, low polydispersity (Nanda and Matyjaszewski, 2003). Huang and co-workers, and Nanda and Matyjaszewski studied the effect of the [PMDETA]/[Cu(I)] ratio, monomer and solvent polarity, counter ion, ligand on the ATRP process, which revealed that the ratio of 1/1 in more polar solvents ascribed to a neutral [Cu(PMDETA)Br] structure of the complex gave the highest values of k_{act} for Cu(I)Br (Nanda and Matyjaszewski, 2003). Some of the possible chemical structures of this transition metal based ligand complex system (Pintauer and Matyjaszewski, 2005) are shown in Figure 2.9.

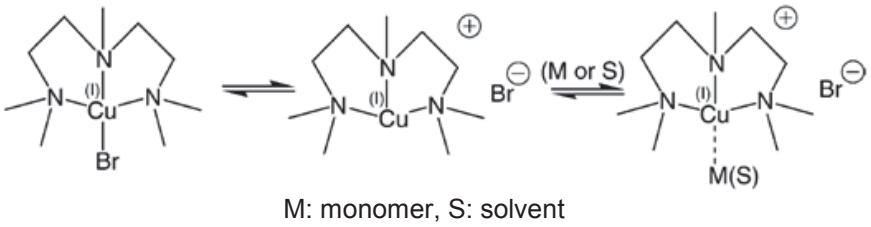

Figure 2.9 Proposed chemical structures of $Cu^{I}Br$/PMDETA complex (Pintauer and Matyjaszewski, 2005).

Sun (Sun et al., 2004a) adapted a SI-ATRP method to fabricate thermally responsive PNIPAAm thin films on both flat and rough silicon substrates with microgrooves etched by a laser cutter. For the polymerization, bromoisobutyryl bromide (BiB) was used as the initiator; and copper(I) bromide ($Cu^{I}Br$) and pentamethyl diethylene triamine (PMDETA) were used as the catalyst and the ligand, respectively. Under these conditions, the thickness of the grafted polymer layer obtained was around 44.8 nm. A switchable superhydrophobicity was observed with contact angle of water of 150°.

Xia (Xia et al., 2006a) reported an innovative dual-stimuli-responsive surface that could switch between superhydrophilicity and superhydrophobicity over a narrow temperature range and a wide pH range by fabricating a poly(NIPAAm-*co*-AAc) copolymer film on a silicon substrate. The whole polymerization process was almost the same as that described by Sun (Sun et al., 2004a), except one more monomer acrylic acid was added in the process. The final film thickness obtained was around 19 nm. Xia (Xia et al., 2007) used the same procedure to synthesize another multi-responsive surface grafted with NIPAAm-*co*-PBA copolymer film using acrylamidedophenyl boronic acid instead of AAc, which was sensitive to pH, temperature, and glucose concentration as well.

Xia (Xia et al., 2006b) investigated the relationship between the phase-transition temperature (cloud point) and the molecular weight. The thermal responsive PNIPAAm with high monomer conversion, well-controlled molecular weight and different hydrophobic and hydrophilic end group was synthesized by ATRP technique by choosing

$CuCl/Me_6TREN$ as the catalyst and ligand, alcohol as the polymer solvent and the appropriate initiators.

Other researchers used gold coated silicon surface as substrates, and indirectly tethered the PNIPAAm onto the Au surface. Ahn (Ahn et al., 2004) and Kaholek (Kaholek et al., 2004) obtained a gold-coated silicon surface with NIPAAm polymer brush fabricated by using the SI-ATRP "grafting from" approach with adsorbed monomer of bromide initiator. The polymerization was conducted under room temperature using Cu(I)Br/PMDETA with 1:5 molar ratio as the catalyst complex dissolved in MeOH. The ellipsometry analysis of the surface revealed a polymer brush layer tethered on the surface with a thickness of 250 nm.

2.4 EXPERIMENTATION

In this section, both coarse and fine silica sands were coated with thermally sensitive polymer by the process detailed in following section. Additionally, flat substrates (plain microscope glass slides and silicon wafers) were simultaneously coated using the same procedure. The flat substrates were utilized as reference surfaces to quantify the wettability of grafted PNIPAAm by measuring the contact angle of water, and as a substitution for scanning electron microscope (SEM), atomic force microscope (AFM), Fourier transfer infrared analysis (FT-IR) and X-ray photoelectron spectroscopy (XPS) measurements.

2.4.1 Materials

The main materials were (i) flat substrates: Fisher brand pre-cleaned plain microscope slides; 150 mm mechanical grade single-side-polished Si wafers from University Wafer; (ii) silica sands: Ottawa ASTM 20/30 sand (D_{50} = 0.72 mm, 99.8 % SiO_2), Ottawa F-110 sand (D_{50} = 0.11 mm, 99.8 % SiO_2); (iii) all the other chemicals were purchased from Sigma Aldrich and used as received without any further treatment. They were sulfuric acid (98 %), hydrogen peroxide (30 %), toluene (99 %), acetone (99 %), pyridine (99 %), methanol (MeOH 99 %), 3-(aminopropyl) triethoxylsilane (APTES, 98 %), dichloromethane (DCM, 99.9 %), bromoisobutyryl bromide (BiB, 98 %), copper(I) bromide (99.999 %), pentamethyl diethylene triamine (PMDETA, 99 %), *n*-isopropylacrylamide (NIPAAm, 99 %).

2.4.2 The Synthesis

There are four steps to the generation of PNIPAAm brushes on solid silica surfaces (Bi et al., 2008; Couet and Biesalski, 2006; Sun et al., 2004b; Xia et al., 2006a; Xia et al., 2007): 1) surface cleaning and hydroxylation, 2) amino-ended silanization, 3) initiator anchoring, and 4) chain growth of polymer or polymerization, as shown in the schematic in Figure 2.10.

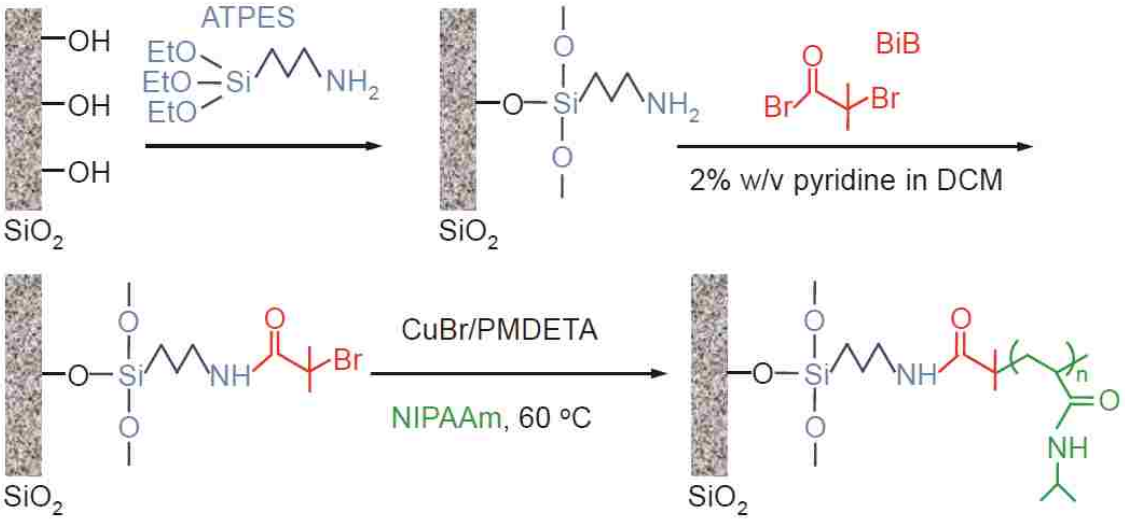

Figure 2.10 Schematic procedure of surface-initiated ATRP on silicon substrate.

1) Surface Cleaning. Glass slides/wafers were cut into small pieces (~1 cm × 1 cm). Glass and sands were washed with "piranha solution" (a mixture of 98 % sulphuric acid and 30 % hydrogen peroxide with volume ratio of 3:1) to remove organic contaminations on the surface. This process required careful handling since the solution reacts violently with organic materials. Then the glass and sands were rinsed with copious amount of deionized water, and oven dried. The cleaned surfaces were rendered hydrophilic due to the large number of -OH groups exposed on the surface.
2) Amino-silane deposition. Glass/sands were immersed into 1 % wt. APTES solution of toluene at room temperature for 12 hours. Then the substrates were rinsed with abundant toluene and acetone several times to remove the residual silane, and they were vacuum dried.
3) Initiator grafting. The NH_2-terminated glass/sands were put into a solution of dichloromethane containing 2 % w/v (weight/volume) pyridine. Then the mixture

was cooled down to 0 °C. The initiator BiB was added dropwise into the solvent containing the substrates. The mixture was kept at 0 °C for 1 hour, and then at room temperature for 12 hours. Following this treatment, the substrates were again cleaned with toluene and acetone, and vacuum dried.

4) Polymer synthesis. In this process, prior to their use, all solutions and flasks were thoroughly flushed with nitrogen to remove oxygen. First, 25 g NIPAAm were dissolved in a mixture of 100 mL of H_2O and 100 mL of MeOH to prepare a monomer solution. The solution was vacuum degassed with magnetic stirring. Then the silicon substrates with initiator already grafted on the surface were immersed into the monomer solution, accompanied with nitrogen purging. Second, an organometallic catalyst system was prepared by adding 317 mg (2.3 mmol) of Cu^IBr into a solution of 1149 mg PMDETA in 1 mL of methanol, accompanied by nitrogen gas blowing to prevent the Cu^+ from being oxidized. Then the system was sonicated for 1~2 min to let the Cu^IBr powder fully dissolve and facilitate the formation of Cu^IBr/PMDETA complex. The molar ratio between monomer/Cu^+/ligand was kept at 100/1/3, and the volume ratio of MeOH to water was fixed at 1/1. The catalyst solution was introduced into polymerization solution through a cannula with nitrogen gas purging to eliminate oxygen. Then the system was heated in a 60 °C water bath for 2 hours for the polymerization. The sample container was slowly rotated for mixing, instead of stirring to prevent the particles from grinding against each other. When the synthesis was completed, the substrate (silica sand) was filtered out and rinsed with acetone and DI water.

2.5 SURFACE CHARACTERIZATIONS

Characterization of surface-modified flat silicon substrates (glass slides/wafers) and the particles (sands) was performed using SEM (scanning electron microscopy), AFM (atomic force microscopy), FT-IR (Fourier transfer infrared spectroscopy), XPS (X-ray photoelectron spectroscopy), ellipsometry, and contact-angle goniometry.

2.5.1 Instrumentation

A Hitachi 4300SE/N system with an analytical high resolution (1.5 nm/30 kV) variable-pressure Schottky field-emission SEM (VP-FESEM), a light element energy dispersive X-ray analyzer (EDS), and electron backscatter diffraction (EBSD) camera was used to collect SEM images. A VASE ellipsometry system from J.A. Woollam Inc. was used to measure the thickness of the silane film and polymer brushes. A light source with wavelengths in the range (300 ~ 850) nm was used for these measurements. Two incident angles were selected (60° and 70°) to fit the model. XPS data were collected using a Scienta ESCA-300 spectrometer. In this measurement, a rotating Al anode serves as the X-ray source generating an Al Kα X-ray beam of 1486.8 eV photons. XPS data analysis was conducted with standard CaseXPS software package. The FT-IR spectra were obtained using a Thermo Scientific Nicolet iS10 spectrometer with 512 scans at 4 cm^{-1} resolution. The AFM was done using a Scanning Probe Microscope Solver NEXT from NT-MDT Co.

2.5.2 SEM characterization

Scanning electron microscopic images of polymer-coated and uncoated sand particles at different magnifications presented in Figure 2.11 show observation of the

surface morphology. The 120× image (2.11-a) shows that there are small cracks and bumps on the grain surface, greatly increasing the roughness of the surface. As the observation window is zoomed in, a greater number of micro-protrusions become visible on the surface (3k× image 2.11-c). The closest photo (2.11-d) with 10k× magnification illustrated the size and shape of the micro-protrusions (~hundreds of nanometers). SEM images of uncoated sand particle are presented in (2.11-e through 2.11-h). Similar micro-protrusions were also observed on uncoated surfaces. By comparing both coated and uncoated particle SEM images, it cannot be concluded with certainty that those micro-features are the polymer coatings. However, arrays of micro-strictures in nanometer scale significantly increased the roughness of the surface, and enhanced the surface hydrophobicity.

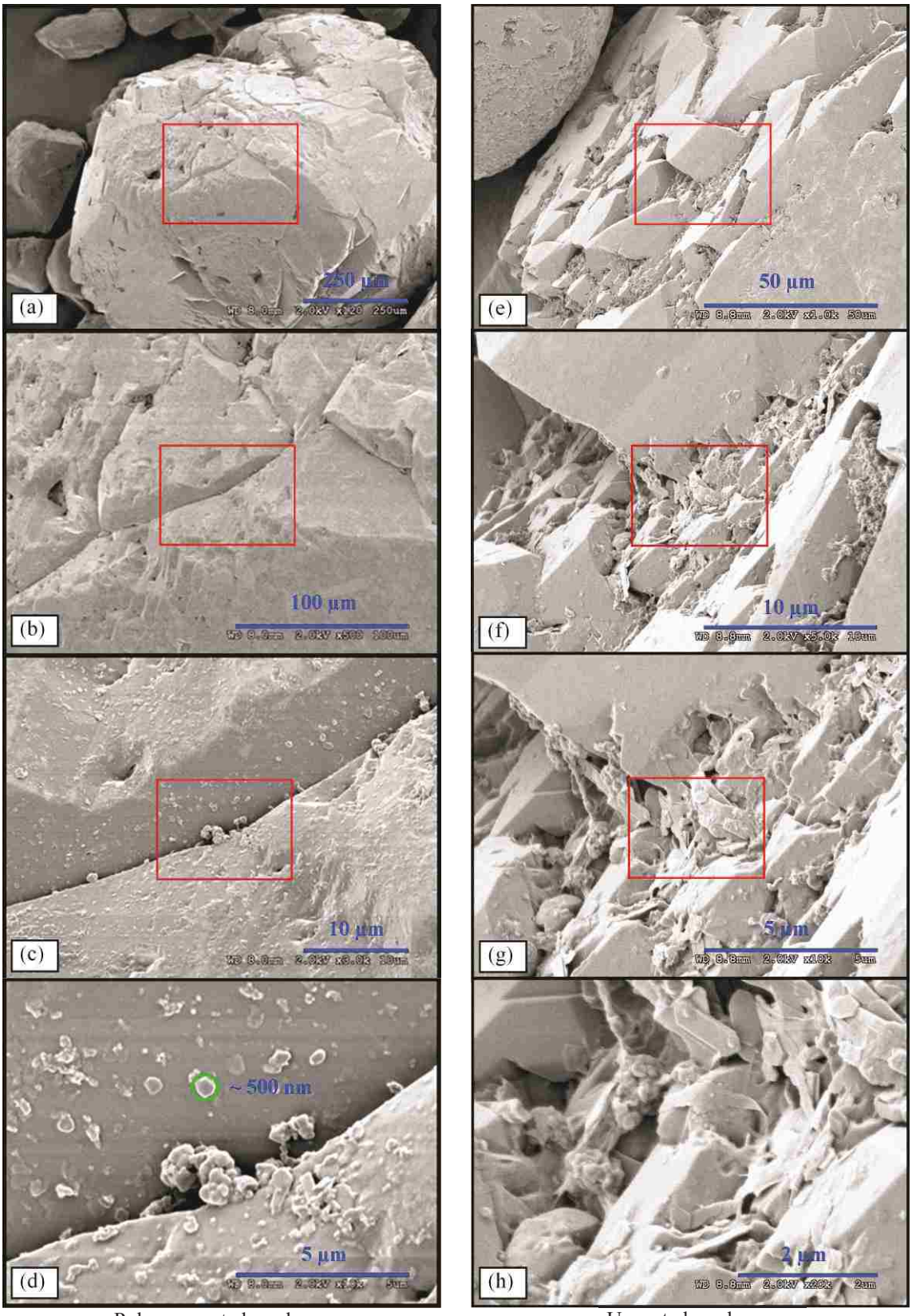

Polymer coated sand

Uncoated sand

Figure 2.11 SEM images taken of polymer-coated sand (Ottawa 20/30) at different magnifying scales: (a) whole sand particle of size ~0.75 mm, (b) zoomed in on a surface crack, (c) and (d) small features enhancing the surface roughness; and uncoated sand (e – h).

2.5.3 AFM characterization of surface–modified substrates

10×10 μm^2 square sections were examined on the treated surface after each step of the synthesis at 0.1 μm resolution of scan. Figure 2.12 below shows the evolution of the topological changes on the surface during the synthesis. Figure 2.12-a shows a micrograph of the cleaned silicon substrate. Except for some native roughness (the bright spots represent peaks), the surface appears smooth. After the treatment with the ATPES solution, the roughness grew and the average height of the asperities increased from 10 nm to 45 nm, as observed in Figure 2.12-b. After the polymer grafting is completed, the surface appeared to be covered by a rough polymer film, with the height of the roughness increased significantly to hundreds of nanometers, as shown in Figure 2.12-c.

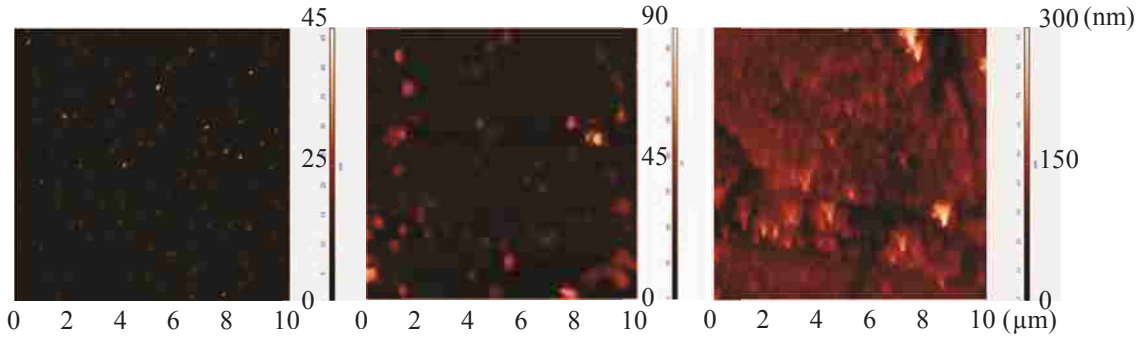

Figure 2.12 Surface topology of poly NIPAAm brushes on a silicon substrate.

2.5.4 FT-IR characterization of the PNIPAAm film

FT-IR was utilized to identify the functional groups present in the molecular structure. In order to facilitate the IR measurements, a single-sided polished silicon wafer was used to represent silica surfaces. The IR spectrum of PNIPAAm coated sample was collected by transmission of the IR beam through the wafer, and is presented in Figure 2.13. As depicted on the curve the absorption peaks verify the presence of PNIPAAm molecules on the substrate. The absorption peak at 3300 cm^{-1} is attributed to the stretch of the hydrogen-bonded NH group. The anti-symmetric stretching vibration of the CH_3 group occurs at 2970 cm^{-1}. The secondary amide C=O stretching gives rise to a strong bond at 1640 cm^{-1}. The last 1460 cm^{-1} peak is corresponds to the anti-symmetric bending vibration of CH_3 groups (Kaholek et al., 2004).

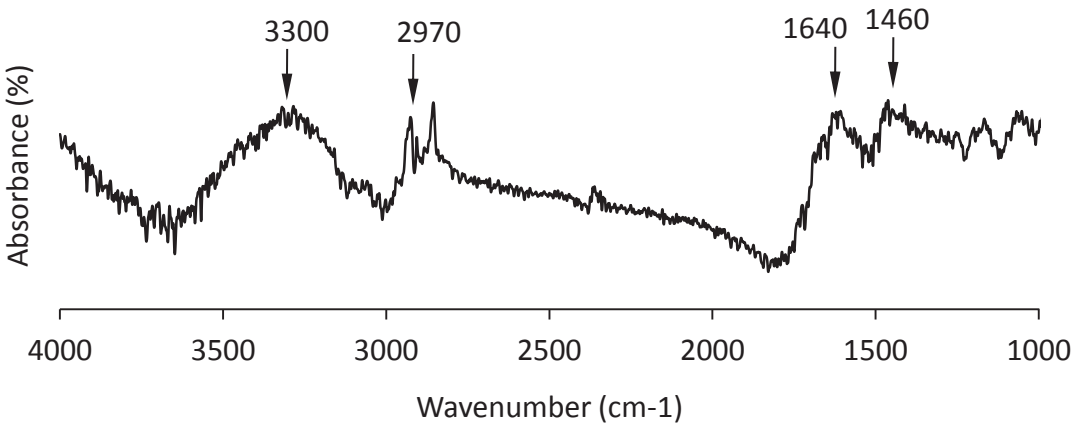

Figure 2.13 FT-IR spectrum of poly NIPAAm on Silica Wafer.

2.5.5 XPS characterization of surface modification

XPS was used to confirm the formation of the coupling agent, the initiator on the surface and successful polymerization of PNIPAAm (Tu et al., 2004). For most organic

polymers, the excited electrons can escape from a depth of ~10 nm with a 60° incident angle of X-ray. XPS data were collected from the freshly cleaned glass (silica) slides treated with APTES solution, then with initiator grafting, and finally after the ATRP synthesis.

The spectrum corresponding to each surface is plotted in Figure 2.14 (a). The first curve (SiO_2-Silane curve) shows one clear N (1s) peak at 398.4 eV and two Si peaks, Si (1s) at 167.6 eV and Si (2p) at 100.1 eV, as well as a large O (1s) peak which indicates a large amount of O element from silane and SiO_2 detected on the surface. After grafting the initiator, (SiO_2-Initiator curve), a significant peak for Br (3p) (182.0 eV) and Br (3d) (68.8 eV) occurred, and in contrast, the silicon peak weakened. Using the atomic concentrations calculated from the peak areas and the relative sensitivity factors, the C:N:O:Br ratio was determined as 55:11:22:9. This N/Br ratio is close to 1, which indicates a high coverage of bromine-ended initiator monolayer formed on the substrate surface. The third spectrum from polymer coated surface (SiO_2-PNIPAAm curve) only has C (1s) (285.0 eV), N (1s) peaks, and a greatly weakened O (1s) peak, which demonstrates that a thick polymer film was formed on the surface. Lack of Si peaks meant that no excited electron of silicon escaped from the surface, indicating a complete coverage of the surface by the polymer. The calculated C:N:O atomic concentration ratio equals to 77:10:13, which is close to the expected 75:12.5:12.5.

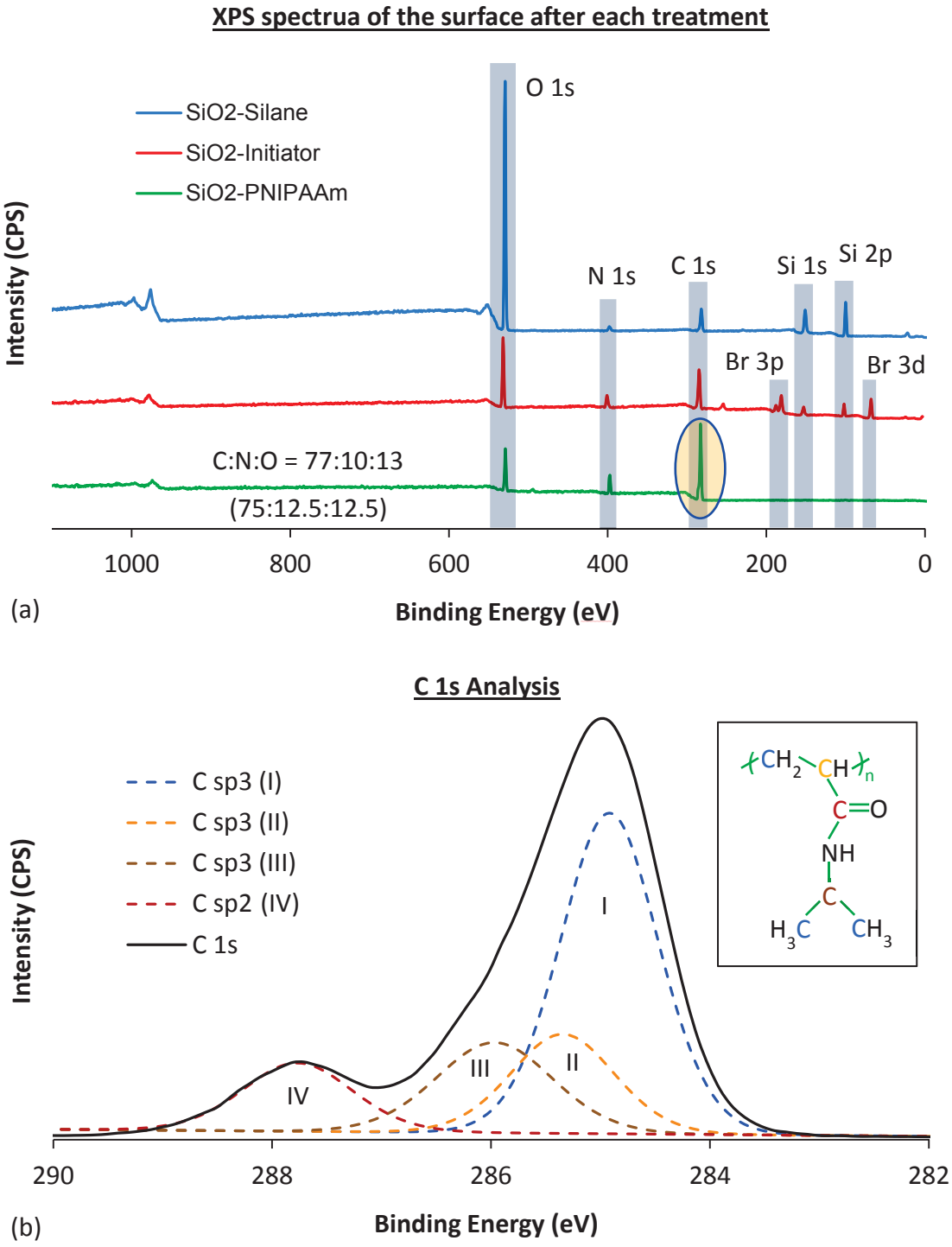

Figure 2.14 XPS spectra of surfaces of the modified substrates at each step of the synthesis (a), and peak fitting on high resolution of C 1s spectrum (b).

According to the references (Kong et al., 2001; Tu et al., 2004), a careful curve fitting on the high resolution C (1s) peaks resolved four peaks representing four different carbons in PNIPAAm. Figure 2.14-b demonstrates this C (1s) analysis. The sp^3-hybridized carbon peak at 285.0 eV was divided into three components: (1) aliphatic hydrocarbon (*C*-C/*C*-H, at a binding energy of 285.0 eV, labeled I), (2) an amide-induced *β*-shifted carbon (*C*-CONH at 285.5 eV, labeled II), (3) an amine-induced carbon shift (*C*-NH at 286.2 eV, labeled III), and the sp^2-hybridized carbon in the carbonyl group: (4) amide carbon (*C*ONH_2 at 287.9 eV, labeled IV) has an molar ratio of 15 %, which is close to the theoretical value 16.7 %. A molar ratio of ~3:1:1 for the three components I:II:III, yielded a match of the overall shape of the sp^3-hydridized carbon peak, confirming the chemical composition of the grafted PNIPAAm brushes.

2.5.6 Ellipsometry measurements

The single-side polished silicon wafer was used to determine the thickness of the polymer film. The PNIPAAm was synthesized following the same procedure described above and the thickness of each film was measured sequentially. Table 2.1 lists the measured thickness of the built layers following each treatment. When the wafer surface was cleaned by piranha solution, a thin native oxide film was formed with thickness of ~2.2 nm, which is in accordance with the typical values reported in literature (Aswal et al., 2006). Coating amino-terminated silane provided a thick siloxane layer with siloxane bonds to the surface. The thickness of this layer greatly depended on the concentration of the silane and the reaction time. Finally, the thickness of poly-NIPAAm was determined as approximately 20 nm.

Table 2.1 Thicknesses of each coating layer.

Layer of coating	SiO_2	Silane layer	PNIPAAm layer
Thickness (nm)	2.2	19.2	19.0

2.6 CONCLUSIONS

Several surface-coating approaches were compared and summarized. Among these methods, ATRP was evaluated to be an efficient and robust technique to graft functional films on the substrate surface. Various characterization methods were used to monitor the quality of each process step, and verify the products built on the surface.

The XPS results indicated that a PNIPAAm coating can be successfully grafted onto the surface. The NIPAAm polymer formed a thick uniform film on the sand with adequate coverage.

CHAPTER 3

INTERFACIAL INTERACTION BETWEEN PARTICLE AND FLUID

3.1 INTRODUCTION

The surface properties of soils define the wetting behavior of associated fluids. The interaction between mineral surfaces and fluids, in turn, governs the transport and fate of fluids and organic substances existing in pore spaces. Solid minerals that consist of soil particles naturally have high surface free energies that attract water (Rodriguez and Newaz, 1988). On the other hand, surfaces coated with hydrophobic materials show strong affinity to organic fluids and substances. Hydrophobic surfaces tend to exclude water from particle surface, which is generally important for the diffusion of solutes in the pore water, thus acting as a diffusion barrier (Goebel et al., 2007). The thickness of water films on hydrophilic surfaces are ten times (~300 nm) greater than that on hydrophobic surfaces (~30 nm) when soils are wet (Derjaguin and Churaev, 1986). Preliminary experiments in our lab showed that coating the soil surface with the organosilane (*n*-octyltriethoxysilane, $C_8H_{17}Si(OCH_2CH_3)_3$) increased the water repellency of soils as shown in Figure 3.1 and created unusual interactions between soil particles and fluids.

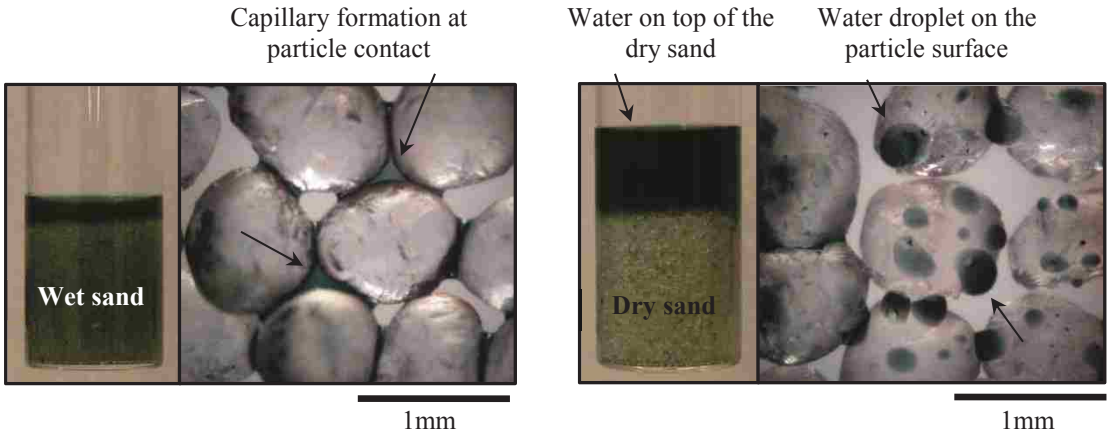

(a) Hydrophilic sand (wettable sand)

(b) Hydrophobic sand (water-repellent sand)

Figure 3.1 Wetting and water-repellent behaviors of hydrophilic and hydrophobic sand (Ottawa 20/30 sand, D_{50} = 0.72 mm). Sand was cleaned with piranha solution to remove impurities on the surface before treating with organosilane. The thickness of organosilane coated on the surface is estimated to be less than ten of nanometer (Sun et al., 2002).

While the water infiltration and capillary formation at inter-particle contacts are evident in hydrophilic sand (Figure 3.1-a), the hydrophobic sand does not allow water to permeate into the pore space and instead the water form "ball" shapes on the particle surface (Figure 3.1-b). This difference shows clearly that surface can control the spatial distribution of participating fluids in the pore space. Consequently, the physical properties of soils with different surface wettabilities can vary substantially at the macro-scale (Frattolillo et al., 2005; Nguyen et al., 1999).

3.2 CONTACT ANGLE AND WATER PENETRATION

3.2.1 Contact-angle measurement

Contact angles were measured for PNIPAAm-grafted glass slides under different temperatures. The images in Figure 3.2 depict the changing wetting behavior of the polymer modified glass surface with temperature. At low temperatures (< ~32 °C), the surface is hydrophilic with a contact angle of around 30°, while when the substrate is slightly heated up over the LCST (> ~32 °C), the surface turns hydrophobic with a contact angle greater than 90°. In essence, this test straightforwardly proves that by simply modifying the material surface at nano-scale, the property at macro-scale can be altered tremendously.

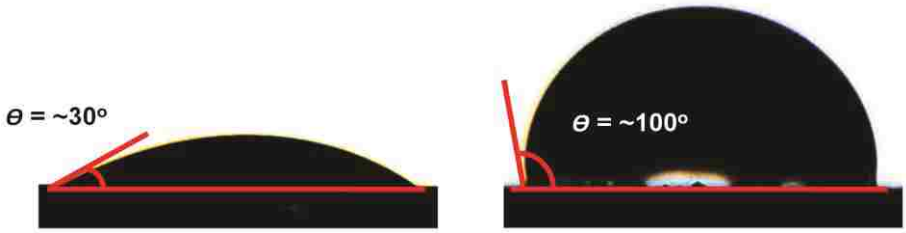

Figure 3.2 Contact angles of PNIPAAm-grafted flat surfaces at low temperature (20 °C, left), and high temperature (50 °C, right).

3.2.2 Water penetration test

A simple water-penetration test was conducted to demonstrate the wettability change induced by temperature change in surface modified sands. Both the fine size sands and the coarse size sand samples were grafted with PNIPAAm using surface-

initiated ATRP technique described in Chapter 2. As shown in Figure 3.3, a small amount of the modified sands were placed in vials immersed in a temperature-controlled water bath system. The water was heated to 50 °C, and then kept at this temperature for long enough time to warm the sand samples. At 50 °C, the modified surfaces turned hydrophobic, indicated by the red line delineating the water front (left pictures in Figure 3.3-a, b) that remained on the top of the sands. Due to the thermally triggered hydrophobicity, the sand surface prevented water to penetrate through the sand bed. Upon cooling the samples down to room temperature, ~20 °C, the polymer-coated sands became hydrophilic, hence allowing the pooled water to infiltrate and saturate the sands.

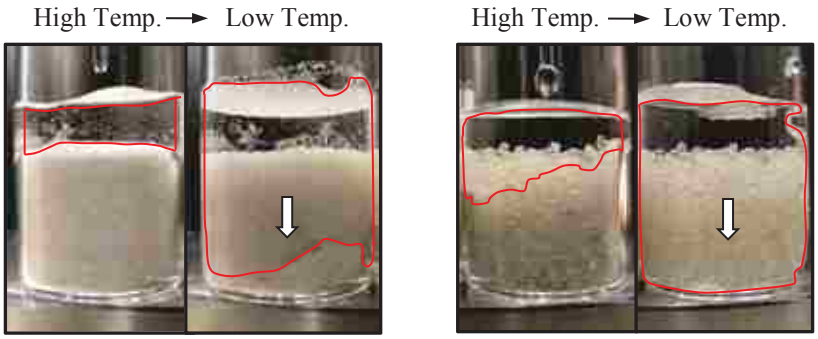

(a) Fine sands with PNIPAAm coated (b) Coarse sands with PNIPAAm coated

Figure 3.3 Water penetration in PNIPAAm coated (a) fine sands (Ottawa F110), and (b) coarse sands (Ottawa 20/30).

3.3 PARTICLE-WATER INTERACTION AND PORE WATER DISTRIBUTION

Optical observation was conducted to capture the characteristics and evolution of pore water distribution at various levels of saturation for soils presenting different surface wettabilities.

3.3.1 Method

The polymer-coated sands (Ottawa 20/30) were synthesized according the procedures described in Chapter 2. A number of small "Hele-Shaw" cells (with 10 mm × 10 mm ×1 mm cavity) were constructed using glued rectangular pieces of transparent glass slides (Fisher brand pre-cleaned plain microscope slides), as sketched in Figure 3.4. The glass cell was sealed at the top after a single-grain thick layer of synthesized sand particles sandwiched in between the top and bottom plates were wetted at the desired degree of water saturation. When the entire system was kept in room temperature (~20 °C), the sands were hydrophilic. The cell was then heated up to 50 °C, when the polymer-coated sands became hydrophobic (T > 32 °C). The sealed cell was kept at constant temperature over long enough time for the water-vapor system to reach the evaporation-condensation equilibrium.

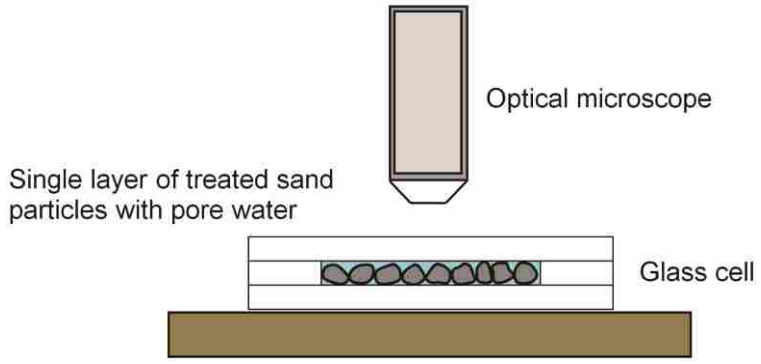

Figure 3.4 Schematic illustration of microscope and customized glass cell for particle observations.

3.3.2 Results and discussion

Figure 3.5 and Figure 3.6 present the microscopic photographs of the pore water distribution at different degrees of saturation for the hydrophilic and hydrophobic sands, respectively. For hydrophilic sands, liquid bridges, connecting only *two* particles, are formed at the very low degree of saturation (Figure 3.5-a). As the water content increases, the capillary bridge size extends to the adjacent pore where the water forms trimers, which tied *three* particles together (Figure 3.5-b). More water content leads to coalescence of two trimmers into a pentamer cementing *five* particles (Figure 3.5-c). Thus, for unsaturated sands at pendular stage, the long range fluid connectivity is well established as connected thin water film surrounding the particles to facilitate the heat conduction and electron movement. This feature is captured later in this dissertation by results of salient increase of thermal and electrical rise at low saturation state of the sands (see results in Chapter 5.2). At medium saturation, pore fluid has started to occupy more

of the pore space and encompassing whole particles (Figure 3.5-d). At this stage, the water phase dominates both the thermal and electrical conduction of the medium. Reflected on the test results, hydrophilic sands gain maximum thermal and electrical conduction capability at ~50 % degree of saturation (see Figure 5.6 and Figure 5.8).

In contrast, hydrophobic sands have fairly different evolution of the patterns of pore-water distribution. At low water content, hydrophobic sands form water droplets that stay in the pore space, and they can hardly wet or bridge particle contacts (Figure 3.6-a, b). At a medium degree of saturation, the water beads expand in size and fill more of the pore space (Figure 3.6-c), but still less of them contribute to particle contacts, which result in a poor fluid connectivity. This feature of hydrophobic sands was exemplified by a gradual build-up of thermal conductivity with degree of saturation S from 20 % to ~ 60 % (see discussion in chapter 5.2.2). While water dominates the void space with increased saturation, the "water-hating" nature of hydrophobic surface exhibits "air-loving" behavior. When water occupies more of the pore size, air builds up at the particle contacts (Figure 3.6-d). As the volumetric fraction of water continues to increase, the trapped air bubbles adhere to the mineral surface rather than freely sojourning in the pore water (Figure 3.6-e, f). This process reduces the area of solid-liquid contact, which makes a severely hindered connectivity path of pore fluid forming at medium to high saturation for hydrophobic sands. Therefore, hydrophobic sands show a very gradual increase in thermal conductivity and reach the upper bound only near 80 % saturation. The electrical conductivity is also poorly developed under 80 % of degree of saturation for these sands (see more discussion in section 5.2.2 and test results in Figure 5.6, Figure 5.8).

The particle-water interaction and pore-fluid distribution for both the hydrophilic and hydrophobic sands become similar at high fractions of water volume, and the effect of surface wettability diminishes.

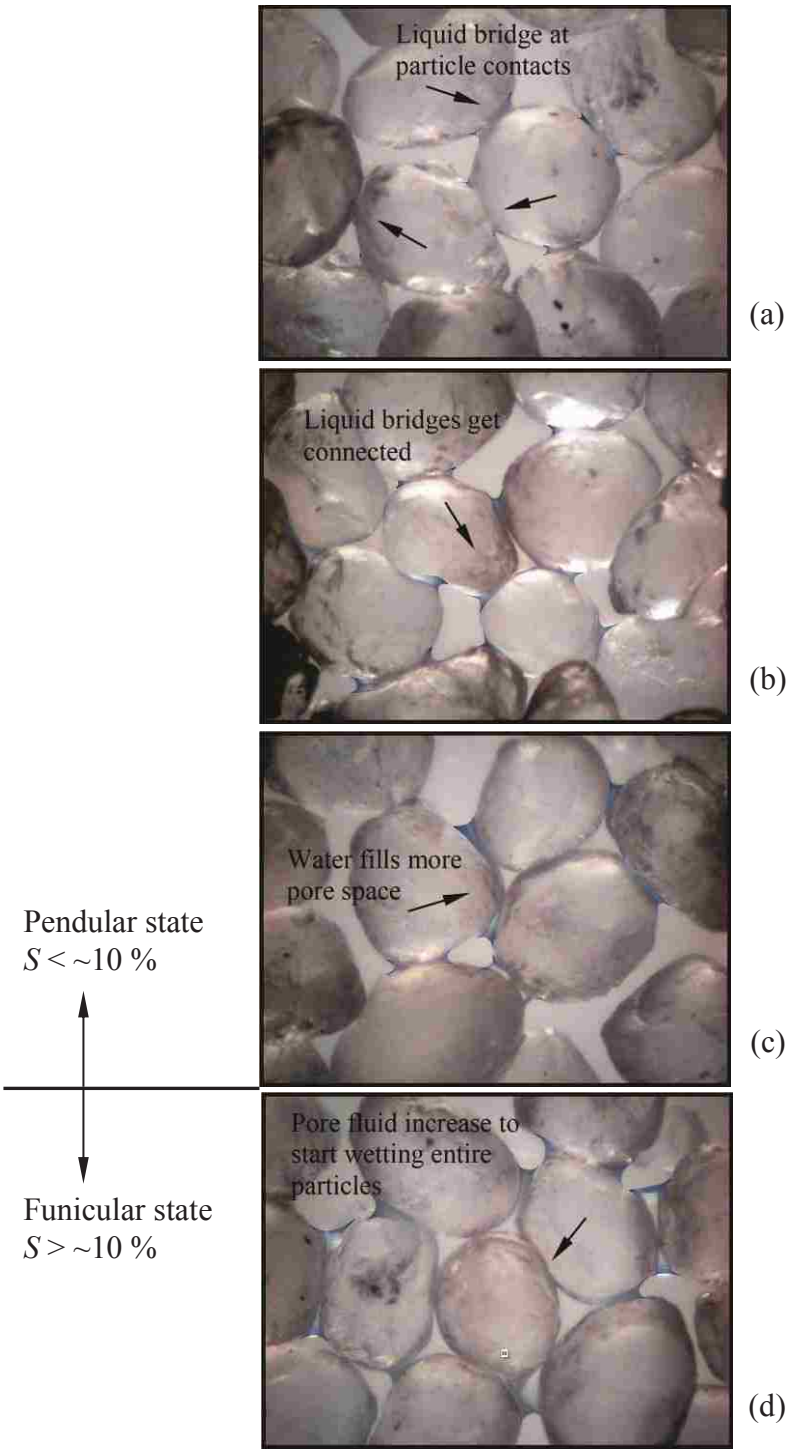

Figure 3.5 Pore-fluid distribution and water-particle contact as the degree of water saturation increases (a-d) in hydrophilic sands (the color of pore water has been edited to highlight the interfaces).

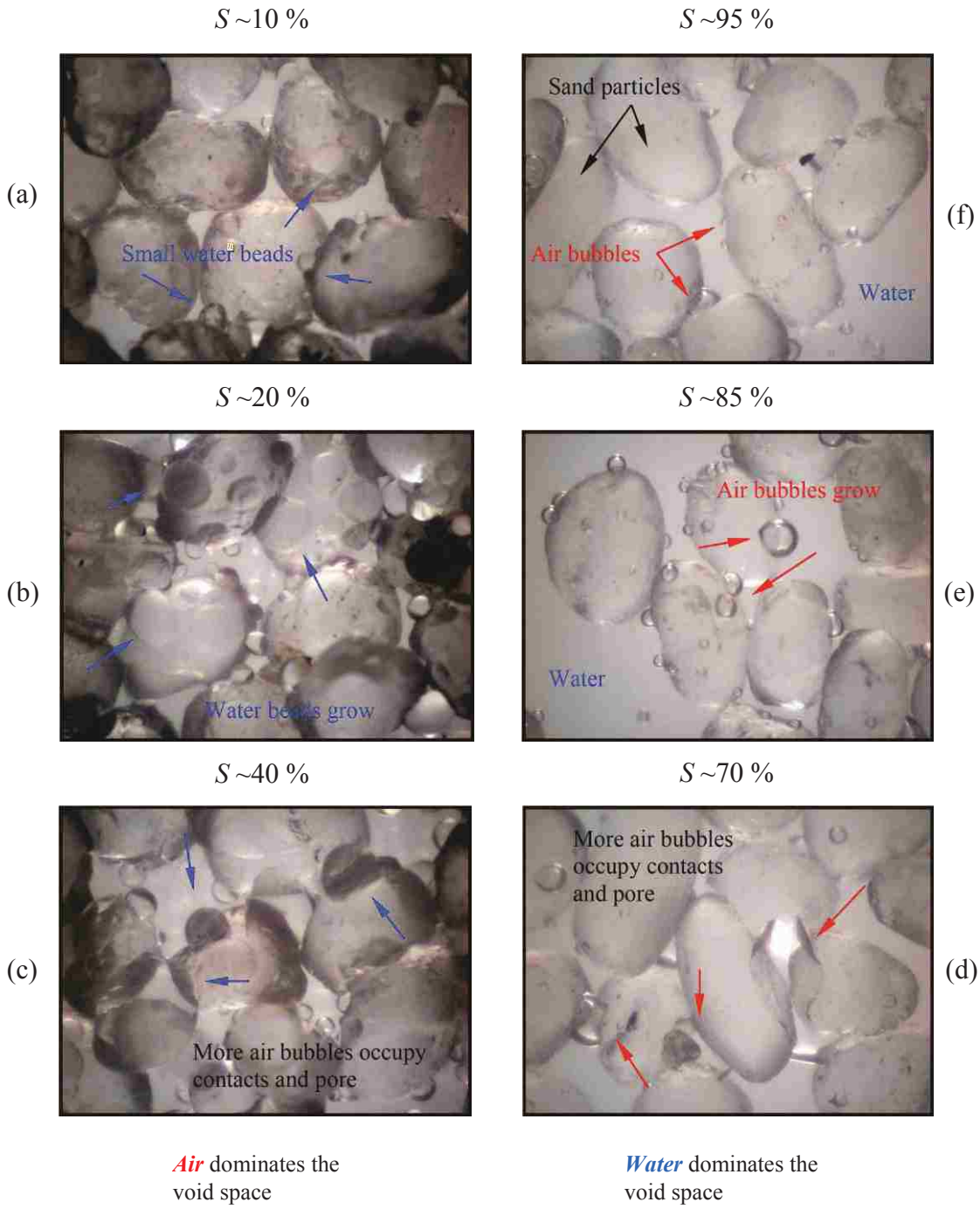

Figure 3.6 Pore-fluid distribution and water-particle contact as the degree of water saturation increases in hydrophobic sands (a-c: air occupies more void space, d-f: water occupies more void space).

3.4 CONCLUSIONS

The contact-angle measurements of the reference surface prove that the polymer coating modifies the wettability of the surface at elevated temperature with a large contact angle ($> 90°$), showing strong hydrophobicity. At macro level, the hydrophobicity renders bulk sands impermeable and prevents liquid water from penetrating through the body.

Particle-level observation reveals the pore-fluid distribution has totally different patterns for hydrophilic and hydrophobic granular materials. In the unsaturated condition, pore fluid tends to stay at the particle contact forming water film or liquid bridge which creates high pore-fluid connectivity in hydrophilic sands, while pore liquid is squeezed into pore space that hinders the development of conduction paths between the networks of pores.

CHAPTER 4

CAPILLARY EFFECT AND SMALL-STRAIN STIFFNESS

4.1 INTRODUCTION

The capillary force between particles is dominated by the interfacial free energy of interfaces among solid, liquid and vapor phases, the contact angle, the particle size, and the volume of liquid present between particles. Moreover, the interplay between the contact angle and the position of tangential point of liquid on the particle surface defines the unique profile of liquid bridge to produce the inter-particle capillary force.

A numerical simulation was conducted to analyze the relationship between capillary pressure (force) and water volume at the particle level. The capillary effect was captured by using a nondestructive testing approach (shear wave velocity) for sands with different surface wettability.

4.2 NUMERICAL STUDY OF CAPILLARY

4.2.1 Physical model and governing equations

Governing Equations

Figure 4.1 portrays a simple physical model for the equilibrium profile of a liquid bridge between two identical spherical particles under the point-contact condition (i.e., no

separation between particles). The axisymmetric condition allows us to consider the "0123" region in Figure 4.1 to evaluate the capillary force and pressure where $y(x)$ is the function that describes the profile of liquid-vapor interface, $u(x)$ is the profile of particle shape, x_p and y_p are abscissa and ordinate of the tangential point "2", θ is the contact angle of liquid-solid interface, α is defined as half filling angle at tangential location of liquid bridge at point "2". Note that both α and θ determine the volume of liquid bridge. The characteristic profile of this model is the solution based on the minimization of the total free energy A in a closed solid-liquid-vapor system with negligible gravitational distortion assumption.

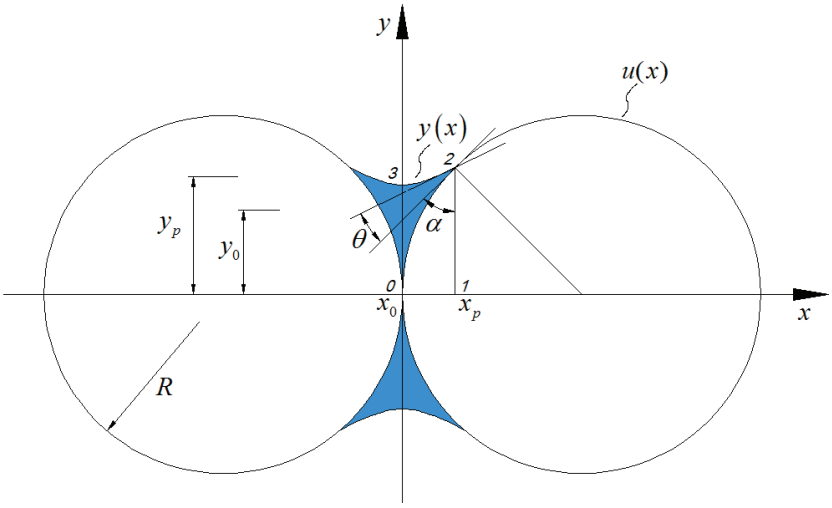

Figure 4.1 Two identical sphere particles model with liquid bridge connects at the particle contact.

The total free energy, A, of this system is expressed as a functional equation (De Bisschop and Rigole, 1982):

$$A = 2\int_{x_0}^{x_p}\left[\gamma_{lv}\cdot 2\pi y\left(1+y'^2\right)^{0.5} + (\gamma_{sl}-\gamma_{sv})\cdot 2\pi u\left(1+u'^2\right)^{0.5} + P_v\cdot\pi\left(y^2-u^2\right)\right]dx \qquad \text{Eq. 4-1}$$

where P_v is the pressure in the vapor phase, and γ_{lv}, γ_{sv}, and γ_{sl} are interfacial free energies of liquid-vapor, solid-vapor, and solid-liquid interfaces respectively. Eq. 4-1 consists of three components: interfacial free energy on the liquid-vapor interface, interfacial free energy on the solid-liquid interface, and the effect of pressure of the liquid body. The liquid profile $y(x)$ meets the requirement of minimizing the total free energy A under the constraint condition of a constant volume of the liquid bridge, V_l, given in Eq. 4-2.

$$V_l = 2\int_{x_0}^{x_p}\left[\pi\left(y^2-u^2\right)\right]dx \qquad \text{Eq. 4-2}$$

The minimization of total free energy is essentially a problem of conditional variation with movable boundaries which is solved by introducing a Lagrange multiplier λ using variational calculus and it eventually leads to Laplace's Theorem (Adamson and Gast, 1997):

$$\lambda - P_v = \gamma_{lv}\left[\frac{1}{y\left(1+y'^2\right)^{0.5}} - \frac{y''}{\left(1+y'^2\right)^{1.5}}\right] \qquad \text{Eq. 4-3}$$

Then, Eq. 4-3 defines capillary pressure or matrix suction (Nelson and Miller, 1992). The Lagrange multiplier λ turns out to be the pressure of liquid phase. The differential pressure between two sides of the liquid-vapor interface is equal to the surface tension on the interface multiplied by the average radius of curvature of the interface. Eq 4-4 shows the proposed solution (De Bisschop and Rigole, 1982).

$$\frac{y}{\left(1+y'^2\right)^{1/2}} = \frac{\left(\lambda - P_v\right)}{2\gamma_{lv}}y^2 + C \qquad \text{Eq. 4-4}$$

where C is the integration constant expressed as in Eq. 4-5:

$$C = y_p \sin(\alpha+\theta) - \frac{(\lambda - P_v)}{2\gamma_{lv}} y_p{}^2 \text{ or } C = y_0 - \frac{(\lambda - P_v)}{2\gamma_{lv}} y_0{}^2 \qquad \text{Eq. 4-5}$$

For a given set of contact angle θ and half-filling angle α, the ratio $(\lambda\text{-}P_v)/\gamma_{lv}$ and the integration constant C, Eq. 4-5 can be determined as the coordinates of point "2" (x_p, y_p) or point "3" (0, y_0) in Figure 4.1, as given below:

$$\frac{y_p}{(1+y_p{}'^2)^{1/2}} = \frac{(\lambda - P_v)}{2\gamma_{lv}} y_p{}^2 + C \text{ or } \frac{y_0}{(1+y_0{}'^2)^{1/2}} = \frac{(\lambda - P_v)}{2\gamma_{lv}} y_0{}^2 + C \qquad \text{Eq. 4-6}$$

The constant C can be obtained with the boundary conditions set as $y_p' = 1/tan(\alpha+\theta)$ and $y_0' = 0$. Finally, the transformation of Eq. 4-5 and Eq. 4-6 results in Eq. 4-7:

$$2\pi C \cdot \gamma_{lv} = 2\pi y_p \sin(\alpha+\theta)\cdot\gamma_{lv} + \pi y_p{}^2 \cdot (P_v - \lambda) = 2\pi y_0 \cdot \gamma_{lv} + \pi y_0{}^2 \cdot (P_v - \lambda) \qquad \text{Eq. 4-7}$$

The quantity $2\pi C\cdot\gamma_{lv}$ is found to represent the total adhesion force acting on the spheres. This equation indicates that the adhesion force is made up of two parts (Lian et al., 1993), as shown in Figure 4.2. One part is the surface tension of the liquid, $2\pi y_0\cdot\gamma_{lv}$ at the central section or the horizontal component $2\pi y_p\, sin(\alpha+\theta)\cdot\gamma_{lv}$ at $x = x_p$ plane on the three-phase contact line. The other part is the attractive hydrostatic pressure acting on either section due to the pressure difference $\pi y_p{}^2\cdot(P_v\text{-}\lambda)$.

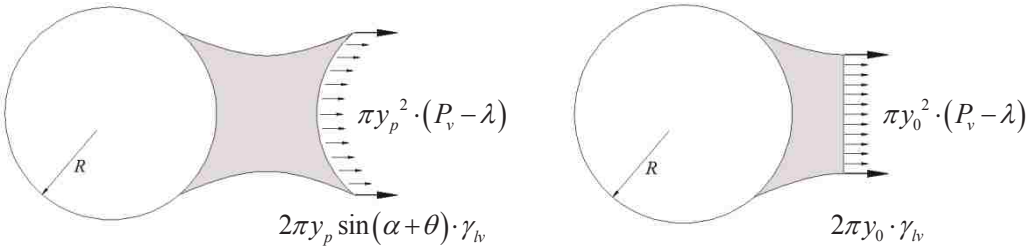

Figure 4.2 Equivalent components comprise the adhesion force resulted from capillarity between two particles: (1) interfacial free engergy either on liquid-vapor-solid interfaces (meet at a line, left) or liquid-vapor interface circled the cross section in middle of the liquid bridge (right), and (2) liquid-vapor pressure difference applied on either solid particle (left) or on the cross-section in the middle of the liquid bridge (right).

4.2.2 Liquid-bridge simulation and capillary analysis

Liquid profiles between spheres

The radius of a sphere is selected as R = 0.36 mm to correspond to the Ottawa 20/30 sand (D_{50} = 0.72 mm) of the experimental study. For a set of given values of contact angle and half-filling angle (see definition in Figure 4.1), the differential equations ($\partial A/\partial y = 0$) are numerically solved in Matlab with the aid of the modified Euler method to evaluate both the capillary force and capillary pressure (Lian et al., 1993). The set of capillary forces and pressures is obtained with the possible combinations of both the contact angle (10° to 150°, every 10°) and the half filling angle (15° to 65°, every 10°) to map the correlation between capillarity and the governing factors.

Selected profiles of liquid bridges at equilibrium are shown in Figure 4.3. Figure 4.3-a illustrates the case of constant contact angle $\theta = 30^\circ$ with variable half filling angles. The formation of liquid bridge for $\theta = 100^\circ$ is shown in Figure 4.3-b. The values of contact angles were selected to correspond with the measured contact angles from the experimental study (see Figure 3.2). Solid lines in red color represent the liquid bridges on hydrophilic particles, while blue lines are those on hydrophobic surfaces. Note that the case of $\theta = 100^\circ$ and $\alpha > 65^\circ$ in Figure 4.3-b cannot be defined because the convex shape of the liquid bridge cannot hold such a large contact angle with a high volume of liquid, where it begins interfering with the neighboring liquid bridges in the bulk system. Figure 4.3-c shows the gradual change of liquid volume with increasing contact angle at the constant half-filling angles of $\alpha = 35^\circ$ and 55°. For each case of half-filling angle and contact angle, capillary forces and pressures are obtained following the principle of minimization of total surface free energy described in section 4.2.1.

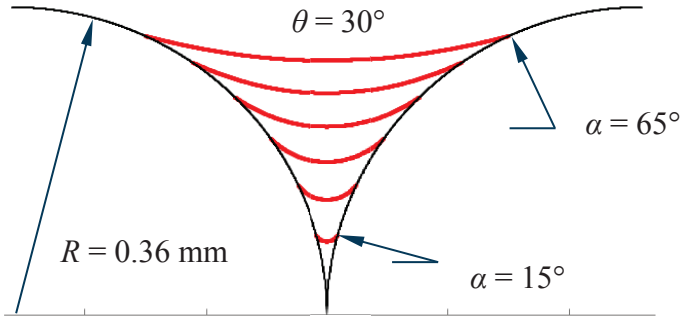

(a) Formation of liquid bridge, $\theta = 30°$

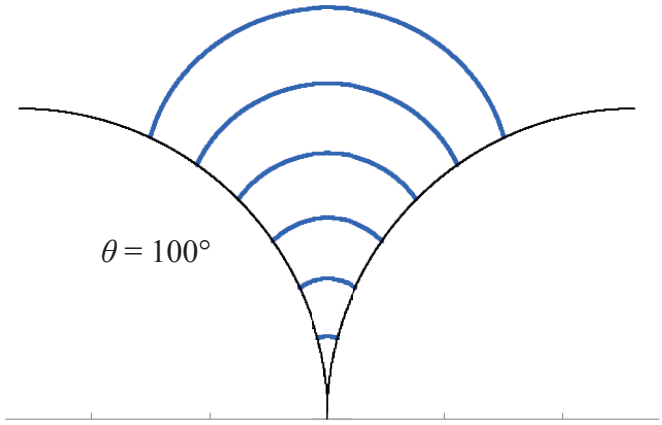

(b) Formation of liquid bridge, $\theta = 100°$

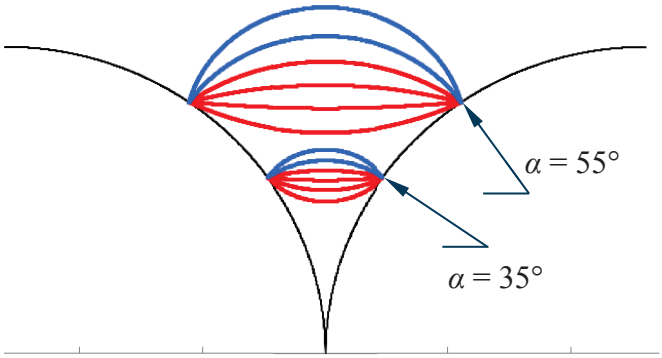

(c) Formation of liquid bridge with a range of θ at constant α.

Figure 4.3 Liquid-bridge profiles at (a) constant $\theta = 30°$, (b) constant $\theta = 100°$, and (c) varying contact angles at constant half-filling angles $\alpha = 35°$ and 55°. Red color represents hydrophilic and blue hydrophobic.

Figure 4.4 shows that the volume of liquid bridge increases as the half-filling angle and contact angle increase due to the inherent geometric profile of the liquid bridge shown in Figure 4.3. Again, red color lines and hollow markers represent hydrophilic surface (contact angle < 90°), blue lines and solid markers present hydrophobic ($\theta > 90°$), and the black line and cross marker are for a neutral surface ($\theta = 90°$). Note that the volume of the liquid bridge is normalized by the volume of the spherical particle, being

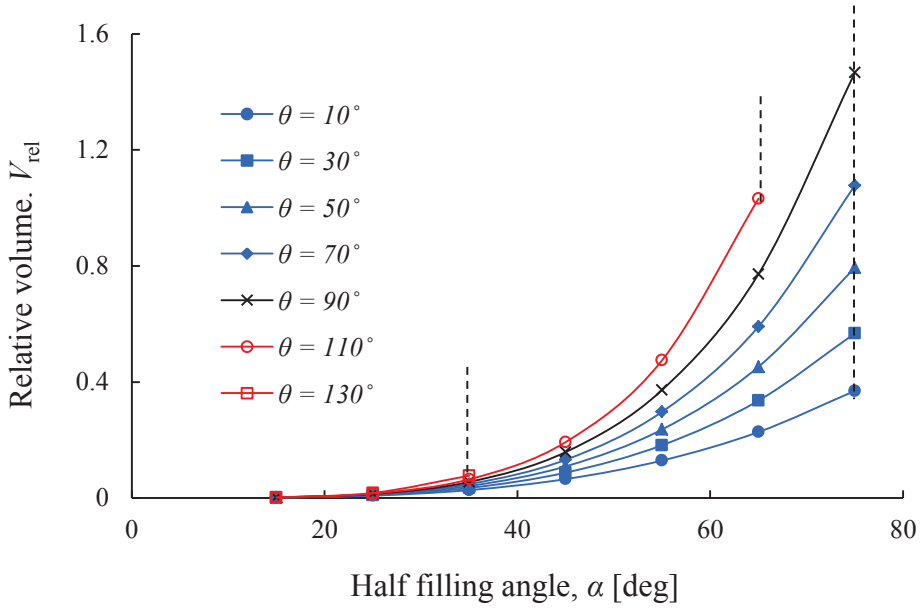

Figure 4.4 Increase of relative volume V_{rel} with half filling angle α depending on the contact angle θ. Red color represents hydrophilic, black for neutral, and blue for hydrophobic.

expressed as relative volume $V_{rel} = V_l/V_s$ (Megias-Alguacil and Gauckler, 2009). The incremental ratio is magnified for larger values of α and θ. The dotted lines in Figure 4.4 delineate the upper bound of possible formation of the liquid bridge for the given values

of contact angle. Higher contact angles have a lower value of upper bound in half-filling angle to form the liquid bridge.

Evolution of capillary force and capillary pressure

The capillary force computed in Eq. 4-7 is plotted with a range of contact angles and relative volumes in Figure 4.5-a. The capillary force is expressed in the dimension-less form as $F_{norm} = F_{cap}/(\gamma \cdot R)$ where γ is the surface tension (71.97 mN/m for water at 25°C temperature) and R is the radius of the sphere. The capillary force decreases with increasing relative volume caused by growing half-filling angle. As the cross-sectional area increases with increasing α, the force due to the surface tension in Eq. 4-7 increases. As a result, the capillary force decreases with increasing half-filling angle. The capillary force for lower values of contact angle ($\theta < \sim 50°$) remain in attraction regime while the repulsive capillary force prevails at higher contact angle ($\theta > \sim 85°$) for the entire range of relative volume. As the relative volume decreases (e.g., equivalent to decreasing degree of saturation of water during evaporation), the capillary force sharply increases at lower value of V_{rel} (note that the x-axis is in logarithmic scale). It should be noted here that the capillary force runs across the boundary between attraction and repulsion as the relative volume decreases when θ ranges from 50° to 85°. Figure 4.5-b shows the boundary between repulsive and attractive forces depending on the relative volume and contact angle delineated by the zero-capillary force as a function of relative volume. The values for this plot were obtained when the computed capillary force changed its sign from positive (attraction) to negative (repulsion) by the cubic-spline interpolation of data

in Figure 4.5-a. As observed, the higher contact angle has lower value of relative volume in order to maintain attractive force.

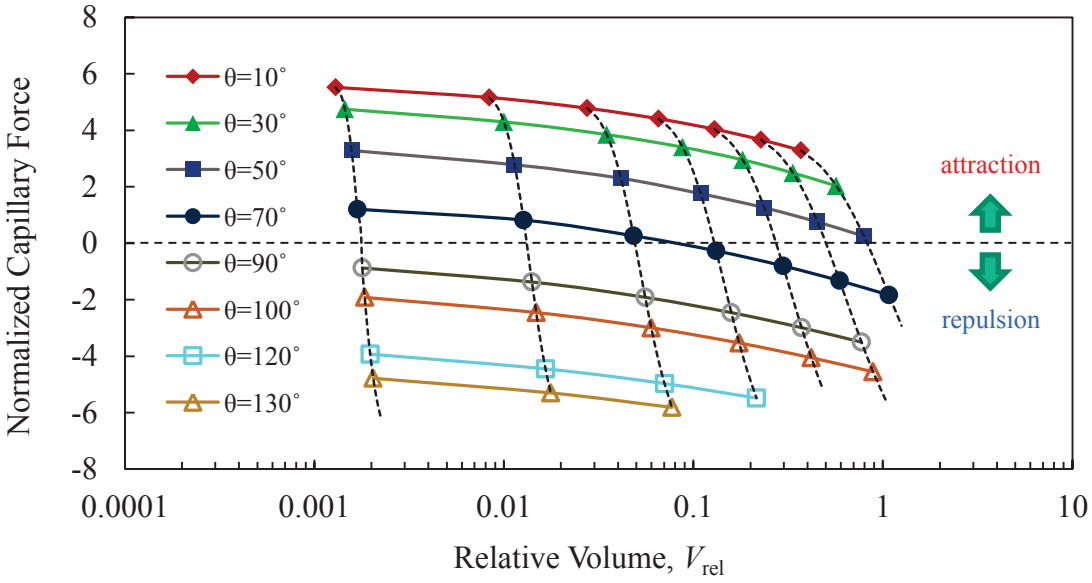

(a) Capillary force with relative volume of liquid: hydrophilic in solid markers, hydrophobic in hollow markers (including nuetral).

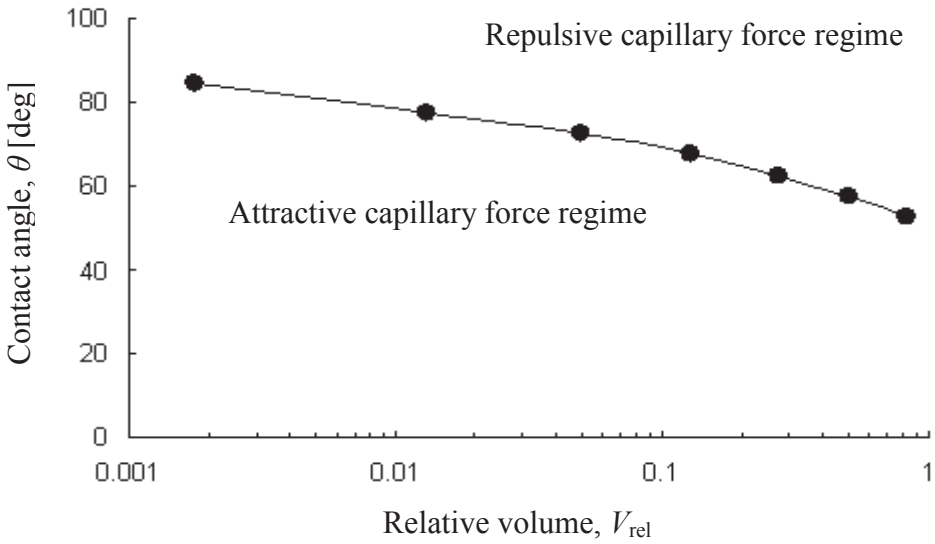

(b) Attractive and repulsive capillary force boundary.

Figure 4.5 Capillary force. (a) Evolution of capillary force with relative volume of water V_{rel} depending on the contact angle θ. (b) Attractive and repulsive capillary force regimes defined by contact angle and relative volume.

Figure 4.6-a shows the normalized capillary pressure variation for a range of contact angles and relative volume, where capillary pressure is expressed in the dimensionless form as $P_{norm} = P_{cap} \cdot R/\gamma$. The capillary pressure was obtained as the pressure difference between vapor and liquid phase, which is proportional to the curvature of liquid bridge described in Eq. 4-6. The independently computed values of force and pressure were validated using the relation between capillary force and pressure as [F_{cap} = *Surface tension* – (P_{cap} × *Cross sectional area*)]. Unlike the capillary force, the capillary pressures at high relative volume, reside in minor repulsion state close to zero value for all contact angles, which is analogous to the highly saturated condition. As the relative volume decreases (e.g., decreasing degree of saturation as liquid evaporates), the attractive capillary pressure develops gradually for lower contact angles and the repulsive capillary pressure develops for higher contact angles.

This solution shows that the capillary pressure between particles becomes more pronounced at smaller values of contact angle and low degrees of saturation. The magnitudes of the contact angle and relative volume determine the direction of pressure, either negative (attraction) or positive (repulsion). The boundary between the attractive and repulsive capillary pressure is shown in Figure 4.6-b. The capillary pressure between particles falls into the attraction zone when the relative volume is relatively small for small contact angles. Similar to the capillary force, lower value of relative volume (e.g., low degree of saturation in bulk soils) is necessary for attractive pressure to develop at higher contact angles.

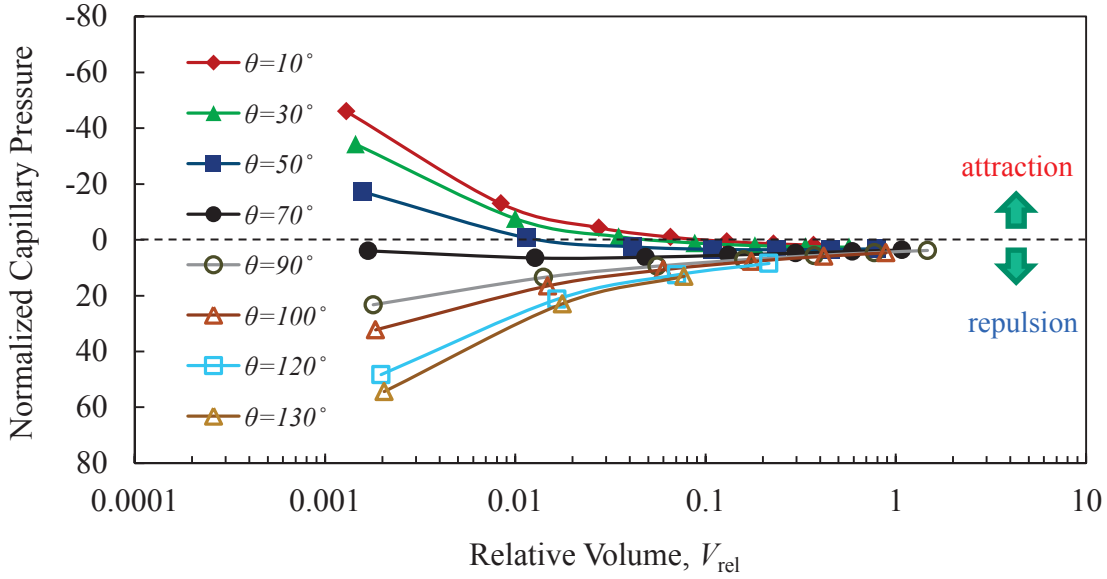

(a) Capillary pressure with relative volume of liquid: hydrophilic in solid markers, hydrophobic in hollow markers (including neutral).

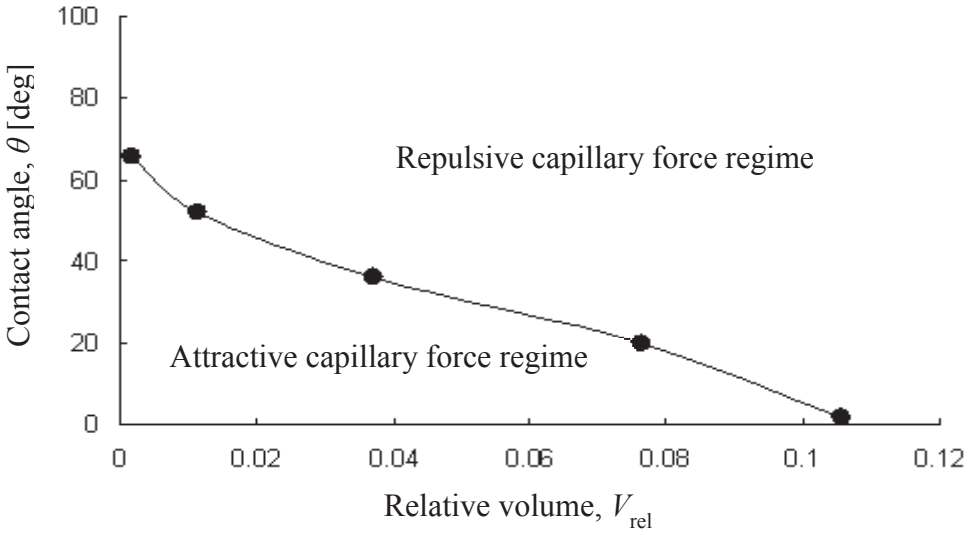

(b) Attractive and repulsive capillary pressure boundary.

Figure 4.6 Capillary pressure. (a) Evolution of capillary pressure with relative volume of water V_{rel} depending on the contact angle θ. (b) Attractive and repulsive capillary pressure regimes defined by contact angle and relative volume.

4.3 EXPERIMENTAL STUDY

4.3.1 Method

Materials

Glass beads were selected to represent ideal sphericity with median diameter, D_{50} = 0.72 mm. The ideal sphericity minimizes the effect of particle shape and roughness, and facilitates the comparative study with numerical investigation. Glass beads were cleaned by piranha solution and then thoroughly rinsed by deionized water and dried in the oven to represent hydrophilic particles. Polymer grafted glass beads were synthesized using the same procedure described in Chapter 2.4.2. The glass slide prepared with the same process was used to estimate the degree of hydrophobicity. Water drops formed on the cleaned glass slide and the silane-treated glass had contact angles of $\theta_{\text{hydrophilic}} \sim 30°$ and $\theta_{\text{hydrophobic}} \sim 100°$ (Figure 3.2).

Sensors and instrument system

The experimental instruments included an oscilloscope (Agilent DSO5014A), a signal generator (Agilent 33220A), a tunable active filter (Krohn-Hite 3944), showen in Figure 4.7-a (1, 2, 4). The experimental configuration is depicted in Figure 4.9. Bender elements (Figure 4.7-b) were made by a *Y*-poled parallel-type piezoelectric chip (T226-A4-303Y) from PIEZO SYSTEM, INC. The function generator sends a signal to the source bender element, which transforms the electrical signal into mechanical vibration. The shear wave excited by the source bender element travels through the sample, and reaches the receiving bender element at the other end, which then transforms the detected elastic wave into electric signal. The received signal is filtered and magnified by tunable

filter. Both the sending and receiving signals were displayed and recorded by the oscilloscope.

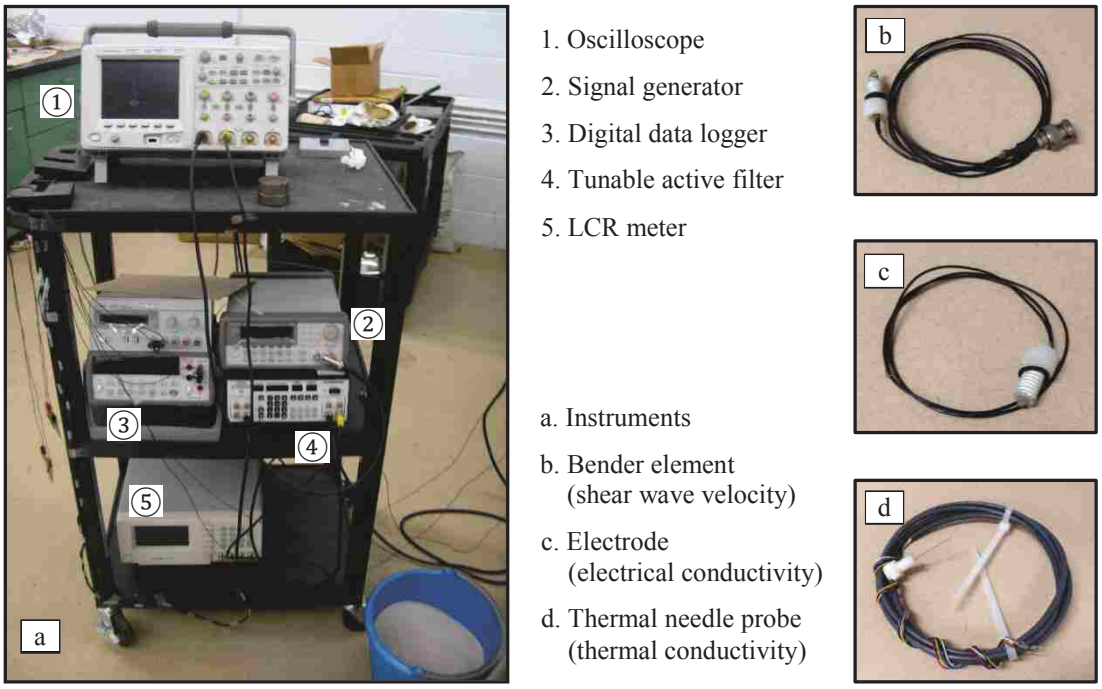

Figure 4.7 Sensors and instruments used throughout the entire research.

Sample Preparation and Measurements

The hydrophilic (cleaned) and the hydrophobic (polymer-coated) glass beads were thoroughly wetted with water prior to their placement into the test cell. The test cell was a perforated acrylic cylinder with diameter × height of Φ72 mm × H32 mm. The initial void ratio of the packed samples was $e_o = 0.68$, and saturation $S = 100$ %. A network of holes was made in the cell to facilitate uniform and fast drying. Filter paper was placed inside the cell to prevent the loss of particles through the holes. No vertical stress was applied on the specimen to be able to capture the maximized capillary effect. A

pair of bender elements was installed at the centers of top and bottom caps to measure shear waves (Figure 4.8). Step function with excitation frequency of 20 Hz and the amplitude of 3 Volt was used as input signal. The received signal went through a digital filter with one channel of high pass of 100 Hz and the other channel of low pass of 50 kHz, and 20 dB magnifications for each channel.

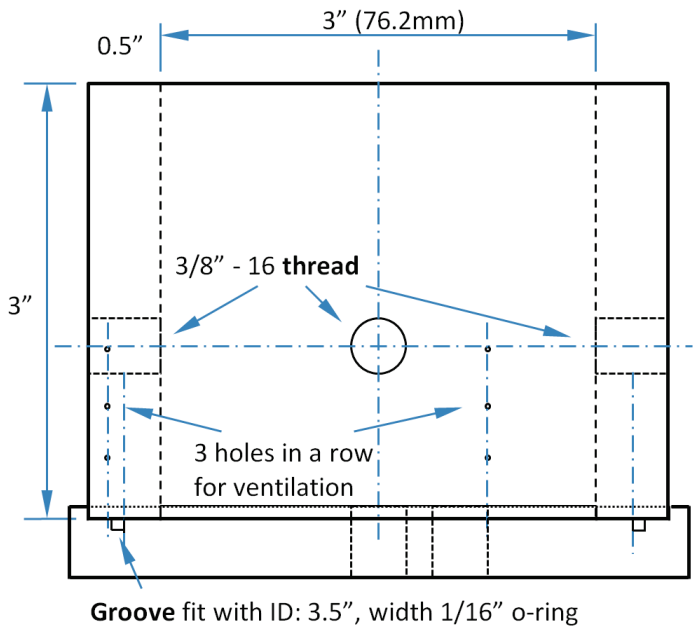

(a) Sketch of customized oedometer cell.

(b) Photo of oedometer cell (top cap and bottom plate, with threaded holes for sensor mounting.

Figure 4.8 Sketch and photo of customized oedometer cell

The cell was placed in a forced-convection chamber connected to the heat circulator (PolyScience Inc., 9102A11B). The temperature of the circulating bath fluid was set at constant temperature of 80 °C to allow for gradual evaporation of sample water by elevating the temperature of the sample up to ~40 °C. The water loss, hence state of saturation was monitored as change in sample mass by a digital balance (Denver Instrument Inc., P-8001) at the time of each shear wave measurement. The cell was placed on the digital balance outside the oven (Figure 4.9). The changes in specimen mass and the corresponding shear-wave signals were continuously monitored until no further change was observed in mass. Since evaporation at ~40 °C could not achieve complete drying (e.g., $S = 0$), the sample was then moved to an oven and completely dried at 120 °C overnight to identify the amount of residual moisture. The computed degree of saturation values were then offset by the residual moisture content. Since no capillary effect prevails under very dry conditions, it is reasonable to assume that the adjusted degrees of saturation are close to the true values for the entire evaporation process.

The electronics setup to obtain shear wave velocities is sketched in Figure 4.9. The determination of the first arrival time of received S-wave signals was based on the work conducted by Lee and Santamarina (2005), which considers the near field effect.

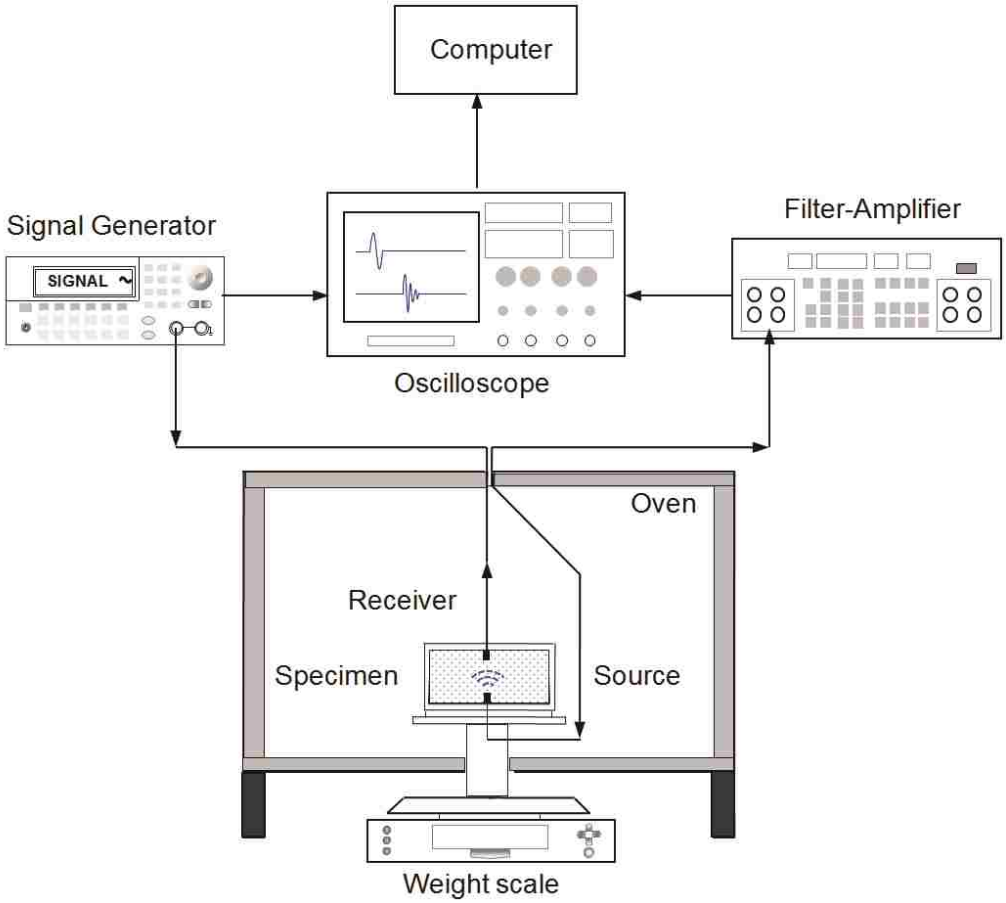

Figure 4.9 Experimental setup for shear-wave velocity measurements during evaporation.

4.3.2 Evolution of shear-wave velocity and small-stain stiffness

The evolution of measured shear-wave velocity and amplitude with saturation for hydrophilic and hydrophobic glass beads are shown in Figure 4.10 and 4.11, respectively. In Figure 4.11 the red color indicates high amplitude, and green color denotes a lower one. The hydrophilic specimen shows the constant evolution of wave traces during early stage of evaporation. The first arrival of shear wave begins slightly increasing near the

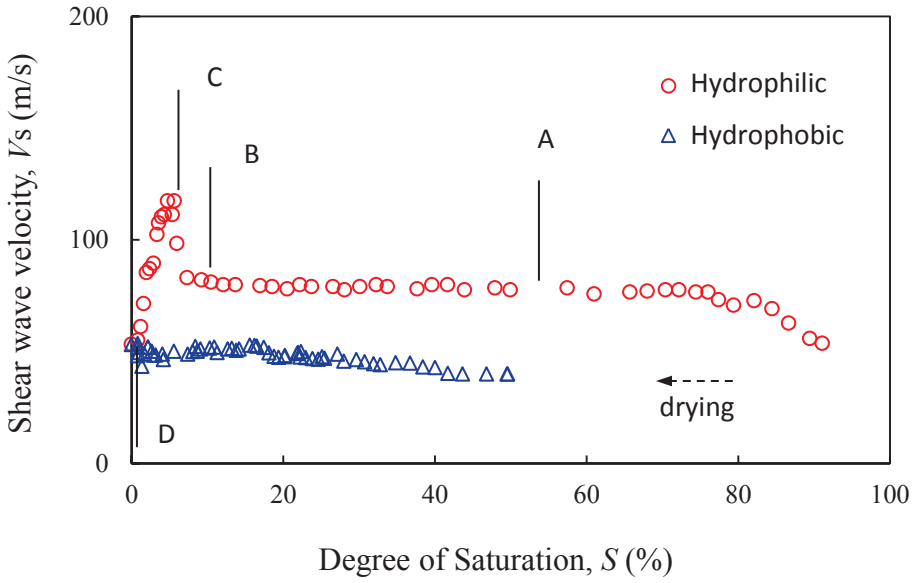

Figure 4.10 Evolution of shear-wave velocity with varying degree of saturation for hydrophilic and hydrophobic sands.

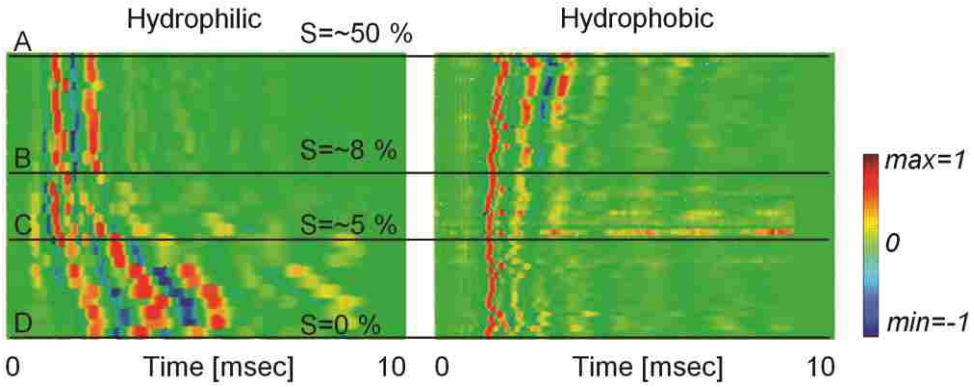

Figure 4.11 S-wave measurements: (left) hydrophilic sample, and (right) hydrophobic sample. A, B, C and D lines are the sections for degree of saturation at 50 %, 8 %, 5 %, and 0 % respectively.

degree of saturation S = 7.5 % (line B in Figure 4.11) and decreasing at S = 5.5 % (line C) towards completely drying condition (line D). On the other hand, the hydrophobic specimen produces a quite constant first arrival in shear wave as shown in Figure 4.11.

The maximum shear stiffness computed from the shear wave velocity is plotted with degree of saturation in Figure 4.12. It should be noted that the degree of saturation is based on the measured mass of entire system. Although the perforated cell allows quasi-uniform evaporation, the actual degree of saturation within the specimen may not be uniform. Thus it is noted that the degree of saturation in this study is an equivalent value.

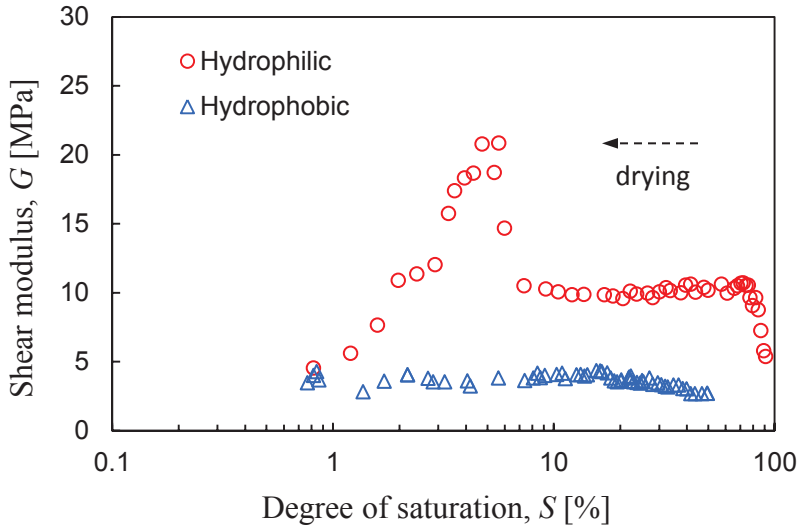

Figure 4.12 Evolution of shear-modulus calculated from shear wave velocity as the varying degree of saturation of hydrophilic sand hydrophobic samples.

Hydrophilic specimen: At the first stage (S = 100 % ~ 85 %), the stiffness slightly increased due to the increase of attractive inter-particle forces with the evaporation of water and small volume reduction and densification (Cho and Santamarina, 2001;

Frattolillo et al., 2005; Lee and Santamarina, 2005; Truong et al., 2011). The stiffness remained constant during the second stage of evaporation (S = 85 % ~ 7.5 %), as there was no remarkable change in the inter-particle contacts. At the final stage (S < 7.5 %), the stiffness noticeably increased and reached its peak value at S ~5.5 % due to the pronounced consequence of negative capillary pressure. As the capillary effect vanished with further drying, the stiffness dropped to the initial saturated value of G_{max} = 4.5 MPa. The results demonstrate that the negative capillary pressure (e.g., suction) plays an important role to improve the inter-particle contacts stresses under nominal vertical effective stress.

Hydrophobic specimen: Stiffness remained fairly constant and at a lower value than of the hydrophilic specimen throughout the evaporation process. The stiffness of hydrophobic specimen is about 18 % of that of the hydrophilic specimen at the point *C,* where the hydrophilic value reaches its maximum. Quasi-constant shear stiffness is attributed to the fact that the polymer-coated particle surfaces do not produce negative capillary pressure, neither do they attracting neighboring particles by water bridges. The same inter-particle forces come into play at S = 0 % for both types of particles at the same initial void ratio, when no water effect prevails and the shear wave velocities convergence.

4.4 CONCLUSIONS

In this chapter, a numerical study was used to simulate the liquid-bridge configuration in hydrophilic and hydrophobic particles, and analyze the induced capillary pressure and capillary forces with various degrees of water saturation.

The complementary shear-wave velocity tests confirmed that development of capillarity in hydrophilic soil can significantly increase the small strain stiffness at low degrees of saturation, whereas such a capillary "cementing" effect is not salient for hydrophobic soil due to the water-repellent property of the surface.

CHAPTER 5

CONDUCTION PHENOMENON IN SANDS OF DIFFERENT WETTABILITY

5.1 INTRODUCTION

Although there is a wealth of knowledge about behaviors of unsaturated soils, this knowledge was established under the assumption of soil as a water-wetting (hydrophilic) material. Yet, hydrophobic soils are ubiquitous either from natural events or human behavior. In unsaturated soils, surface property plays a deterministic role on wetting behaviors of the pore fluid, and in turn the soil-water interaction and the liquid-air distribution dominate the mechanical and physical properties of these systems.

Conduction behaviors of hydrophobic soil have been rarely investigated. In this chapter, experiments were designed to characterize the heat, electronic, and water conduction behavior of the hydrophilic and hydrophobic sands at varying degrees of saturation.

5.2 HEAT TRANSFER AND ELECTRICAL CONDUCTION

The accurate estimation of thermal behavior in soils has significant implications to a wide range of geotechnical and geo-environmental engineering, including geothermal foundations and energy piles (Brettmann and Amis, 2011), geological carbon

dioxide sequestration, recovery of natural gas hydrates (Cortes et al., 2009), and nuclear waste disposal (Li et al., 2012). A number of physical factors that influence the thermal response of soils have been investigated, such as void ratio, pore fluid, particle gradation, degree of saturation, and mineralogy (Abu-hamdeh and Reeder, 2000; Brandon and Mitchell, 1989; Yun and Evans, 2010; Yun and Santamarina, 2008). Among these the water content has been observed to be a dominant parameter, yet the surface wettability has been excluded.

On the other hand, in fossil-fuel-resource exploration, non-destructive testing using seismic and electromagnetic waves to estimate the amount of hydrocarbon rely on the electrical properties of soils and rocks (Mukerji et al., 2009). The electrical properties, in turn, rely on the volumetric fraction of every constituent phase in the burying layers. Nevertheless, the spatial distribution of each phase, not only the volumetric fraction, influences the thermal transfer and electrical conduction of these geo-materials significantly. As shown earlier, the spatial distribution of phases (e.g., water and air) can be affected by the pore-fluid configuration and the interplay with solid particles determined by surface wettability. Therefore, the interpretation of measured physical properties requires further investigation of evolutionary conduction behavior of unsaturated soil with the consideration of different surface wettability.

Several methods have been reported to synthesize hydrophobic sands by coating the surface with organic-silane (McHale et al., 2007). However, this stationary hydrophobicity of soils prohibits uniform pore fluid distribution at high degree of saturation, which might lead to inaccurate measurement of thermal or electrical properties (Kim et al., 2011). Therefore, a fully saturated hydrophobic sand and uniform water

phase distribution at high water content can be achieved by using the PNIPAAm polymer-grafted sands to avoid such limitations. The sample can be completely saturated at low temperature as a hydrophilic material, and then turns into hydrophobic when temperature is raised, which generates more credible physical properties at high degrees of saturation.

5.2.1 Experiment setup

Materials

The granular material tested in this study is quartz sand Ottawa 20/30 with specific gravity $G_s = 2.65$, maximum void ratio $e_{max} = 0.742$, minimum void ratio $e_{min} = 0.502$. The grain size distribution was fairly uniform, with coefficient of uniformity $C_u = 1.15$, and mean particle size $D_{50} = 0.72$ mm. The sand particles were well rounded (roundness ~0.9) so that the shape effect could be ignored. Sands cleaned with "piranha solution" (a mixture of 98% sulfuric acid and 30% hydrogen peroxide in 3:1 by volume), were used as wettable or hydrophilic material. Even though silica sand is naturally hydrophilic, acid washing results in very hydrophilic sand particles.

The hydrophobic sand was produced by grafting with thermally sensitive polymer, poly-NIPAAm or PNIPAAM, using the surface-initiated atom radical transfer polymerization (SI-ATRP) technique as described in Chapter 2. The polymer-grafted sand was hydrophilic at room temperature and hydrophobic when the temperature was higher than the lower critical solution temperature (LCST) ~32 °C. The surface modification procedure is schematically presented in Figure 2.10 (detailed process can be

found in Chapter 2.4.2). The polymer coated sands were used as hydrophobic material at elevated temperatures.

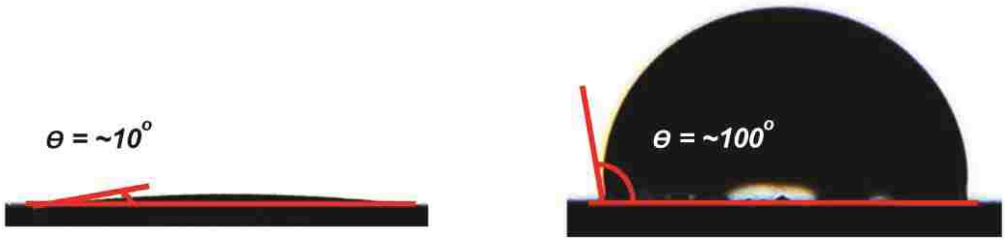

Figure 5.1 Comparison of contact angles of a hydrophilic (cleaned) and hydrophobic surface (polymer coated at temperature > LCST).

The water affinity of hydrophilic and hydrophobic sand was characterized by measuring the contact angles on the surrogate surfaces, which are glass slides simultaneously treated with the same process as the sand surfaces. Water droplets spread on the hydrophilic glass slide forming a flat water film with a contact angle $\theta_{hydrophilic}$ ~10° (hydrophilic). The polymer-grafted surface switches to hydrophobic when the slide is heated up to ~50°C, and water droplets form a contact angle of $\theta_{hydrophobic}$ ~100° (as shown in Figure 5.1). This observation verified that the presence of polymer film makes the surface hydrophilic-phobic reversible and imposes a controllable hydrophobicity.

Specimen preparation

Specimens (i.e., cleaned sands and polymer-grafted sands) were thoroughly mixed with water for 15 min before packing into the test cell. The same cylindrical acrylic cell described earlier (see Figure 4.8, inside diameter 72 mm × height 81 mm, described in

chapter 4.3.1) was used as the test cell. A single thermal-needle probe and a pair of electrodes were mounted on the top and bottom plates to measure the thermal and electrical properties. Figure 5.2 shows the entire experiment setups for the thermal and electrical properties measurements. Detailed depiction of the test cell, configuration of the sensors, and peripheral electronics are shown in Figure 5.3 and Figure 5.4, for the thermal and electrical conductivity, respectively.

The mixing water was deionized, vacuum degassed, and heated up to ~40 °C to equilibrate the sample temperature with the test chamber conditions, hence minimize varying temperature effect. A very small vertical pressure of 0.99 kPa was applied to manifest the capillary effect before testing began.

(a)

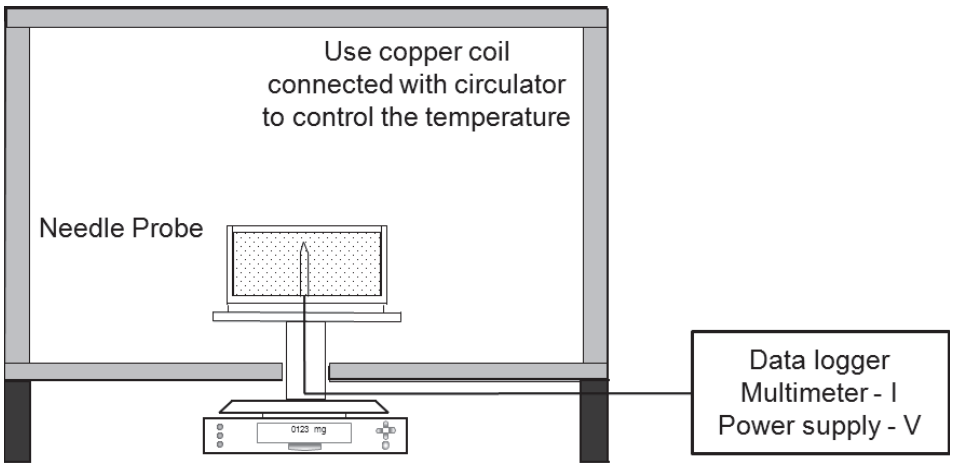

(b)

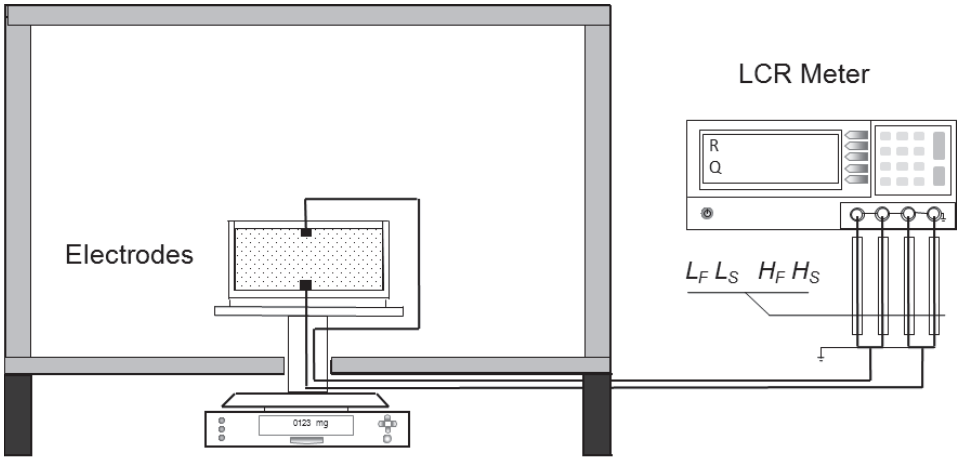

Figure 5.2 experimental setups for (a) transient line-source heating system for thermal conductance measurements; (b) two terminal electrode system for electrical resistance measurements of soil with different surface wettability as the degree of saturation varies.

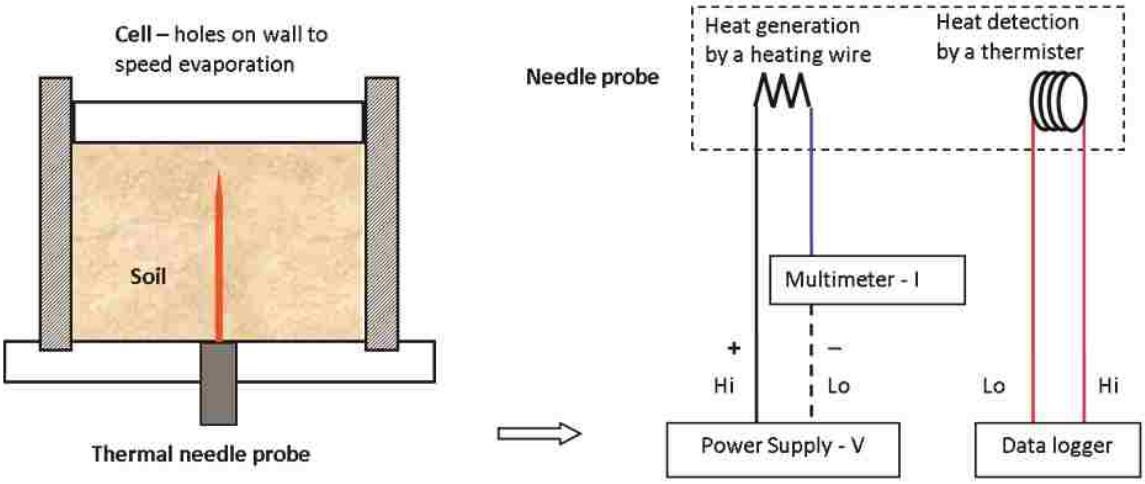

Figure 5.3 Testing cell and thermal needle probe formation.

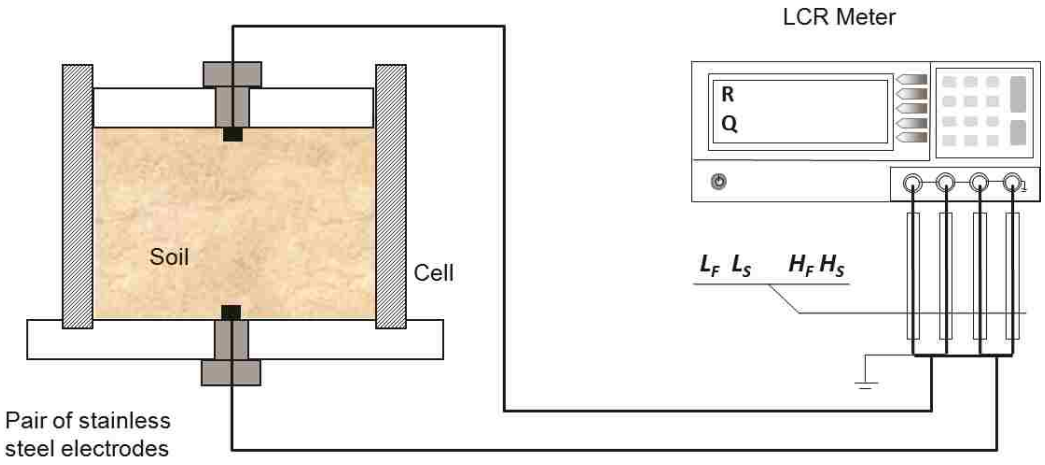

Figure 5.4 Testing cell, sensors configuration, and LCR meter connection of the two terminal system.

Experimental procedure

The cell was placed in a forced-convection chamber consisting of a storage container and a coiled copper tube connected with circulator for heating (PolyScience Inc., 9102A11B). The circulating bath-fluid temperature was set at 80 °C, which allowed gradual evaporation of water with temperature of the sample in the cell up to 40 °C. The cell sat on a digital balance located outside the chamber. The changing mass of specimens were continuously monitored and stored in computer until no changing in the weight of the specimen. After the evaporating process, the sands were removed and completely dried in oven to determine the residual moisture content of the specimens. During the evaporation process, the thermal/electrical conductivity was measured and recorded at a certain time intervals (e.g., 30 min).

The thermal property measurements were made using the line-source transient heat method. A thermal needle probe, consisting of a heating wire and a thermistor incorporated into a 3 cm long, 1 mm diameter, stainless steel needle, was mounted at the center of the bottom plate of the cell (see Figure 4.7-d and Figure 5.3). Heat was generated by running a DC current through the heating wire, and the temperature evolution within the sample was monitored by the thermistor. The test specimens were assumed to be homogeneous, isotropic and with little heat loss.

The thermal conductivity can be obtained by the following equation:

$$k = \frac{Q}{4\pi}\frac{\ln\left(t_2/t_1\right)}{\left(T_2 - T_1\right)} = \frac{I^2 R_m}{4\pi}\frac{\ln\left(t_2/t_1\right)}{\left(T_2 - T_1\right)} \qquad \text{Eq. 5-1}$$

where k is the calculated thermal conductivity; Q is the heat flow of one measurement; I and R_m are the measured current and resistance of the heating wire. By monitoring the

temperature change from T_1 to T_2, during the time period t_1 to t_2, a linear relationship between temperature and time (in log scale) can be defined, as shown in Figure 5.5, where an appropriate window was selected, e.g. 30 sec after measuring started, to avoid the initial non-linearity caused by boundary effect. The slope of the linear part of the curve can be converted into thermal conductivity using Eq. 5-1.

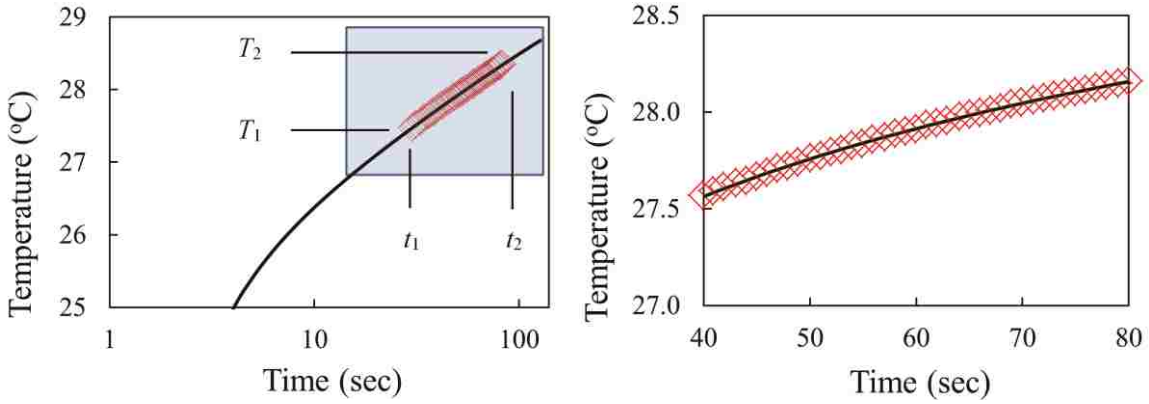

Figure 5.5 Typical temperature change profile of the heating process in one thermal conductivity measurement.

A two-terminal electrode system, as shown in Figure 4.7-c and Figure 5.4 was used to measure the electrical resistance at low frequency (<100 kHz). The insulating plastic cell houses a pair of 3 mm diameter electrodes made of stainless steel located on the top cap and the bottom plate. Each electrode was connected to two co-axial cables and fed into the impedance analyzer (GW Instek, LCD-819). The excitation alternating current voltage was set at 1 V.

5.2.2 Results and discussion

Evolution of Thermal Conductivity

The thermal conductivity k of granular materials depends on the mineral that makes the solid grains, the fluid that fills the pore space, and the inter-granular contact conditions.

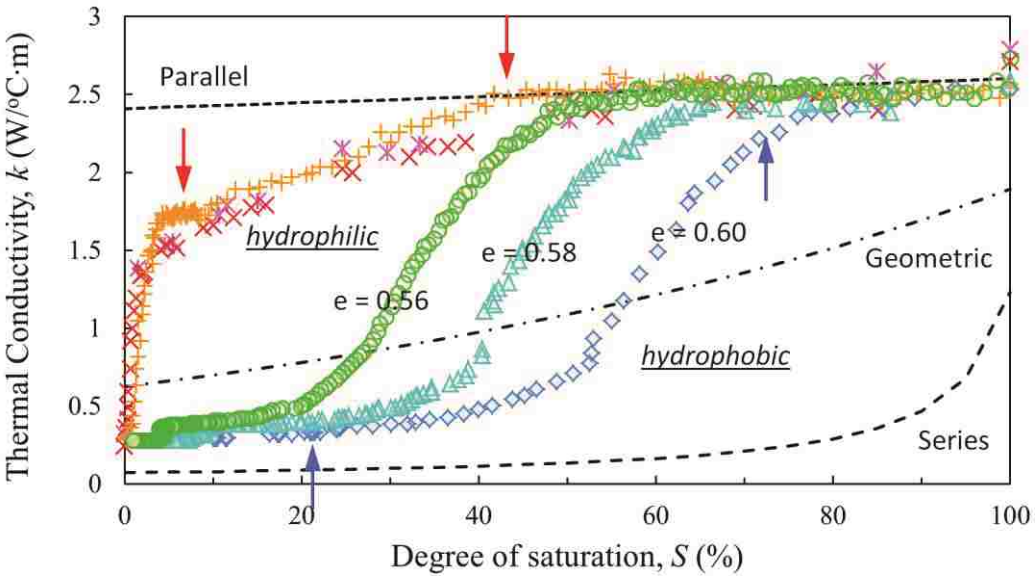

Figure 5.6 Thermal conductivity changes with degree of saturation for both hydrophilic and hydrophobic sands (e: void ratio = V_{void}/V_{solid}).

Figure 5.6 presents the evolution of thermal conductivity with degree of saturation for the two types of sand with different surface wettabilities. The dry sand thermal conductivity was measured as ~0.25(±0.05) W/mK, and the fully wetted sand (e.g. S = 100%) as ~2.5(±0.10) W/mK, for both the hydrophilic or hydrophobic samples. Note that, for hydrophobic samples at a high degree of saturation, it is hard to evenly mix the

sand with water due to the inherent water repellency. Therefore, polymer coated sand was utilized to be fully wetted at low temperature first, and then temperature was increased turning the sand into hydrophobic afterwards. All samples were dried from 100 % degree of saturation to fully dried state (S = 0 %).

For hydrophilic sand specimens, the thermal conductivity did not deteriorate with drying until S was reduced to ~50 % degree of saturation. The thermal conductivity started decaying as the sample dried and lost ~40 % of thermal transfer capability from 50 % to ~5 % of saturation. As the sample dried completely, the thermal conductivity decreased steeply to its minimum value at full dryness.

On the other hand, the hydrophobic samples showed a different pattern of thermal conductivity variation with saturation. All of the hydrophobic samples had fairly constant thermal conductivity values at high degrees of saturation (S above ~80 %). As the water evaporated, the hydrophobic sands displayed S-shape decrease path for thermal conductivity, which appeared to be sensitive to the relative density or void ratio of the sample. The thermal conductivities of all the hydrophobic samples decayed smoothly and converged to a minimum value at ~20 % saturation, which is much earlier in the drying process than hydrophilic sand. In the region from 80 % to 20 %, the denser samples (lower e) lost thermal conductivity later than the looser sands at S = ~50 % relative to 65 % and 80 %. In this region, dense samples were approaching stable at S ~20 %, later than loose samples at 30 % and 40 %. Except at very high degree of saturation (> ~80 %), the hydrophobic sand specimens always had a lower thermal conductivity than the hydrophilic ones.

It is known that the thermal conductivity of each soil component varies over two orders of magnitude (e.g., $k_{mineral} > 3$ W/mK, $k_{water} = 0.56$ W/mK (at 0 °C), $k_{air} = 0.026$ W/mK) (Yun and Santamarina, 2008). However, the thermal conductivity is almost one order of magnitude lower in dry soils that are made of the same minerals than the value of the solid minerals comprised of soil particles, in most cases ($k_{dry\_soil} < 0.5$ W/mK). Figure 5.7-a shows particle-level heat transfer mechanisms in soils. This suggests that the main heat-transfer path in particulate materials is through the pore fluid conduction, particle conduction, and contact conduction. Macro-scale tests show that heat

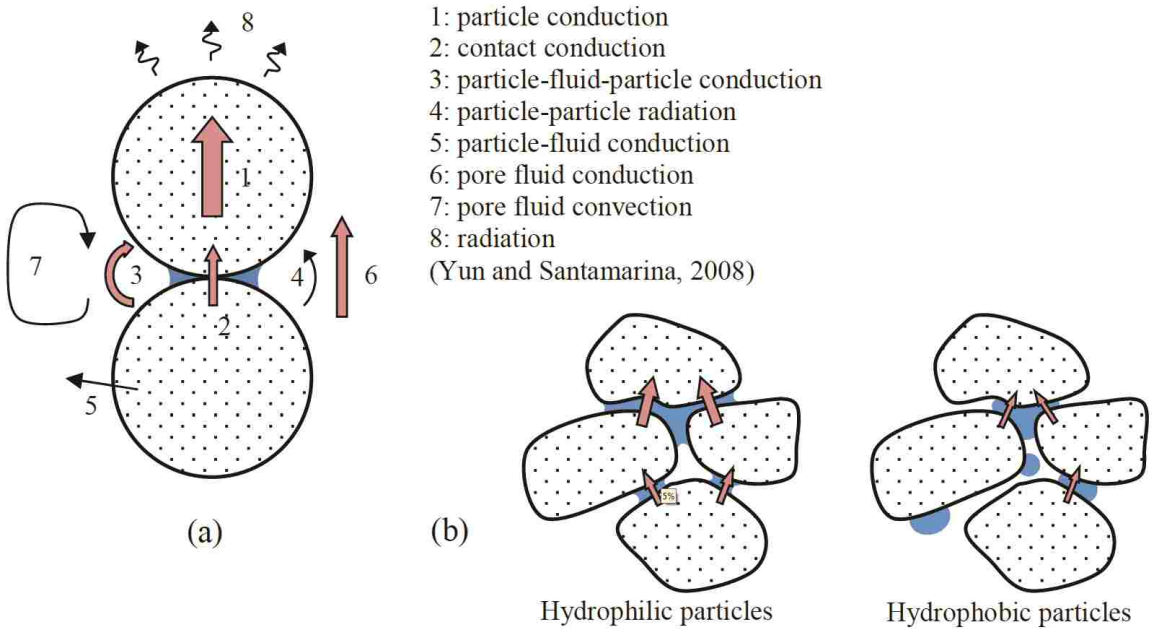

Figure 5.7 Typical heat transfer paths in particle-fluid system (a), and comparison of heat transfer in hydrophilic sands and hydrophobic sand at low degree of saturation (b).

flux through pore-fluid at contacts plays a preponderant role on the effective thermal conductivity of soils at low water saturation. In other words, the pore fluid contributes a major portion of the heat-transferring capability, and the thermal conductance decreases substantially only at a very low degree of saturation where very little liquid bridging at the inter-particle contact can transfer the heat. This explains the ordered sequence of typical thermal conductivity values: $k_{air} < k_{dry\_soil} < k_{water} < k_{saturated\_soil} < k_{mineral}$.

Figure 5.7-b compares the effect of pore water distribution for hydrophilic and hydrophobic soils. The pore water distribution in hydrophobic particles has much smaller area for particle-fluid-particle conduction at particle contacts compared to hydrophilic particles at the same level of saturation. This also explains that the thermal conductivity of hydrophilic soils decreases dramatically only at very dry state and the value of hydrophobic soils is much lower than hydrophilic soils and decreases gradually as the soils dry.

The predicted thermal conductivity by mixture models is superimposed in Figure 5.6, to delineate upper and lower bounds for the data (DeVera and Strieder, 1977). The parallel mixture model, analogous to the effective elastic modulus, can be calculated as follows:

Parallel: $k_{soil} = (1-n)\cdot k_{mineral} + n\cdot S\cdot k_{fluid} + n\cdot(1-S)\cdot k_{air}$ Eq. 5-2

The series model and the geometric mean model are described in Eq. 5-3, and Eq. 5-4, respectively.

Series: $k_{soil} = \sum\left(\frac{\phi_{mineral}}{k_{mineral}} + \frac{\phi_{fluid}}{k_{fluid}} + \frac{\phi_{air}}{k_{air}}\right)^{-1}$ Eq. 5-3

Geometric mean: $k_{soil} = k_{mineral}^{\phi_{mineral}} \cdot k_{fluid}^{\phi_{fluid}} \cdot k_{air}^{\phi_{air}}$ Eq. 5-4

where Φ_i is the volumetric fraction of each component i, which includes $\Phi_{mineral} = (1-n)$, $\Phi_{fluid} = n \cdot S$, $\Phi_{air} = n \cdot (1-S)$, and S is the degree of saturation, n is the porosity. The existing empirical and semi-empirical models to estimate thermal properties usually include macro-scale parameters, such as unit weight, porosity, degree of saturation, without considering surface wettability effect. Hence, the implementation of models using known soil property parameters may be somewhat misleading. The experimental results presented here reveal that surface wettability has a significant influence on thermal conductivity for unsaturated soil.

Evolution of Electrical Conductivity

The electrical conductivity, which is the reciprocal of electrical resistivity, is a measure of the ability of a medium to conduct an electric current. In soils this property is governed by the volumetric fraction of water and the ionic concentration of the pore fluid. Therefore, the material is expected to have higher conductance with increasing degree of saturation. However, unlike thermal conduction, electrical conductance must have the long-range connectivity of the pore fluid to carry the electrons from one side to the other following the percolation path.

Figure 5.8 shows the electrical conductance of both hydrophilic and hydrophobic sands with varying degree of saturation. For hydrophilic sands, the electrical conductivity stays constant at high water content from 100 % to ~50 % of degree of saturation. As the sample dries, the electrical conductance starts declining linearly with saturation to its minimum value at fully dried condition.

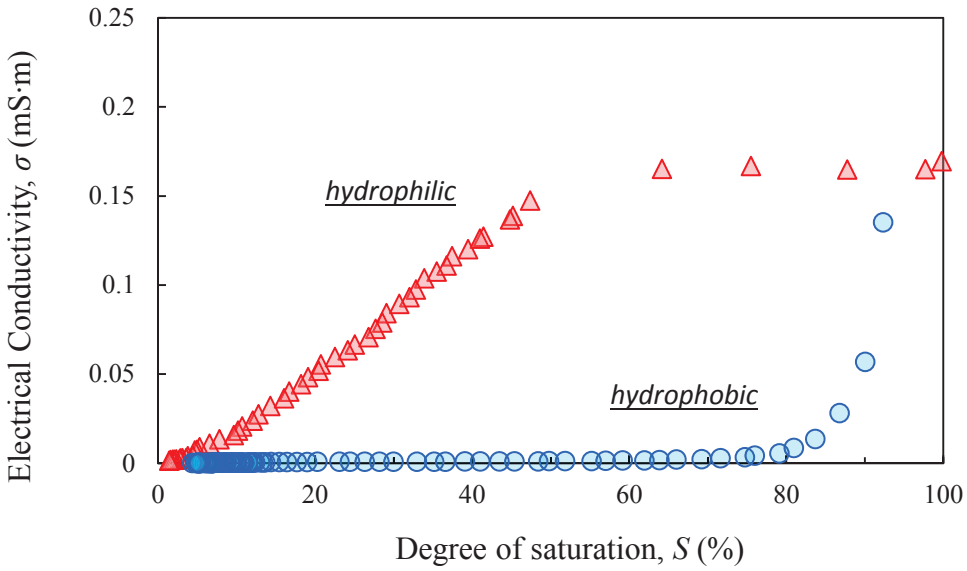

Figure 5.8 Electrical conductivity evolutions as degree of saturation of sample for both hydrophilic and hydrophobic sand.

In contrast, hydrophobic sample did not evolve the electrical conductivity until the degree of saturation increased to above ~80 %, where a sharp rise took place beyond. Eventually, the electrical conductivity of hydrophobic sands reaches the maximum number and converge to the value same as hydrophilic ones. The unsaturated hydrophilic sand displayed had higher electrical conductivity than the hydrophobic ones for all degrees of saturation. When sands are fully dry or fully saturated, the electrical property does not differ between the two types of sands of opposite water affinity, suggesting that the surface wettability doesn't affect this property in these conditions. Under unsaturated conditions, hydrophilic sand does not lose any conducting capability down to ~50 % saturation, while the hydrophobic sand, on the other hand, display little or no conductivity even when the sand is at ~80 % saturation.

The hydrophobic sand has low affinity to water, so that water tends to segregate instead of wetting the particle surface. The long-range connectivity of water phase in hydrophobic soils is poor, as was also determined through microscopic observations presented in Chapter 3 (see Figure 3.6). Hence, the surface wettability plays a crucial role of electrical properties of unsaturated soils.

5.3 HYDRAULIC CONDUCTION

5.3.1 Experiment setup

Three types of tests were conducted to characterize the different hydrological behavior of hydrophilic and hydrophobic soils. (1) Water infiltration: Water invades the dry-soil body; (2) saturated flow: water conduction at 100 % degree of saturation, no air pockets present in the sample; (3) gravity drainage: water drains out of the sample from full saturation under gravity.

To avoid temperature-induced viscosity changes, organo-silane treated hydrophobic sand was used instead of the hydrophobic polymer-coated sands at elevated temperature. The contact angles of water on these two surfaces were similar. Sand particles were filled in a jacketed Chromaflex® column (I.D 2.5 cm, length 30 cm, volume 147 mL, from Kimble Chase). The inside wall of the glass column was treated with organo-silane to be hydrophobic (Jesionowski, 2009) to restrict boundary flow. For water infiltration and saturated conduction tests, three different constant head pressures (16.6 cm, 46.6 cm, and 79.9 cm of water) were applied to measure the hydraulic diffusion and conduction. A water reservoir was seated on a strut with height adjustable brackets,

connecting to a water supply. The column was put on the digital balance so that the mass of water invading the column could be recorded every 2 seconds in water infiltration tests. The test setup is shown in Figure 5.9-a.

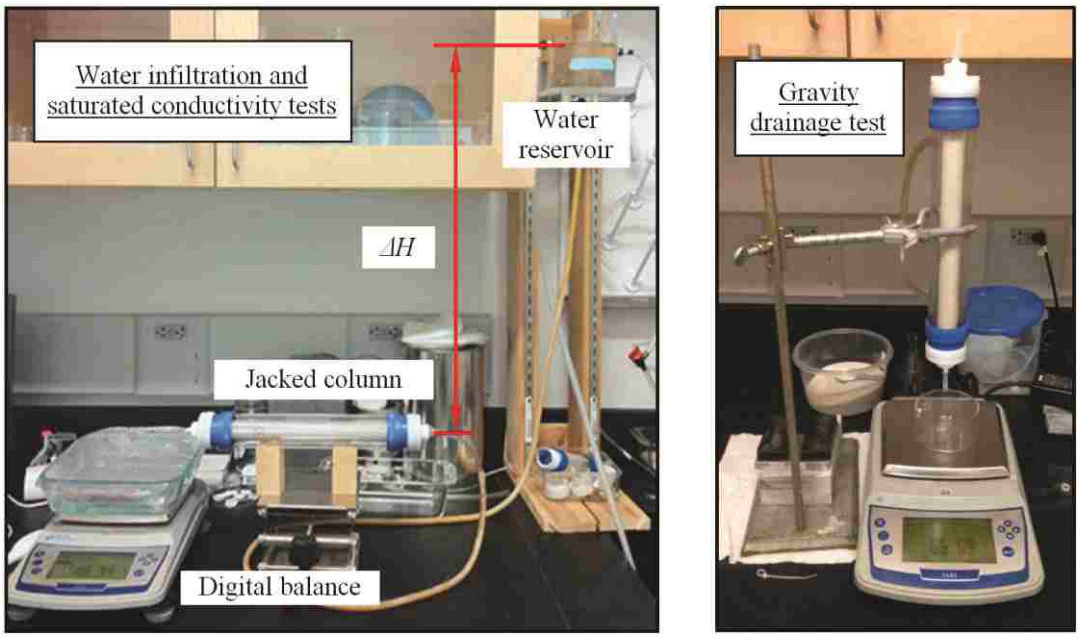

Figure 5.9 Experiment setup of hydraulic conduction test for hydrophilic and hydrophobic sands.

In the saturated-flow test, the configuration was the same except the digital balance was used to monitor the mass of the water flowing out of the column. In that case, the increase in the mass of water per time was converted into volumetric flow rate. Since the degree of saturation greatly affects the value of hydraulic conductivity, it was important to make the sample fully saturated to avoid the influence of the degree of saturation. Vacuum was applied to the column to remove the residual air and to facilitate

full saturation. Degassed deionized-water was used in the system to avoid extra air bubbles entering the vacuum-saturated sample.

The gravity-drainage tests were run right after the saturated-flow tests. The column with a fully saturated sample was vertically fixed by clamp without any water inflow, and the pore water was allowed to drain out of the column by gravity. The drained water was collected and weighed on the balance. The experimental setup is shown in Figure 5.9-b.

Three sizes of hydrophilic and hydrophobic quartz sands were used in these three series of experiments. Their physical properties are summarized in Table 5.1.

Table 5.1 Tested sand properties.

Soil	Mineralogy	Void ratio	D_{50} (mm)	C_u	G_s	Roundness
Ottawa F110 sand	quartz	0.56	0.12	1.62	2.65	0.7
Ottawa 50/70 sand	quartz	0.56	0.31	1.43	2.65	0.5
Ottawa 20/30 sand	quartz	0.56	0.72	1.15	2.65	0.9

Data source: (Lee et al., 2007; Yun, 2005)

According to the simple capillary tube model (Lu and Likos, 2004), a rough estimation of capillary pressure or matrix suction can be obtained by using Young-Laplace equation: $P_c = (P_a - P_w) = 2\gamma_{aw}/r$ (assuming the surface is perfect wetting, contact angle $\theta = 0°$), where P_c is the capillary pressure, term $(P_a - P_w)$ is matric suction which is the pressure difference between air and water phase, γ_{aw} is the surface energy of air-water interface, and r is the radius of the capillary tube. The granular sand can be simplified as

idealized soil comprised of uniform spherical particles. The upper and lower bound of capillary rise may then be calculated by considering simple cubic (SC, i.e., loosest possible) packing and face-centered cubic (FCC, i.e., densest possible) packing as the two limiting cases, shown in Figure 5.10-a. Using D_{50} of the sand as the equivalent diameter of the particle allows calculation of the pore sizes in idealized soil model, and an estimation of the region where capillary pressures of the three types of real sands could possibly fall. A comparison of the applied hydraulic pressure heads (16.6 cm, 46.6 cm, and 79.9 cm) and the corresponding capillary pressures that can be developed in different size sands are plotted in Figure 5.10-b. Three water heads are approximately at the same level with the capillary rises that the three different sands could build. Hence, the capillary effect on the flow behaviors (infiltration, saturated flow, drainage) is well manifested.

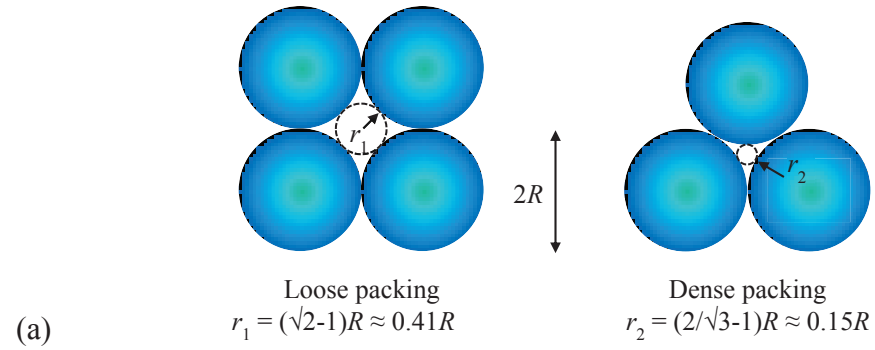

(a)

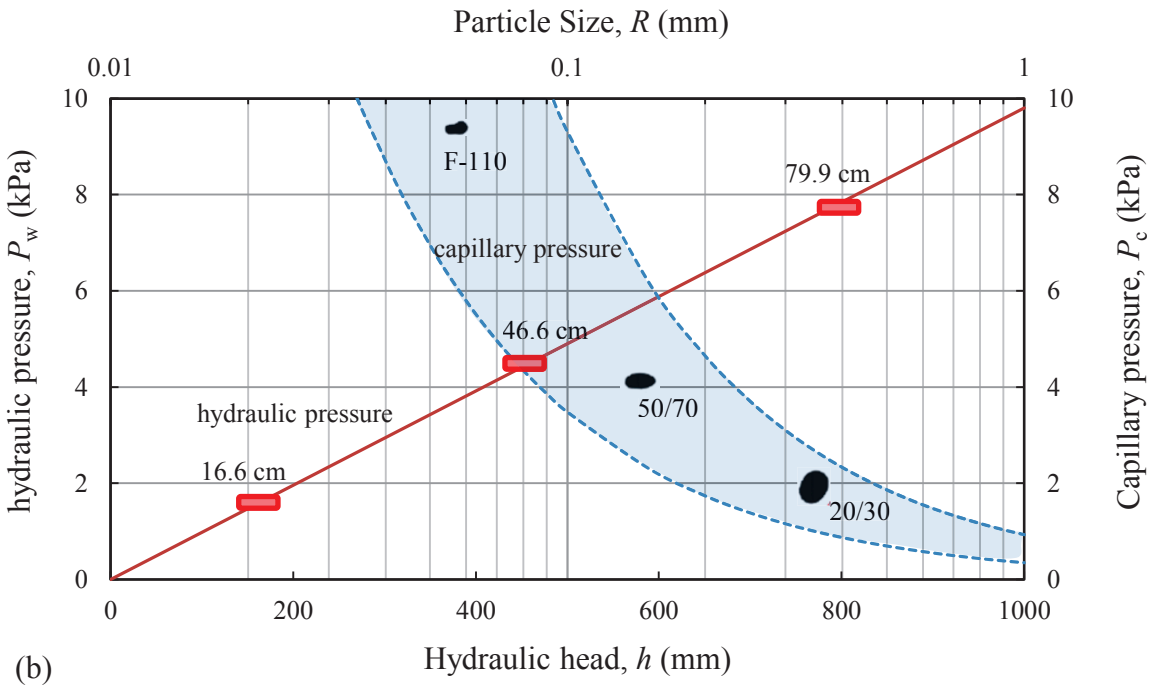

(b)

Figure 5.10 (a) relationship between pore size and particle diameter in loose (left, simple cubic packing) and dense (right, face-centered cubic packing) system; and (b) Comparison of hydraulic presure applied on the system (red blocks) and capillary pressure (light blue region) which soil samples, of different sizes (black particles), could develop.

5.3.2 Results and discussion

Water infiltration

First, let's take a look at a single tube element in a pore-network model. Figure 5.11 illustrates the pressures applied in a micro-tube with air-water interface. The capillary pressure P_c is dependent upon the size of the tube R, free energy of the air-water

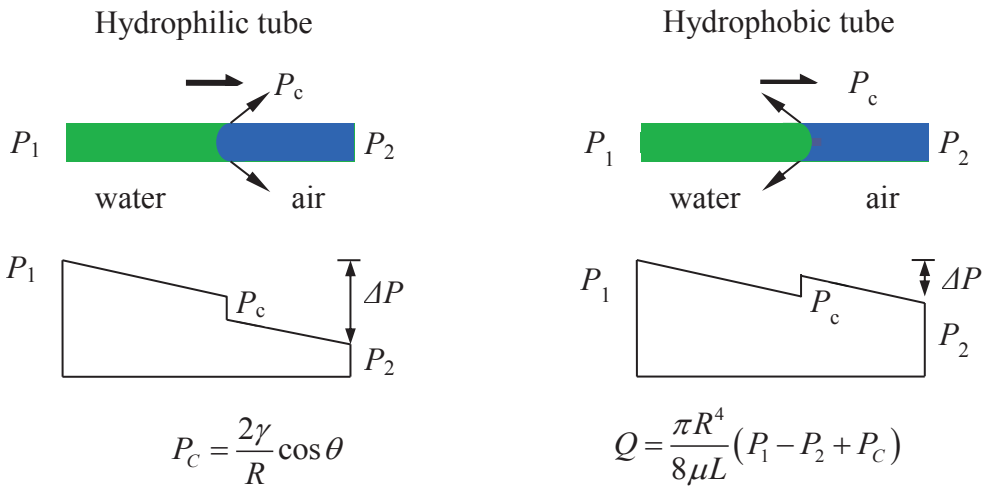

Figure 5.11 Schematic plot of Poiseuille flow and pressure distribution.

interface γ, and contact angle θ. The flow rate is determined by the pressure difference between two ends ΔP, and the geometry of the tube R and L, and fluid viscosity μ. Assuming water is invading air (i.e., $P_1 > P_2$), the capillary pressure increases the pressure difference (Figure 5.11 left), when the tube is hydrophilic. On the other hand, if the tube is hydrophobic, the invading water needs to overcome the capillary pressure against the flow direction (Figure 5.11 right). This is equivalent to the pressure difference that is partially counterbalanced by capillary pressure due to the hydrophobic tube surface. By

comparing this simple tube model, it is obvious that the surface wettability could greatly affect the pore-fluid flow in the porous media.

Figure 5.12-a shows the response of sands with different wettabilities to water invasion under different hydraulic pressure heads. Three charts plot the volumetric inflow into the column versus time for Ottawa F110, 50/70, 20/30 sands, respectively. Red solid lines represent hydrophilic sand, while blue dashed lines are for hydrophobic. Numbers 1, 2, and 3 symbolize three different applied heads 79.9 cm, 46.6 cm, and 16.6 cm correspondingly.

It is clear that for the same type of sand, as the applied hydraulic pressure increases, the water invades faster. At the same hydraulic head level, coarse sands have higher flow rates than fine sands, due to the larger pore sizes. Comparing samples with different wettability, hydrophilic sands are easier to be invaded by water (higher slope of the red curves) than hydrophobic ones (blue) at the same water pressure.

For hydrophilic sands, the surface is “water-loving”, thus the samples attract water easily so that when the water front breaks through the column, samples are almost saturated and reach the full water-retention capacities (see Ottawa 50/70 and 20/30 in Figure 5.12-a). For hydrophilic Ottawa F110 sand, the samples are less saturated as the water pressure is lowered, due to the imperfection of air extrusion from small particle size packs.

On the other hand, the hydrophobic sands are “water-fearing”. From the analysis in Chapter 4, it can be concluded that hydrophobic surfaces develop the opposite capillary force compared to hydrophilic sands in which pore water is present as liquid bridges at low degrees of saturation. The negative capillary force (see results in Figure

4.5-a) repels water and prevents the liquid from invading the sample body. If the applied water pressure is high enough to overcome the negative capillary pressure, then the fluid can still obtrude into the dry sand but with lower infiltration rate than hydrophilic counterpart under same conditions (portrayed in Figure 5.12-a, curve 1 in Ottawa F110, curves 1 and 2 in 50/70, curves 1, 2 and 3 in 20/30). The negative capillary pressure acts counter to the hydraulic pressure direction. Hence the response is equivalent to hydrophilic sample bearing lower hydraulic pressure.

However, if the applied water pressure is not large enough to overcome the negative capillary pressure, the fluid flow is halted at the location where the driving pressure is exhausted and balanced with the negative capillary pressure. As limned in Figure 5.12-a, at hydraulic head level 3 for hydrophobic 20/30 and 50/70 sands, the water infiltration flow stopped in the middle of the column by the resistance of water repellency. At hydraulic head level 2 and 3, the water pressure could not thrust the water even to enter the dry F110 sample (similar behaviors on curve 2 for 50/70 sands).

Notice that, also shown in Figure 5.10, the hydraulic pressures applied in the system fall into the range of capillary pressures developed by sands of different sizes. For instance, Ottawa F110 can develop a capillary pressure slightly higher than the hydraulic pressure that at 79.9 cm-head, while the capillary pressures developed in Ottawa 20/30 and 50/70 sands are on the same level of static water pressures at heads of 16.6 cm and 46.6 cm, respectively. This explains that for hydrophobic 50/70 sand under a 16.6 cm head, the water flow does not break through the sample (blue curve 3 in Figure 5.12-a, Ottawa 50/70). For hydrophobic F110 sand, under 16.6 cm and 46.6 cm water pressure,

the flow did not even intrude the sample (lines do not show up in Figure 5.12-a, Ottawa F110).

Meanwhile, in the cases that when the water flow did break through the column samples, the hydrophobic sands hold less amount of water than hydrophilic samples, which may mean that air is trapped inside the samples and fingered flow occurred internally, due to localized lack of wetting.

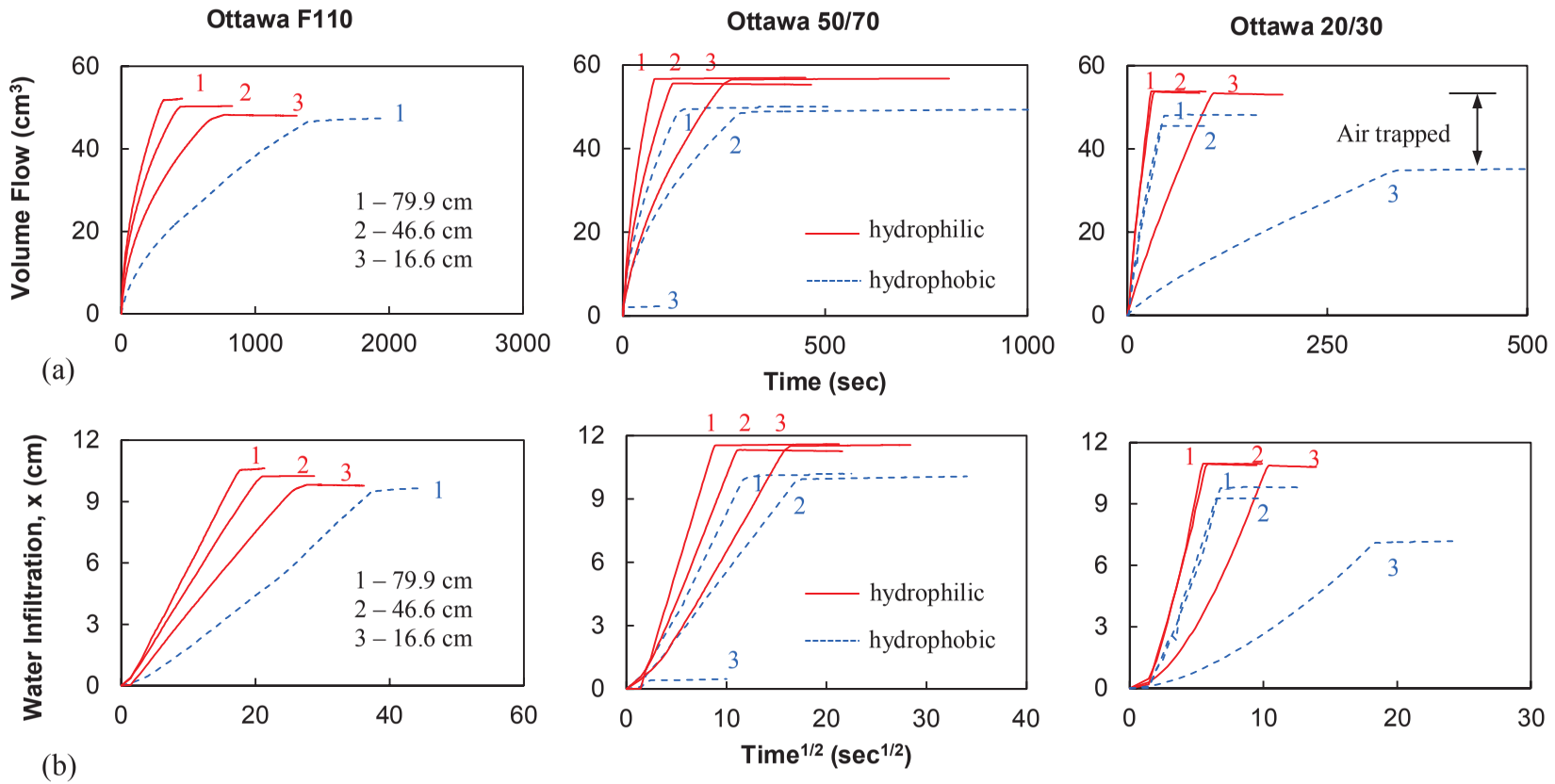

Figure 5.12 Water infiltration behaviors of dry-sand columns at different hydraulic heads for both hydrophilic and hydrophobic sands with three sizes of sand: (a) plots of volumetric flow versus time for Ottawa F110 (fine), 50/70 (medium), and 20/30 (coarse) sands; (b) replot the flow in terms of infiltration.

Diffusivity

In the case of transient horizontal water infiltration, the invasion of water as a "sharp wetting front" initially propagates at a relative fast rate through the column and gradually slows with time. Two assumptions were used to simplify the flow problem amenable for analytical solution using Darcy's law: (1) the soil beyond the wetting front (in the dry portion of the column) is fully dry, and (2) the water content and corresponding hydraulic conductivity of soil behind the wetting front (in the wet portion of the column) are constant in both space and time. Therefore the infiltration rate can be written as:

$$q = \frac{dQ}{dt} = \frac{(\theta_0 - \theta_t)\,dx}{dt} = -k_0 \frac{h_i - h_0}{x} \qquad \text{Eq. 5-5}$$

where h_i is the hydraulic head at the wetting front; h_0 is the water head behind the wetting front, and k_0 is the hydraulic conductivity behind the wetting front, which is here assumed to be equal to the saturated hydraulic conductivity.

Integrating with respect to the space and time variables x and t and imposing the initial condition of $x = 0$ at $t = 0$ yields:

$$\frac{x}{\sqrt{t}} = \sqrt{2k_0 \frac{h_0 - h_i}{\theta_0 - \theta_i}} = \lambda = \text{const.} \qquad \text{Eq. 5-6}$$

Therefore the infiltration rate q at the boundary and the total infiltration displacement Q may be predicted according to the equations:

$$q = k_0 \frac{h_0 - h_i}{\sqrt{Dt}} \qquad \text{Eq. 5-7}$$

$$\text{Q}=(\theta_0 - \theta_i)\sqrt{Dt} = s\sqrt{t} \qquad \text{Eq. 5-8}$$

where parameter s is called sorptivity [m/√t], and D is the hydraulic diffusivity [m^2/t].

In Figure 5.12-b, water infiltration is re-plotted in terms of displacement versus the square of time (second). The volumetric flow curves transform into linear displacement lines. The slope of the straight line represents sorptivity (s), and s^2 leads to diffusivity D. It is evident that hydrophilic sand has higher diffusivity than hydrophobic sand.

Saturated flow

Figure 5.14 shows the results of saturated flow of different size samples with hydrophilic and hydrophobic surface wettability. For each type of sand, three hydraulic heads were applied to get an averaged hydraulic conductivity, as plotted in Figure 5.15. It was concluded that hydrophobic sands tend to possess higher conduction ability. As the flow velocity increases with the particle size getting large, the fluid flows faster through hydrophobic than hydrophilic material.

Researchers have explored the hydrophobic surface for micro-fluid enhancement and verified that one reason why hydrophobic surface could enhance surface flow would be that the hydrophobicity turns the boundary flow from non-slip mode to slip mode (Barrat and Bocquet, 1999; Jia Ou and Blair Perot and Jonathan, 2004; Ou et al., 2004; Voronov et al., 2007; Watanabe et al., 1999). This means that at the point where liquid and surface contacts, the fluid has velocity along the flow direction, as shown in Figure 5.13. The large slip length b indicates large flow velocity at the solid-liquid interface; hence more slip boundary effect and more flow rate. This non-zero boundary flow could significantly reduce the fluid drag, in the same way that swim coats mimic hydrophobic shark skin reduce fluid friction (Dean and Bhushan, 2010).

This saturated-flow test verified the validity of slip-boundary flow in hydrophobic porous media, by showing that the hydrophobic sand has a higher hydraulic conductivity in saturated flow than hydrophilic sand.

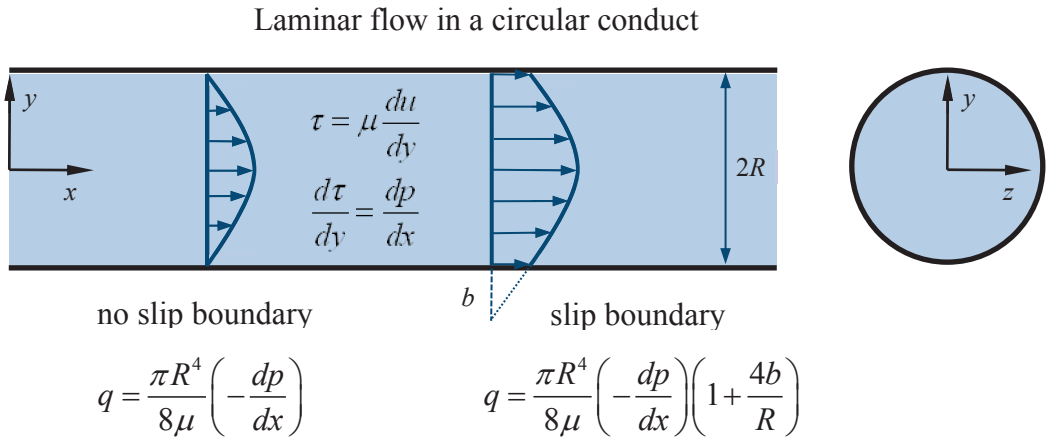

Figure 5.13 Non-slip boundary and slip boundary flow (laminar) in circular conduct.

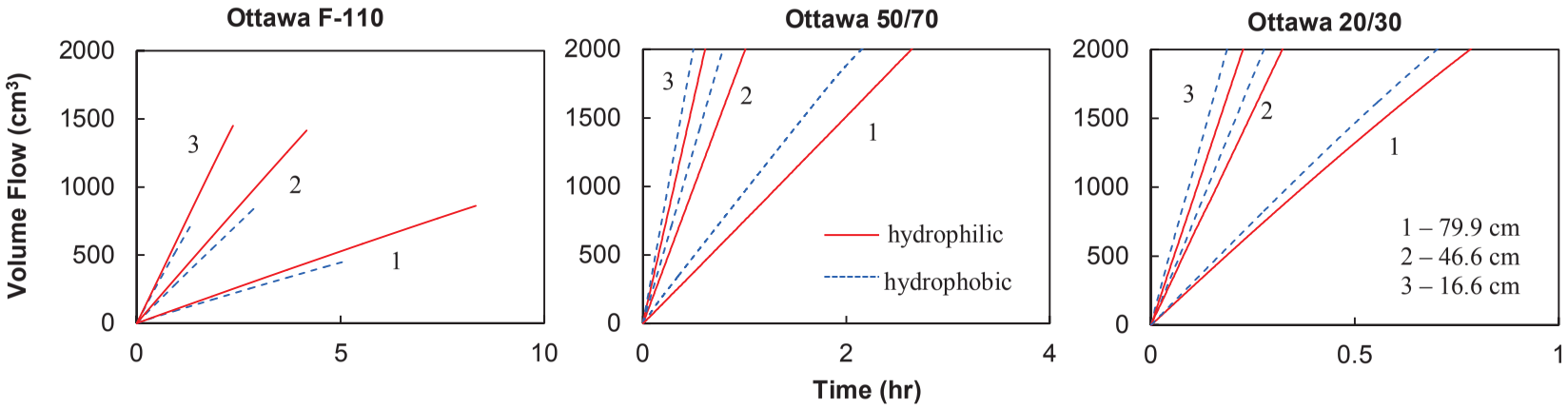

Figure 5.14 Volumetric flow of water in fully saturated hydrophilic and hydrophobic sands at three hydraulic heads.

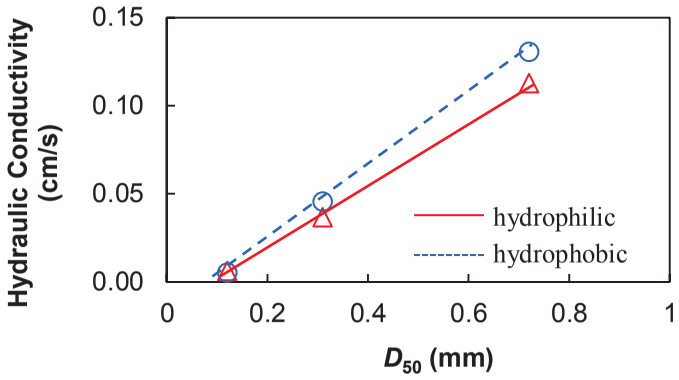

Figure 5.15 hydraulic conductivity comparison of hydrophlic and hydrophobic sands with different particle size.

Gravity drainage

The results of water mass measurements for hydrophilic and hydrophobic sands are converted into water volume and shown in Figure 5.16. The curves correspond to the quantity of drained water as a function of time for the two wetting states for Ottawa 20/30, 50/70, and F110 sand separately. For the coarse sand (20/30), there is not a substantial difference between the behaviors of hydrophilic and hydrophobic sands. Nevertheless, for sands with smaller particle sizes (50/70 and F110), hydrophilic samples can hold a larger amount of water by their internal capillarity. On the contrary, hydrophobic samples release more than 50 % (F110) or even higher percentage (80 % for 50/70) of the pore fluid. Moreover, the visual observation after the drainage shows that, for hydrophilic porous media the hydraulic continuity of the liquid phase allows for a flow in water film, whereas, bulk water displacement hence greater water recover rate is observed for hydrophobic sands due to the water repellency of the surface.

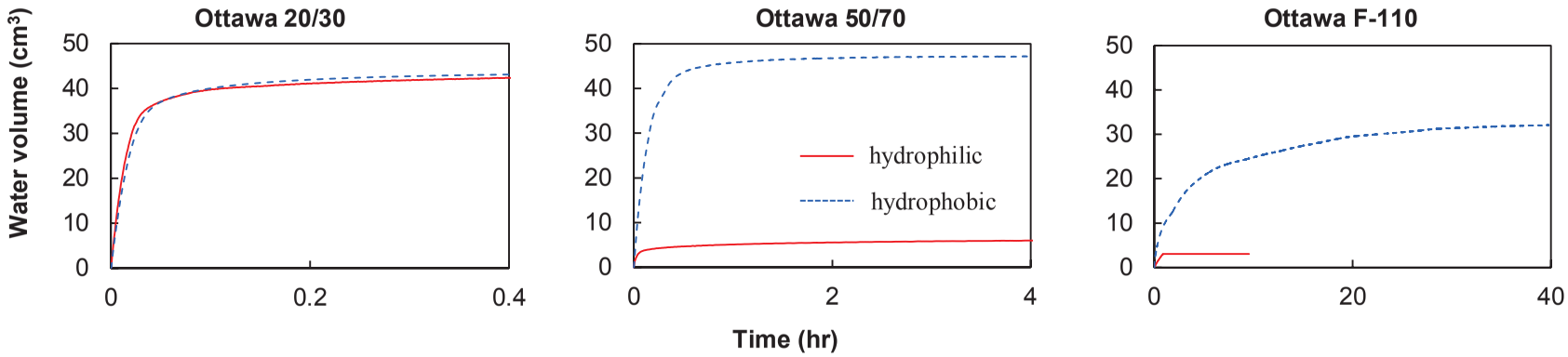

Figure 5.16 Gravity drainage of hydrophilic and hydrophobic sand columns with different particle sizes.

5.4 CONCLUSIONS

Surface wettability and associated conduction behaviors have a great number of engineering implications. In this chapter, thermal, electrical and hydraulic conduction behaviors were examined. The hypothesis has been verified that the particle-water interaction and pore fluid distribution in porous media play an important role on the heat, electron, and fluid conduction.

For thermal and electrical transfer in unsaturated porous media, hydrophilic soils have higher conduction capability due to the well-connected paths inside the material via capillary induced water films and liquid bridges at the particle contacts. Due to the water repellency, hydrophobic soils reject pore fluid inhabiting the particle contacts, therefore yield local dry particle sequestrations resulting poor connectivity.

Water infiltration, fully saturated flow, and air imbibition tests were conducted to determine the hydraulic conduction behaviors of sands with different surface wettability. Hydrophobic soils hinder water invasion at unsaturated conditions. When the soils have been fully saturated, hydrophobic sands allow faster water flow than the hydrophilic counterpart with the same void ratio. The hydrophobic surface reduces the fluid drag and flow friction between liquid-solid interfaces. In water drainage under gravity, the hydrophilic soils hold more water while the hydrophobic soils display high water drainage rates.

CHAPTER 6

CONCLUSIONS AND RECOMMENDATIONS

6.1 CONCLUSIONS

A unique synthesis process have been implemented to explore an innovative soil modification approach to engineer the natural soils with desired functionality, and develop a prototype of "smart soil" for potential applications such as intelligent hydraulic barrier, oil-water separation, and microbial controller. This research has also contributed to fundamental mechanistic understanding of the capillary effects in unsaturated soils with different surface wetting ability, including particle-fluid interaction, the small-strain stiffness, and thermal, electrical, hydraulic conduction behaviors.

The most important conclusions from this study are summarized as follows:

Surface modification: poly-NIPAAm has been proved to be an ideal material to alter the surface wettability of geological materials, such as sand particles. The ATRP technique has been tested to be an effective polymer grafting method with strong bonding and excellent quality of coatings.

Particle fluid interaction: even subtle modification (nano scale) on the surfaces can influence the bulk properties (macro scale) of the material substantially. The polymer-grafted sands and reference silica surfaces show large water contact angles and display strong water non-wetting characteristic at temperatures higher than the LSCT of

the grafted polymer. Hydrophilic particles, in unsaturated state, tend to have pore water arrested at particle contacts providing a capillary "cementing" and evolving well developed conduction paths with large water-solid contact area. Hydrophobic sands, at low degree of saturation, swerve to constrict the water in pore space bearing isolated local dry particles with poor connectivity. At higher degrees of saturation, the air bubbles compress on particle surfaces reducing the water-solid contact area.

Small-strain stiffness: capillary effect plays a profound role at low degree of saturation for hydrophilic soils with an evidential increase on shear modulus. Hydrophobic soils develop negative capillary force and pressure opposite to those of hydrophilic ones.

Conduction behaviors: well defined conduction paths make unsaturated hydrophilic grains conductive material for adequate heat and electric current conduction at low degree of saturation, while poor connectivity confines the thermal diffusion and electrical conduction even at high degree of saturation for hydrophobic particles. For water transportation, dry hydrophilic sands are easier to be infiltrated than hydrophobic sands. On the other hand, gravity drainage is delayed in fully saturated hydrophilic sands which hold pore-water due to capillarity, whereas hydrophobic sands tend to drain readily under gravity, as the grain size getting smaller. For fully saturated flow, hydrophobic sands were found to have higher hydraulic conductivity than hydrophilic ones. In light of fluid drag reduction of non-wetting surface, it is believed that fully saturated hydrophobic soils develop slip boundary flow which considerably reduces flow friction and render higher hydraulic conductivity capability than hydrophilic soils.

6.2 RECOMMENDATIONS AND FUTURE RESEARCH

I suggest the following areas of further study:

- Development of engineered soils by grafting various types of "intelligent" polymers responsive to UV, solvent exposure, pH, ionic strength to accomplish other desired functionalities.
- Further investigation on thermal and electrical conduction behavior for heterogeneous and anisotropic particulate materials in view of the effects of surface wettability.
- Advance study on conduction behaviors of different fluids and examine experimentally the immiscible fluid separation applications.

REFERENCES

Abbaszadegan, M., Lechevallier, M. and Gerba, C., 2003, Occurrence of Viruses in US Groundwaters. American Water Works Association. Journal, 95: 107-120.

Abbott, S., Ralston, J., Reynolds, G. and Hayes, R., 1999, Reversible Wettability of Photoresponsive Pyrimidine-Coated Surfaces. Langmuir, 15: 8923-8928.

Abu-hamdeh, N.H. and Reeder, R.C., 2000, Soil Thermal Conductivity : Effects of Density, Moisture, Salt Concentration, and Organic Matter. Soil Science Society of America, Madison, WI, ETATS-UNIS

Adamson, A.W. and Gast, A.P., 1997, Physical Chemistry of Surfaces. Wiley

Advincula, R.C., Brittain, W.J., Caster, K.C. and Rühe, J. eds., 2004, Polymer Brushes - Synthesis, Characterization, Applications. Wiley-VCH.

Ahn, S.J., Kaholek, M., Lee, W.K., LaMattina, B., H LaBean, T. and Zauscher, S., 2004, Surface-Initiated Polymerization on Nanopatterns Fabricated by Electron-Beam Lithography. Advanced Materials, 16: 2141-2145.

Allen, G.C., Sorbello, F., Altavilla, C., Castorina, A. and Ciliberto, E., 2005, Macro-, micro- and nano-investigations on 3-aminopropyltrimethoxysilane self-assembly-monolayers. Thin Solid Films, 483: 306-311.

Anonymous, 1991, New Short Contact Time Processes Upgrade Residual Oils and Heavy Crudes. Oil & Gas Journal, 89: 79.

Arya, S.K., Prusty, A.K., Singh, S.P., Solanki, P.R., Pandey, M.K., Datta, M. and Malhotra, B.D., 2007, Cholesterol biosensor based on N-(2-aminoethyl)-3-aminopropyl-trimethoxysilane self-assembled monolayer. Analytical Biochemistry, 363: 210-218.

Aswal, D.K., Lenfant, S., Guerin, D., Yakhmi, J.V. and Vuillaume, D., 2006, Self assembled monolayers on silicon for molecular electronics. Analytica Chimica Acta, 568: 84-108.

Ayano, E., Nambu, K., Sakamoto, C., Kanazawa, H., Kikuchi, A. and Okano, T., 2006, Aqueous chromatography system using pH- and temperature-responsive stationary phase with ion-exchange groups. Journal of Chromatography A, 1119: 58-65.

Barrat, J.-L. and Bocquet, L., 1999, Large Slip Effect at a Nonwetting Fluid-Solid Interface. Physical Review Letters, 82: 4671-4674.

Baygents, J.C., Glynn, J.R., Albinger, O., Biesemeyer, B.K., Ogden, K.L. and Arnold, R.G., 1998, Variation of Surface Charge Density in Monoclonal Bacterial Populations: Implications for Transport through Porous Media. Environmental Science & Technology, 32: 1596-1603.

Bi, S., Wei, X., Li, N. and Lei, Z., 2008, In-situ formation of Fe_3O_4 nanoparticles within the thermosensitive hairy hybrid particles. Materials Letters, 62: 2963-2966.

Bragg, J.R., Prince, R.C., Harner, E.J. and Atlas, R.M., 1994, Effectiveness of bioremediation for the Exxon Valdez oil spill. Nature, 368: 413-418.

Brandon, T. and Mitchell, J., 1989, Factors Influencing Thermal Resistivity of Sands. Journal of Geotechnical Engineering, 115: 1683-1698.

Braun, D., Cherdron, H., Rehahn, M., Ritter, H. and Voit, B., 2004, Polymer Synthesis: Theory and Practice: Fundamentals, Methods, Experiments. Springer

Brettmann, T. and Amis, T., 2011, Thermal Conductivity Evaluation of a Pile Group Using Geothermal Energy Piles. Geo-Frontiers 2011499-508.

Bryant, D.E., Stewart, D.I., Kee, T.P. and Barton, C.S., 2003, Development of a Functionalized Polymer-Coated Silica for the Removal of Uranium from Groundwater. Environmental Science & Technology, 37: 4011-4016.

Burch, G.J., Moore, I.D. and Burns, J., 1989, Soil hydrophobic effects on infiltration and catchment runoff. Hydrological Processes, 3: 211.

Callewaert, M., Rouxhet, P.G. and Boulangé-Petermann, L., 2005, Modifying stainless steel surfaces with responsive polymers: effect of PS-PAA and PNIPAAM on cell adhesion and oil removal. Journal of Adhesion Science and Technology, 19: 765-781.

Catalan, L.J.J., Buset, K.C. and Kling, L., 2004, Low temperature oxidation for the remediation of soil contaminated with motor oil. Journal of Environmental Engineering and Science, 3: 279.

Chen, Z., Lu, X., Chan, C.M. and Mi, Y., 2006, Manipulating the surface properties of polyacrylamide with nitrogen plasma. European Polymer Journal, 42: 2914-2920.

Cho, G.C. and Santamarina, J.C., 2001, Unsaturated Particulate Materials: Particle-Level Studies. Journal of Geotechnical and Geoenvironmental Engineering, 127: 84-96.

Cortes, D.D., Martin, A.I., Yun, T.S., Francisca, F.M., Santamarina, J.C. and Ruppel, C., 2009, Thermal conductivity of hydrate-bearing sediments. Journal of Geophysical Research, 114: B11103.

Couet, J. and Biesalski, M., 2006, Surface-Initiated ATRP of N-Isopropylacrylamide from Initiator-Modified Self-Assembled Peptide Nanotubes. Macromolecules, 39: 7258-7268.

Dai, L., 2004, Intelligent Macromolecules for Smart Devices: From Materials Synthesis to Device Applications (Engineering Materials and Processes) Springer

De Bisschop, F.R.E. and Rigole, W.J.L., 1982, A physical model for liquid capillary bridges between adsorptive solid spheres: The nodoid of plateau. Journal of Colloid and Interface Science, 88: 117-128.

Dean, B. and Bhushan, B., 2010, Shark-skin surfaces for fluid-drag reduction in turbulent flow: a review. Philosophical Transactions of the Royal Society A: Mathematical, Physical and Engineering Sciences, 368: 5737-5737.

DeBano, L.F., Neary, D.G. and Ffolliott, P.F., 1998, Fire Effects on Ecosystems John Wiley & Sons, John Wiley & Sons

Delaine, J., 1985, SEPARATING OIL FROM WATER OFFSHORE. Chemical Engineer (London): 31-34.

Derjaguin, B.V. and Churaev, N.V., 1986, Flow of nonfreezing water interlayers and frost heaving. Cold Regions Science and Technology, 12: 57-66.

DeVera, A.L. and Strieder, W., 1977, Upper and lower bounds on the thermal conductivity of a random, two-phase material. The Journal of Physical Chemistry, 81: 1783-1790.

Doerr, S.H., Shakesby, R.A., Dekker, L.W. and Ritsema, C.J., 2006, Occurrence, prediction and hydrological effects of water repellency amongst major soil and

land-use types in a humid temperate climate. European Journal of Soil Science, 57: 741-754.

Dorrer, C. and Rühe, J., 2008, Wetting of Silicon Nanograss: From Superhydrophilic to Superhydrophobic Surfaces. Advanced Materials, 20: 159-163.

Etkin, D.S., 2005a, Historical overview of oil spills from all sources (1960-1998). Global Engineering Documents, Miami Beach, FL, United states.

Etkin, D.S., 2005b, Comparative methodologies for estimating on-water response costs for marine oil spills. Global Engineering Documents, Miami Beach, FL, United states.

Etkin, D.S., 2005c, Estimating cleanup costs for oil spills. Global Engineering Documents, Miami Beach, FL, United states.

Franco, C.M.M., Clarke, P.J., Tate, M.E. and Oades, J.M., 2000, Hydrophobic properties and chemical characterisation of natural water repellent materials in Australian sands. Journal of Hydrology, 231-232: 47-58.

Frattolillo, A., Giovinco, G., Mascolo, M.C. and Vitale, A., 2005, Effects of hydrophobic treatment on thermophysical properties of lightweight mortars. Experimental Thermal and Fluid Science, 30: 27-35.

Fu, Q., Rao, G.V.R., Ward, T.L., Lu, Y. and Lopez, G.P., 2007, Thermoresponsive Transport through Ordered Mesoporous Silica/PNIPAAm Copolymer Membranes and Microspheres. Langmuir, 23: 170-174.

Gallagher, P.M. and Lin, Y., 2005, Column testing to determine colloidal silica transport mechanisms. American Society of Civil Engineers, Austin, TX, United states.

Gargiulo, G., Bradford, S., Simunek, J., Ustohal, P., Vereecken, H. and Klumpp, E., 2007, Bacteria transport and deposition under unsaturated conditions: The role of the matrix grain size and the bacteria surface protein. Journal of Contaminant Hydrology, 92: 255-273.

Ginn, T.R., Wood, B.D., Nelson, K.E., Scheibe, T.D., Murphy, E.M. and Clement, T.P., 2002, Processes in microbial transport in the natural subsurface. Advances in Water Resources, 25: 1017-1042.

Goebel, M.-O., Woche, S.K., Bachmann, J., Lamparter, A. and Fischer, W.R., 2007, Significance of Wettability-Induced Changes in Microscopic Water Distribution for Soil Organic Matter Decomposition. Soil Science Society of America Journal, 71: 1593-1599.

Gratchev, I., Sassa, K., Osipov, V., Fukuoka, H. and Wang, G., 2007, Undrained cyclic behavior of bentonite-sand mixtures and factors affecting it. Geotechnical and Geological Engineering, 25: 349-367.

Guilherme, M.R., Silva, R., Girotto, E.M., Rubira, A.F. and Muniz, E.C., 2003, Hydrogels based on PAAm network with PNIPAAm included: hydrophilic-hydrophobic transition measured by the partition of Orange II and Methylene Blue in water. Polymer, 44: 4213-4219.

Heikenfeld, J. and Dhindsa, M., 2008, Electrowetting on Superhydrophobic Surfaces: Present Status and Prospects. Journal of Adhesion Science and Technology, 22: 319-334.

Heiney, P.A., Gruneberg, K., Fang, J., Dulcey, C. and Shashidhar, R., 2000, Structure and Growth of Chromophore-Functionalized (3-Aminopropyl)triethoxysilane Self-Assembled on Silicon. Langmuir, 16: 2651-2657.

Howarter, J.A. and Youngblood, J.P., 2006, Optimization of Silica Silanization by 3-Aminopropyltriethoxysilane. Langmuir, 22: 11142-11147.

Howarter, J.A. and Youngblood, J.P., 2007, Surface Modification of Polymers with 3-Aminopropyltriethoxysilane as a General Pretreatment for Controlled Wettability. Macromolecules, 40: 1128-1132.

Hryciw, R.D. and Susila, E., Year, Temporary Solidification of Coarse Grained Soil by Magnetorheological Fluids. 9.

Hsiue, G.-H., Hsu, S.-h., Yang, C.-C., Lee, S.-H. and Yang, I.K., 2002, Preparation of controlled release ophthalmic drops, for glaucoma therapy using thermosensitive poly-N-isopropylacrylamide. Biomaterials, 23: 457-462.

Huang, J., Pintauer, T. and Matyjaszewski, K., 2004, Effect of variation of [PMDETA]/[Cu(I)Br] ratio on atom transfer radical polymerization of n-butyl acrylate. Journal of Polymer Science Part A: Polymer Chemistry, 42: 3285-3292.

Ichimura, K., Oh, S.-K. and Nakagawa, M., 2000, Light-Driven Motion of Liquids on a Photoresponsive Surface. Science, 288: 1624-1626.

Ista, L.K., Perez-Luna, V.H. and Lopez, G.P., 1999, Surface-Grafted, Environmentally Sensitive Polymers for Biofilm Release. Applied and Environmental Microbiology, 65: 1603-1609.

Iwata, H., Oodate, M., Uyama, Y., Amemiya, H. and Ikada, Y., 1991, Preparation of temperature-sensitive membranes by graft polymerization onto a porous membrane. Journal of Membrane Science, 55: 119-130.

Jacobs, A., Lafolie, F., Herry, J.M. and Debroux, M., 2007, Kinetic adhesion of bacterial cells to sand: Cell surface properties and adhesion rate. Colloids and Surfaces B: Biointerfaces, 59: 35-45.

Jesionowski, T., 2009, Alkoxysilane-Functionalized Silica Fillers - Preparation and Characterization. Composite Interfaces, 16: 115-129.

Jia Ou and Blair Perot and Jonathan, P.R., 2004, Laminar drag reduction in microchannels using ultrahydrophobic surfaces. Physics of Fluids, 16: 4635-4643.

Jordan, R., Advincula, R., Buchmeiser, M.R., Dyer, D.J., Fukuda, T., Goto, A., Matsuda, T., Ohno, K., Tsujii, Y. and Yamamoto, S. eds., 2006, Surface-Initiated Polymerization I (Advances in Polymer Science). Springer.

Kaeselev, B., Pieracci, J. and Belfort, G., 2001, Photoinduced grafting of ultrafiltration membranes: comparison of poly(ether sulfone) and poly(sulfone). Journal of Membrane Science, 194: 245-261.

Kaholek, M., Lee, W.K., Ahn, S.J., Ma, H., Caster, K.C., LaMattina, B. and Zauscher, S., 2004, Stimulus-Responsive Poly(N-isopropylacrylamide) Brushes and Nanopatterns Prepared by Surface-Initiated Polymerization. Chem. Mater., 16: 3688-3696.

Khan, M.M. and Islam, M.R., 2006, Downhole separation of petroleum fluids. Petroleum Science and Technology, 24: 789-805.

Kim, D.H., Kim, Y.J., Lee, J.-S. and Yun, T.S., 2011, Thermal and Electrical Response of Unsaturated Hydrophilic and Hydrophobic Granular Materials. ASTM, West Conshohocken, PA, ETATS-UNIS 9 p.

Kong, J. and Li, K., 1999, Oil removal from oil-in-water emulsions using PVDF membranes. Separation and Purification Technology, 16: 83-93.

Kong, X., Kawai, T., Abe, J. and Iyoda, T., 2001, Amphiphilic Polymer Brushes Grown from the Silicon Surface by Atom Transfer Radical Polymerization. Macromolecules, 34: 1837-1844.

Lahann, J., Balcells, M., Lu, H., Rodon, T., Jensen, K.F. and Langer, R., 2003a, Reactive Polymer Coatings: A First Step toward Surface Engineering of Microfluidic Devices. Analytical Chemistry, 75: 2117-2122.

Lahann, J., Mitragotri, S., Tran, T.-N., Kaido, H., Sundaram, J., Choi, I.S., Hoffer, S., Somorjai, G.A. and Langer, R., 2003b, A Reversibly Switching Surface. Science, 299: 371-374.

Lee, J. and Santamarina, J., 2005, Bender Elements: Performance and Signal Interpretation. Journal of Geotechnical and Geoenvironmental Engineering, 131: 1063-1070.

Lee, J., Guimaraes, M. and Santamarina, J., 2007, Micaceous Sands: Microscale Mechanisms and Macroscale Response. Journal of Geotechnical and Geoenvironmental Engineering, 133: 1136-1143.

Li, D., Sun, X. and Khaleel, M., 2012, Comparison of Different Upscaling Methods for Predicting Thermal Conductivity of Complex Heterogeneous Materials System: Application on Nuclear Waste Forms. Metallurgical and Materials Transactions A: 1-9.

Li, W., Zhang, A., Feldman, K., Walde, P. and Schlüter, A.D., 2008, Thermoresponsive Dendronized Polymers. Macromolecules, 41: 3659-3667.

Lian, G., Thornton, C. and Adams, M.J., 1993, A Theoretical Study of the Liquid Bridge Forces between Two Rigid Spherical Bodies. Journal of Colloid and Interface Science, 161: 138-147.

Liang, L., Feng, X., Peurrung, L. and Viswanathan, V., 1999, Temperature-sensitive membranes prepared by UV photopolymerization of N-isopropylacrylamide on a surface of porous hydrophilic polypropylene membranes. Journal of Membrane Science, 162: 235-246.

Liu, G. and Zhang, G., 2005, Collapse and Swelling of Thermally Sensitive Poly(N-isopropylacrylamide) Brushes Monitored with a Quartz Crystal Microbalance. J. Phys. Chem. B, 109: 743-747.

Lu, N. and Likos, W.J., 2004, Unsaturated Soil Mechanics. Wiley

Matyjaszewski, K., 2012a, Atom Transfer Radical Polymerization (ATRP): Current Status and Future Perspectives. Macromolecules, 45: 4015-4039.

Matyjaszewski, K., 2012b, Atom Transfer Radical Polymerization: From Mechanisms to Applications. Israel Journal of Chemistry, 52: 206-220.

McHale, G., Shirtcliffe, N.J., Newton, M.I. and Pyatt, F.B., 2007, Implications of ideas on super-hydrophobicity for water repellent soil. Hydrological Processes, 21: 2229-2238.

Megias-Alguacil, D. and Gauckler, L.J., 2009, Capillary forces between two solid spheres linked by a concave liquid bridge: Regions of existence and forces mapping. AIChE Journal, 55: 1103-1109.

Minko, S., Müller, M., Motornov, M., Nitschke, M., Grundke, K. and Stamm, M., 2003, Two-Level Structured Self-Adaptive Surfaces with Reversibly Tunable Properties. Journal of the American Chemical Society, 125: 3896-3900.

Motornov, M., Minko, S., Eichhorn, K.-J., Nitschke, M., Simon, F. and Stamm, M., 2003, Reversible Tuning of Wetting Behavior of Polymer Surface with Responsive Polymer Brushes. Langmuir, 19: 8077-8085.

Mukerji, T., Mavko, G. and Gomez, C., 2009, Cross-property rock physics relations for estimating low-frequency seismic impedance trends from electromagnetic resistivity data. The Leading Edge, 28: 94-97.

Nanda, A.K. and Matyjaszewski, K., 2003, Effect of [PMDETA]/[Cu(I)] Ratio, Monomer, Solvent, Counterion, Ligand, and Alkyl Bromide on the Activation Rate Constants in Atom Transfer Radical Polymerization. Macromolecules, 36: 1487-1493.

Nelson, J.D. and Miller, D.J., 1992, Expansive Soils: Problems and Practice in Foundation and Pavement Engineering. J. Wiley

Nguyen, B.-L., Bruining, J. and Slob, E.C., 1999, Effects of wettability on dielectric properties of porous media. Soc Pet Eng (SPE), Richardson, TX, United States, Houston, TX, USA.

Okamura, A., Itayagoshi, M., Hagiwara, T., Yamaguchi, M., Kanamori, T., Shinbo, T. and Wang, P.-C., 2005, Poly(N-isopropylacrylamide)-graft-polypropylene membranes containing adsorbed antibody for cell separation. Biomaterials, 26: 1287-1292.

Ou, J., Perot, B. and Rothstein, J.P., 2004, Laminar drag reduction in microchannels using ultrahydrophobic surfaces. Physics of Fluids, 16: 4635-4643.

Pamukcu, S. and Akbulut, S., 2006, Thermoelastic Enhancement of Damping of Sand Using Synthetic Ground Rubber. Journal of Geotechnical and Geoenvironmental Engineering, 132: 501-510.

Peng, T. and Cheng, Y.-L., 1998, Temperature-responsive permeability of porous PNIPAAm-g-PE membranes. Journal of Applied Polymer Science, 70: 2133-2142.

Pintauer, T. and Matyjaszewski, K., 2005, Structural aspects of copper catalyzed atom transfer radical polymerization. Coordination Chemistry Reviews, 249: 1155-1184.

Rebata-Landa, V., 2007, Microbial activity in sediments: Effects on soil behavior, Ph.D., Georgia Institute of Technology, United States -- Georgia, 173.

Rodriguez, E.L. and Newaz, G.M., 1988, The effect of sand surface treatment on sand-filled composites. Polymer Composites, 9: 93-102.

Rodriguez, M.A., Rubio, J., Rubio, F., Liso, M.J. and Oteo, J.L., 1997, Application of inverse gas chromatography to the study of the surface properties of slates. Clays and Clay Minerals, 45: 670-680.

Rosario, R., Gust, D., Garcia, A.A., Hayes, M., Taraci, J.L., Clement, T., Dailey, J.W. and Picraux, S.T., 2004, Lotus Effect Amplifies Light-Induced Contact Angle Switching. The Journal of Physical Chemistry B, 108: 12640-12642.

Rosenberg, E., Rosenberg, M. and Gutnick, D.L., 1983, Adherence of Bacteria to Hydrocarbons. DOE, Bartlesville Energy Technology Cent (CONF-8205140), Bartlesville, OK, USA, Afton, OK, USA.

Rushton, A., Ward, A.S. and Holdich, R.G., 2000, Solid-Liquid Filtration and Separation Technology. Wiley-VCH

Sanders, R.S., Chow, R.S. and Masliyah, J.H., 2003, Hydrophobic Interactions in Silane-Treated Silica Suspensions and Bitumen Emulsions. The Canadian Journal of Chemical Engineering, 81: 43-52.

Scott, D.F., 2000, Soil wettability in forested catchments in South Africa; as measured by different methods and as affected by vegetation cover and soil characteristics. Journal of Hydrology, 231: 87.

Sokolovic, R.M.S., Vulic, T.J. and Sokolovic, S.M., 2007, Effect of bed length on steady-state coalescence of oil-in-water emulsion. Separation and Purification Technology, 56: 79-84.

Stalcup, D., Yoshioka, G., Kaiman, B., Siegmann, L. and Masters, K., Year, Major oil spill incidents: Lessons for response planning. 2005 International Oil Spill Conference, IOSC 2005, Miami Beach, FL, United states, 4483-4485.

Sun, C., Aston, D.E. and Berg, J.C., 2002, Structural Evolution of Octyltriethoxysilane Films on Glass Surfaces during Annealing at Elevated Temperature. Journal of Colloid and Interface Science, 248: 96-102.

Sun, T., Wang, G., Feng, L., Liu, B., Ma, Y., Jiang, L. and Zhu, D., 2004a, Reversible Switching between Superhydrophilicity and Superhydrophobicity13. Angewandte Chemie International Edition, 43: 357-360.

Sun, T., Wang, G., Feng, L., Liu, B., Ma, Y., Jiang, L. and Zhu, D., 2004b, Reversible Switching between Superhydrophilicity and Superhydrophobicity. Angewandte Chemie International Edition, 43: 357-360.

Tafuri, A.N., Yezzi Jr., J.J., Watts, D.J. and Carlyle, J.M., 2005, Leak detection and leak location in underground pipeline. Global Engineering Documents, Miami Beach, FL, United states.

Torkzaban, S., Hassanizadeh, S.M., Schijven, J.F. and van den Berg, H.H.J.L., 2006, Role of air-water interfaces on retention of viruses under unsaturated conditions. Water Resources Research, 42: W12S14.

Truong, Q.H., Lee, J.-S., Dong, Y. and Yun, T.S., 2011, Capillary Induced Small-Strain Stiffness For Hydrophilic And Hydrophobic Granular Materials: Experimental And Numerical Studies. Japanese Geotechnical Society, Tokyo, JAPON 9 p.

Tu, H., Heitzman, C.E. and Braun, P.V., 2004, Patterned Poly(N-isopropylacrylamide) Brushes on Silica Surfaces by Microcontact Printing Followed by Surface-Initiated Polymerization. Langmuir, 20: 8313-8320.

Vandermeulen, J.H., Seizer, P.D. and Penrose, W.R., 2005, Persistence of non-alkane components of Bunker C oil in beach sediments of Chedabucto Bay, and lack of their metabolism by molluscs. Global Engineering Documents, Miami Beach, FL, United states.

Voronov, R.S., Papavassiliou, D.V. and Lee, L.L., 2007, Slip length and contact angle over hydrophobic surfaces. Chemical Physics Letters, 441: 273-276.

Wang, N., Zhao, Y. and Jiang, L., 2008, Low-Cost, Thermoresponsive Wettability of Surfaces: Poly(*n*-isopropylacrylamide)/Polystyrene Composite Films Prepared by Electrospinning. Macromolecular Rapid Communications, 29: 485-489.

Wang, W. and Vaughn, M.W., 2008, Morphology and Amine Accessibility of (3-Aminopropyl) Triethoxysilane Films on Glass Surfaces. Scanning, 30: 65-77.

Watanabe, K., Udagawa, Y. and Udagawa, H., 1999, Drag reduction of Newtonian fluid in a circular pipe with a highly water-repellent wall. Journal of Fluid Mechanics, 381: 225-238.

Wu, T., Zhang, Y., Wang, X. and Liu, S., 2008, Fabrication of Hybrid Silica Nanoparticles Densely Grafted with Thermoresponsive Poly(N-isopropylacrylamide) Brushes of Controlled Thickness via Surface-Initiated Atom Transfer Radical Polymerization. Chemistry of Materials, 20: 101-109.

Xia, F., Feng, L., Wang, S., Sun, T., Song, W., Jiang, W. and Jiang, L., 2006a, Dual-Responsive Surfaces That Switch between Superhydrophilicity and Superhydrophobicity. Advanced Materials, 18: 432-436.

Xia, F., Ge, H., Hou, Y., Sun, T., Chen, L., Zhang, G. and Jiang, L., 2007, Multiresponsive Surfaces Change Between Superhydrophilicity and Superhydrophobicity. Advanced Materials, 19: 2520-2524.

Xia, Y., Burke, N.A.D. and Stover, H.D.H., 2006b, End Group Effect on the Thermal Response of Narrow-Disperse Poly(N-isopropylacrylamide) Prepared by Atom Transfer Radical Polymerization. Macromolecules, 39: 2275-2283.

Xiu, Y., Zhu, L., Hess, D. and Wong, C.P., 2006, Superhydrophobic Silicone/PTFE Films for Biocompatible Application in Encapsulation of Implantable Microelectronics Devices. 2006 Electronic Components and Technology Conference.

Yoshioka, G. and Vitale, E., 2005, The threat of oil spills from storage tanks at end user facilities. Global Engineering Documents, Miami Beach, FL, United states.

Yun, T.S., 2005, Mechanical and Thermal Study of Hydrate Bearing Sediments, Ph.D., Georgia Institute of Technology, Atlanta

Yun, T.S. and Santamarina, J.C., 2008, Fundamental study of thermal conduction in dry soils. Granular Matter, 10: 197.

Yun, T.S. and Evans, T.M., 2010, Three-dimensional random network model for thermal conductivity in particulate materials. Computers and Geotechnics, 37: 991-998.

Zhang, K., Ma, J., Zhang, B., Zhao, S., Li, Y., Xu, Y., Yu, W. and Wang, J., 2007, Synthesis of thermoresponsive silica nanoparticle/PNIPAM hybrids by aqueous surface-initiated atom transfer radical polymerization. Materials Letters, 61: 949-952.

Zhang, L., 2007, Thermally-Responsive Core-Shell Particles, Lehigh University, Bethlehem

Zhang, X.-Z., Wu, D.-Q. and Chu, C.-C., 2004, Synthesis, characterization and controlled drug release of thermosensitive IPN-PNIPAAm hydrogels. Biomaterials, 25: 3793-3805.

Zornberg, J.G., Cabral, A.R. and Viratjandr, C., 2004, Behaviour of tire shred - sand mixtures. Canadian Geotechnical Journal, 41: 227 - 241.

VITA

Yi Dong was born on September 3, 1983 in Quzou, Zhejiang province in China. He received his Bachelor degree of Civil Engineering from Zhengzhou University, Zhengzhou, China in 2005. He obtained his Master degree of Structural Engineering from Tongji University, Shanghai, China in 2008. He started research towards this doctoral dissertation at Lehigh University in August 2008.